



FRANÇOIS-RABELAIS UNIVERSITY OF TOURS



Doctoral School Health, Science and Technology

Laboratory: Inserm U930 "*Imaging and Brain*", CNRS ERL 3106, Team 5

THESIS defended by:

Sébastien MÉNIGOT

on December 12th, 2011

to obtain the rank of: Doctor of the François-Rabelais University of Tours

Discipline / Speciality: Life and Health Sciences

Optimal Command Applied to Ultrasound Imaging System

THESIS SUPERVISED BY:

Jean-Marc GIRAULT Reader

François Rabelais University of Tours

Abdeldjalil OUAHABI Full Professor

François Rabelais University of Tours

REVIEWERS :

Olivier BASSET Full Professor

Claude-Bernard University, Lyon I

Claude DEPOLLIER Full Professor

University of Maine, Le Mans

JURY:

Olivier BASSET Full Professor

Claude-Bernard University, Lyon I

Claude DEPOLLIER Full Professor

University of Maine, Le Mans

Vincent GIBIAT Full Professor

Paul Sabatier University, Toulouse III

Denis KOUAMÉ* Full Professor

Paul Sabatier University, Toulouse III

Jean-Marc GIRAULT Reader

François Rabelais University of Tours

Abdeldjalil OUAHABI Full Professor

François Rabelais University of Tours

* *President of the Jury*

PROOFREADING

Sébastien MÉNIGOT

Optimal Command Applied to Ultrasound
Imaging System

translated from French by
Sébastien Ménigot & Lucile Chauveau

2016

Original title

“Commande optimale appliquée aux systèmes d’imagerie ultrasonore”

PROOFREADING

The translations of this thesis is distributed with the license Creative Commons Attribution-NonCommercial-ShareAlike 2.0 Generic (CC BY-NC-SA 2.0).



You are free:



to Share — to copy, distribute and transmit the work



to Remix — to adapt the work

Under the following conditions:



Attribution — You must attribute the work in the manner specified by the author or licensor (but not in any way that suggests that they endorse you or your use of the work).



Noncommercial — You may not use this work for commercial purposes.



Share Alike — If you alter, transform, or build upon this work, you may distribute the resulting work only under the same or similar license to this one.

With the understanding that:

Waiver — Any of the above conditions can be waived if you get permission from the copyright holder.

Public Domain — Where the work or any of its elements is in the public domain under applicable law, that status is in no way affected by the license.

Other Rights — In no way are any of the following rights affected by the license: Your fair dealing or fair use rights, or other applicable copyright exceptions and limitations; The author's moral rights; Rights other persons may have either in the work itself or in how the work is used, such as publicity or privacy rights.

Notice — For any reuse or distribution, you must make clear to others the license terms of this work. The best way to do this is with a link to this web page:

<http://creativecommons.org/licenses/by-nc-sa/2.0/>

This is a human-readable summary of the Legal Code (the full license):

<http://creativecommons.org/licenses/by-nc-sa/2.0/fr/legalcode>

PROOFREADING

“Forty-two!” yelled Loonquawl. “Is that all you’ve got to show for seven and a half million years’ work?”

“I checked it very thoroughly,” said the computer, “and that quite definitely is the answer. I think the problem, to be quite honest with you, is that you’ve never actually known what the question is.”

ADAMS, D., *The Hitchhiker’s Guide to the Galaxy.*

Pan Books, London, UK.

PROOFREADING

Acknowledgements

First of all I would like to thank Olivier BASSET and Claude DEPOLLIER for agreeing to be the reviewers of this thesis, as well as all the members of the jury who took the time to judge this work.

This thesis has been supported by the National Research Agency within the MONITHER project (ANR-07-TECSAN-015) and the SURFOETUS project (ANR-07-TECSAN-023). This work has been featured several times in Congress with the support of the laboratory, as well as the French Acoustics Society.

I also thank the Clinical Research Center for the Technological Innovation of Tours (CIC-IT 806 CHU Tours) for their provision of ultrasound contrast products.

The success of this thesis can not only be attributed to a research work. A thesis would not be successful without the human environment of the laboratory. The atmosphere that prevails can only contribute to a better dynamic. For that, I thank all the members of the laboratory. I express thank-you-notes: Audren for his cooperation in setting up experiments on the cMUT in due course; Dom for his support on this thesis, as well as his commitment to the work we did together on the cMUT; Fatima for the work we started together and which should continue; Guillaume for his guidance in optimization algorithms; Leïla for her advices on the numerical solution of the oscillation of microbubbles in the model of MARMOTTANT; Mélouka for our poster at the San Diego Congress; Samuel for the confidence that he has given me at the IUT of Blois; Tatoux and Christelle for their help with administrative tasks; Tony for his beamforming explanations; all the people with whom I shared an office on the fourth and seventh floor; all the people who have directly or indirectly worked with me.

Many of you have supported me, including giving me the honor of attending my PhD, especially my mother Agnès, Alain, Jacques, my father Roger, Joëlle, Stéphane

ACKNOWLEDGEMENTS

and all the people who would have liked to come.

I thank my co-supervisor, Abdeldjalil OUAHABI, for his review and valuable corrections.

I offer a special thanks to Anthony NOVELL for his help and advices in the handling of experimental devices. His remarks during proofreading papers were relevant.

I want to thank Nicolas SÉNÉGOND for his explanation both on his model and on cMUT. His proofreading of the section on cMUT helped me confirm that I understood how they work. For all these efforts, I promise him a quiet night if we have to set off again together.

This work would not be this same without the help of Iulian VOICU, since he is the one whom initiated this topic on his master thesis. He is the one to who I turn first when I have a question on signal processing, on Matlab programming or just for talking about L^AT_EX. But beyond these scientific discussions, he became a friend.

Note that it is obvious that this thesis would not exist at all without my supervisor Jean-Marc GIRAULT. At the end of my master, he trusted me and convinced me to do this thesis. Without him, I would not have done it and I would have missed something. From the beginning, he is listening to me. His advices widen my vision to help me find new solutions. I'm glad he was my supervisor. I hope that our collaboration still continue for a long time.

Finally, beyond the science and the lab, I wink at my Fluffy *cat* which was able to disturb my writing weekends to better resume. I want to thank a lot Lucile who has been sharing my life and has been supporting me everyday for almost seven years. She has always been willing to correct my English or French papers. Her support was essential. These words can not express my gratitude and love.

Résumé

Les systèmes d'imagerie médicale ultrasonore ont considérablement amélioré le diagnostic clinique par une meilleure qualité des images grâce à des systèmes plus sensibles et des post-traitements. La communauté scientifique de l'imagerie ultrasonore a consenti à un très grand effort de recherche sur les post-traitements et sur le codage de l'excitation sans s'intéresser, outre mesure, aux méthodes de commande optimale. Ce travail s'est donc légitimement tourné vers les méthodes optimales basées sur l'utilisation d'une rétroaction de la sortie sur l'entrée. Pour rendre applicable ces méthodes, ce problème complexe de commande optimale a été transformé en un problème d'optimisation paramétrique sous-optimal et plus simple. Nous avons appliqué ce principe au domaine de l'imagerie ultrasonore : l'échographie, l'imagerie harmonique native et l'imagerie harmonique de contraste avec ou sans codage de la commande.

La simplicité de l'approche nous a permis, par une modification de la fonction de coût, de l'adapter à l'imagerie harmonique. Cette adaptation montre que la méthode peut être appliquée à l'imagerie ultrasonore en générale.

Aujourd'hui, les enjeux de l'imagerie ultrasonore portent non seulement sur les traitements des excitations ou des images mais aussi sur les capteurs. Ce point nous a conduit naturellement à rechercher la commande optimale des transducteurs capacitifs (cMUT) afin de les adapter à une utilisation plus large en imagerie ultrasonore codée. Nos méthodes de compensation et de codage par commande optimale procurent des résultats très prometteurs qui vont au delà de nos espérances.

Le champ d'applications de nos méthodes de codage optimal est large et nous n'en voyons pas forcément encore toutes les limites. L'atout majeur de nos approches est leur simplicité d'utilisation et d'implémentation. En effet, elles ne nécessitent pas d'informations *a priori* difficilement accessibles sur les outils utilisés ou milieux explorés. Notre système s'adapte automatiquement aux variations qui peuvent être liées au vieillissement du capteur ou à la modification du milieu exploré.

Mots clés: Boucle fermée, commande optimale, optimisation, imagerie ultrasonore, système adaptatif.

PROOFREADING

Abstract

Medical ultrasound imaging systems have greatly improved the clinical diagnosis by improving the image quality thanks to more sensitive systems and post-processings. The scientific community has made a great effort of research on post-processing and on encoding the excitation. The methods of the optimal control have been neglected. Our work has focused on the optimal methods based on the feedback from output to input. We have transformed the complex problem of optimal control into an easier suboptimal parametric problem. We apply the principle of optimal control to the ultrasound imaging, the ultrasound harmonic imaging and to the contrast harmonic imaging with or without encoding.

The simplicity of the method has allowed us to adapt it to harmonic imaging by a change in the cost function. This adaptation shows that our method can usually be applied to the ultrasound imaging.

Nowadays, the stakes of the ultrasound imaging focus not only on the excitation processings or image processings but also on the sensors. This point naturally leads us to seek the optimal control of the capacitive transducers (cMUT) in order to adapt them to the encoded ultrasound imaging. Our compensation and encoding methods by optimal control provide very promising results that go beyond our expectations. The application scope of our methods of optimal control is large and we do not see all the limits yet. The main advantage of our approaches is the easiness of their use and of their implementation. Indeed, our approaches do not require any *a priori* knowledge on system and medium explored. Our system automatically adapts itself to the changes which may be related to sensor ageing or to the medium change.

Keywords: Adaptive system, closed-loop, optimal control, optimization, ultrasound imaging.

PROOFREADING

Contents

Résumé	11
Abstract	13
List of Tables	20
List of Figures	32
List of Notations	33
Introduction	37
I Principle of the Optimal Command in Imaging	41
1 Introductions to Optimized Ultrasound Imaging Systems	43
1.1 Feedback and Closed Loop	43
1.2 Acoustic Optimization	44
1.2.1 Time Reversal	44
1.2.2 Topological Energy in Time Domain	46
1.3 Optimal Command for imaging system	48
1.3.1 Problem of Optimal Command with Constraints	48

1.3.2	Toward a Parametric Problem	49
1.4	Conclusion	52
 II Optimal Command in Ultrasound Contrast Harmonic Imaging		53
2	Ultrasound Harmonic Imaging and Simulation Models	55
2.1	Imaging Device	56
2.1.1	Simulation model	57
2.1.2	Experimental Setup	62
2.2	Contrast Imaging Techniques	63
2.2.1	Harmonic Imaging by Nonlinear Autoregressive Filtering	64
2.2.2	Pulse Inversion Imaging	67
2.2.3	Imaging by Phase and Amplitude Modulation	69
2.2.4	Imaging by Frequency Modulation	70
3	Optimal Command by Signal Families	73
3.1	Methods	74
3.2	Optimal Command by Family of Truncated Half-Sine Waves	75
3.2.1	Harmonic Imaging by Nonlinear Autoregressive Filtering	78
3.2.2	Imaging by Pulse Inversion	87
3.2.3	Imaging by Phase and Amplitude Modulation	94
3.2.4	Application to Tissue Harmonic Imaging	95
3.2.5	Conclusion	98
3.3	Optimal Command by Family of Sine Waves Modulated in Frequency	100
3.3.1	Setting of a Linear Modulation Law	101
3.3.2	Setting of a Quadratic Modulation Law	101
3.3.3	Setting of a Cubic Modulation Law	102
3.3.4	Discussions	103
4	Optimal Command of Transmitted Waveform	105

CONTENTS

4.1	Method	105
4.2	Optimal Command of Waveform for a Linear Medium	106
4.3	Optimal Command of Waveform for a Nonlinear Medium	108
4.3.1	Optimal Command of Backscattering	108
4.3.2	Optimal Command of Waveform in Imaging by Pulse Inversion	109
4.3.3	Conclusion	110
III Optimal Command of the Transducer Response		113
5 Optimal Command of a Capacitive Micromachined Ultrasound Transducers		115
5.1	Material: Simulation of a cMUT	117
5.2	Methods	119
5.2.1	Optimal Recursive Command	120
5.2.2	Optimal Iterative Command	121
5.3	Optimal Command of Encoded Excitation for cMUTs	121
5.3.1	Optimal Command for second harmonic imaging	122
5.3.2	Optimal Command for pulse inversion imaging	125
5.3.3	Optimal Command for imaging by chirp reversal	125
5.4	Conclusion	127
Conclusion		129
References		137
Appendix		141
A Optimization algorithm		141
A.1	Algorithm based on the Gradient	141
A.2	NELDER-MEAD Algorithm	142

B Optimal Command in Pulse Inversion Imaging	145
B.1 Setting of the Frequencies of Truncated Half-Sine Waves	145
B.2 Setting of the Amplitude Ratio Between the Truncated Half-Sine Waves	147
B.3 Setting of the Frequencies and the Amplitude Ratio of the Truncated Half-Sine Waves	148
C Optimal Command in Imaging by Phase and Amplitude Modulation	151
C.1 Setting of the Excitation Frequency	151
C.2 Setting of the Frequencies of Truncated Half-Sine Waves	153
C.3 Setting of the Amplitude Ratio Between the Truncated Half-Sine Waves	155
C.4 Setting of the Frequencies and the Amplitude Ratio of the Truncated Half-Sine Waves	156
D Optimal Command of Encoded Excitation for cMUTs	159
D.1 Optimal Command for Second Harmonic Imaging	159
D.2 Optimal Command for Pulse Inversion Imaging	160
D.3 Optimal Command for Chirp Reversal Imaging	160
E List of publications	163
Index	167

List of Tables

2.1	Mechanical properties of the medium to be explored [Szabo, 2004].	58
3.1	Optimizations for the family of truncated sine waves (HI-NAR: harmonic imaging by nonlinear autoregressive filtering, PI: pulse inversion imaging, CPS: phase modulation and amplitude imaging).	78
3.2	Optimal <i>CTR</i> of simulations in harmonic imaging by nonlinear autoregressive filter according to different optimal settings for a pressure level A_0 of 400 kPa.	86
3.3	<i>CTR</i> optimization simulations in pulse inversion imaging in different optimal settings for a A_0 of 400 kPa pressure level. The <i>CTR</i> increases with the number of optimization parameters.	93
3.4	<i>CTR</i> optimization simulations in imaging by phase and amplitude modulation in different optimal settings for a A_0 of 400 kPa pressure level. The <i>CTR</i> increases with the number of optimization parameters.	95
3.5	Optimal parameters of the simulations according to the different optimizations for a pressure level A_0 of 400 kPa (HI-NAR: harmonic imaging by nonlinear autoregressive filtering, PI: pulse inversion imaging, CPS: imaging by phase and amplitude modulation).	99
3.6	Simulations of the global maxima of the backscattered energy by a non-encapsulated microbubble with a $2.5 \mu\text{m}$ -radius when the excitation is a chirp and associated parameters of the modulation law (CHI: harmonic imaging by chirp; CPI: imaging of chirp inversion).	100

- 3.7 Simulations of the global maxima of the backscattered energy by a non-encapsulated microbubble with a $2.5 \mu\text{m}$ -radius when the excitation is a chirp and associated parameters of the modulation law (CHI: harmonic imaging by chirp; CPI: imaging of chirp inversion). 101
- 3.8 Optimal simulation parameters according to the different optimizations for a pressure level A_0 of 400 kPa in imaging by chirp inversion. 103

PROOFREADING

List of Figures

1	Block diagram of an unoptimized ultrasound imaging system.	37
1.1	Block diagram of an ultrasound imaging system optimized by feedback.	43
1.2	Block diagram of the imaging time reversal.	45
1.3	Block diagram of the topological energy in time domain.	47
1.4	Block diagram of ultrasound imaging by matched filter.	50
1.5	Experiment with an initial sinusoidal signal and with a pressure level A_0 of 137 kPa.	51
2.1	Scheme of the experimental setup	56
2.2	Block diagram of the principle of the simulation model.	57
2.3	Representation of the grid of speed c of wave speed and of the grid of the density ρ that define the medium to be explored. The ultrasound probe is located at the depth 0 at the top of the representation.	59
2.4	Histogram of the size distribution of microbubbles.	60
2.5	Modelisation of the effective surface tension of a monolayer of phospholipid of a microbubble.	61
2.6	Block diagram of the experimental device.	62
2.7	Block diagram of ultrasound imaging.	63
2.8	Block diagram of the harmonic imaging by nonlinear autoregressive filtering.	65
2.9	Bandwidth transducer showing the overlap between the transmission bandwidth and the receiver bandwidth for harmonic imaging.	65
2.10	Block diagram of pulse inversion imaging.	67

2.11	Principle of pulse inversion imaging.	68
2.12	Block diagram of the imaging by phase and amplitude modulation.	69
3.1	Block diagram of closed-loop ultrasound imaging.	75
3.2	Optimal solution computed analytically [Reddy and Szeri, 2002] and sample suboptimal solution defined for our family of truncated half-sine waves.	76
3.3	Simulations of optimizations using the excitation frequency f_0 in harmonic imaging by nonlinear autoregressive filter for different pressure levels A_0 . (a) Empirical investigations of the <i>CTR</i> maxima as a function of the excitation frequency $f_{0,k}$. The automatic optimization path for the pressure level $A_0 = 400$ kPa is depicted in black. (b) Automatic search of the <i>CTR</i> using the excitation frequency $f_{0,k}$ by an algorithm using the gradient.	79
3.4	Synthetic images in harmonic imaging by nonlinear autoregressive filter for a pressure level of $A_0 = 400$ kPa where the excitation frequency f_0 is (a) the center frequency f_c of the transducer ($f_c = 3.5$ MHz), (b) the two-thirds of the center frequency f_c of the transducer ($2/3f_c = 2.33$ MHz), (c) the optimal frequency ($f_{0,opt} = 2.28$ MHz).	80
3.5	Experiment of automatic optimization using the frequency of excitation f_0 in harmonic imaging by nonlinear autoregressive filter by a gradient algorithm.	81
3.6	Simulation of the empirical search of the <i>CTR</i> maximum as a function of the frequencies f_1 and f_2 of the truncated half-sine waves in harmonic imaging by nonlinear autoregressive filter for a pressure level $A_0 = 400$ kPa. The automatic searches are reported in black for the gradient algorithm and in white for the NELDER-MEAD algorithm.	82
3.7	Simulations of the automatic optimizations using the frequencies f_1 and f_2 of the truncated half-sine waves in harmonic imaging by nonlinear autoregressive filter for different pressure levels A_0 by the algorithm based on the gradient (a) and the NELDER-MEAD (b). The frequencies f_1 are written in solid lines, while the frequencies f_2 are dotted.	83

LIST OF FIGURES

3.8 Synthetic image in harmonic imaging by nonlinear autoregressive filter for a pressure level of $A_0 = 400$ kPa and with the optimal values of $f_{1,opt}$ and $f_{2,opt}$ 83

3.9 Simulations of the optimizations using the amplitude ratio α ratio in harmonic imaging by nonlinear autoregressive filter for different pressure levels A_0 . (a) Empirical searches of the CTR maxima as a function of α . The automatic optimization path for the pressure level $A_0 = 400$ kPa is marked in black. (b) Automatic search of CTR using α by an algorithm using the gradient. 84

3.10 Synthetic image in harmonic imaging by nonlinear autoregressive filter for a pressure level of $A_0 = 400$ kPa and with the optimal values of $f_{1,opt}$ and $f_{2,opt}$, and after optimization of α 85

3.11 Simulations of automatic optimizations using the frequencies f_1 and f_2 , and the amplitude ration α in harmonic imaging by nonlinear autoregressive filter for different pressure levels A_0 . The frequencies f_1 are written in solid lines, while the frequencies f_2 are dotted. 85

3.12 Synthetic image in harmonic imaging by nonlinear autoregressive filter for a pressure level of $A_0 = 400$ kPa after optimization of f_1 , f_2 and α 86

3.13 Simulations of the optimizations using the excitation frequency f_0 in pulse inversion imaging for different pressure levels A_0 . (a) Empirical searches of the CTR maxima as a function of $f_{0,k}$. The automatic optimization path for the pressure level $A_0 = 400$ kPa is marked in black. (b) Automatic search of CTR using $f_{0,k}$ by an algorithm using the gradient. 88

3.14 Synthetic images in pulse inversion imaging for a pressure level of $A_0 = 400$ kPa, where the excitation frequency is (a) the central frequency f_c of transducer ($f_0 = 3.5$ MHz), (b) the two-thirds of the center frequency f_c of the transducer ($f_0 = 2.33$ MHz), (c) the optimal frequency ($f_{0,opt} = 1.77$ MHz). 89

3.15 Experiment of automatic optimization using the excitation frequency f_0 in pulse inversion imaging by a gradient algorithm. 90

3.16 Simulations of the *CTR* optimizations for a pressure level A_0 of 400 kPa in the presence of an evolution of the microbubble properties during the optimization. The first optimization is performed with ten microbubbles of radius R_0 ; the second with five microbubbles of radius $2R_0$. The third optimization starts with ten microbubbles of radius R_0 up to iteration 10 and then with five microbubbles of radius $2R_0$ 91

3.17 Simulations of optimizations using the excitation frequency f_0 in pulse inversion imaging for different pressure levels A_0 and with constant axial resolution. (a) Empirical search of the *CTR* maxima as a function of the excitation frequency $f_{0,k}$ for different transmission bandwidths. (b) Automatic search of the *CTR* using the excitation frequency $f_{0,k}$ for a transmission bandwidth of 100 %, or a constant axial resolution of from 0.43 mm. 92

3.18 Synthetic images in pulse inversion imaging for a pressure level of $A_0 = 400$ kPa and with a constant axial resolution of 0.43 mm, where the frequency of the excitation is (a) two thirds of the center frequency f_c of the transducer ($f_0 = 2.33$ MHz), (b) the optimal frequency ($f_{0,opt} = 1.38$ MHz). 93

3.19 Simulation of the optimizations using the excitation frequency f_0 in tissue harmonic imaging for different pressure levels A_0 using the excitation frequency f_k by an algorithm using the gradient. 96

3.20 Synthetic images in tissue harmonic imaging for a pressure level of $A_0 = 400$ kPa where the excitation frequency f_0 is (a) the center frequency f_c of the transducer ($f_c = 3.5$ MHz), (b) the two-thirds of the center frequency f_c of the transducer ($2/3f_c = 2.33$ MHz), (b) the optimal frequency ($f_{0,opt} = 2.79$ MHz). 96

3.21 Experiment of automatic optimization using the frequency of excitation f_0 in tissue harmonic imaging by a gradient algorithm. 97

3.22 Experimental images in tissue harmonic imaging where the excitation frequency f_0 is (a) the center frequency f_c of the transducer ($f_c = 4$ MHz), (b) the two-thirds of the center frequency f_c of the transducer ($2/3f_c = 2.67$ MHz), (b) the optimal frequency ($f_{0,opt} = 2.02$ MHz). 97

LIST OF FIGURES

3.23 (a) Experiment of automatic optimization using the transmit frequency f_0 by the NELDER-MEAD algorithm in tissue pulse inversion imaging by a gradient algorithm. The frequencies f_1 are written in solid lines, while the frequencies f_2 are dotted. Associated experimental images, where the frequency of excitation is (b) the two thirds of the center frequency f_c of the transducer ($f_0 = 2.67$ MHz) and (c) the optimal frequency ($f_{0,opt} = 2.02$ MHz). 98

3.24 Simulations of the optimization of linear modulation law in imaging by chirp inversion for a pressure level A_0 of 50 kPa. (a) Empirical search of the CTR maximum as a function of f_0 and β_1 . The automatic optimization path is written in black. (b) Automatically search for CTR using f_0 and β_1 with the NELDER-MEAD algorithm. 102

3.25 Simulations of the optimization of the quadratic modulation law in imaging by chirp inversion for a pressure level A_0 of 50 kPa. (a) Empirical search of the CTR maximum as a function of f_0 , β_1 and β_2 . The automatic optimization path is written in black. (b) Automatically search for CTR using f_0 , β_1 and β_2 by the NELDER-MEAD algorithm. 103

3.26 Simulation of the automatic optimization of the cubic modulation law in imaging by chirp inversion for a pressure level A_0 of 50 kPa using f_0 , β_1 , β_2 and β_3 by the NELDER-MEAD algorithm. 104

4.1 Block diagram of optimal command of transmitted waveform for a linear medium with sinus wave excitation. 106

4.2 Comparison between the excitation after optimization and the backscattered signal for a linear system (at the top the excitation signal and the backscattered signal, in the middle their linear components of a nonlinear autoregressive filter; their quadratic components of a nonlinear autoregressive filter). The ordinate axis corresponds to normalized pressure values. 107

4.3 Comparison between the excitation after optimization and the backscattered signal for a nonlinear system (at the top the excitation signal and the backscattered signal, in the middle their linear components of a nonlinear autoregressive filter; their quadratic components of a nonlinear autoregressive filter). The ordinate axis corresponds to normalized pressure values. 108

4.4 Block diagram of optimal waveform in imaging by pulse inversion. . . 109

4.5 Histogram of the *CTR* measurements when the excitation is a noise. . 111

4.6 Optimization of the *CTR* by the search for parameters \mathbf{w} that describe the the excitation waveform. 111

5.1 Structure of a cMUT at different scales. 115

5.2 Block diagram of the optimal command for cMUT in the context of harmonic imaging. 116

5.3 First-order equivalent scheme of a capacitive transducer. 117

5.4 cMUT command for different frequencies and voltages (20% in red, 40% in green and 60% in blue of the collapse voltage) on the first line. Displacement u_{mb} associated to the membrane in comparison with the cavity size on the second line. Membrane displacement spectra on the third line. 119

5.5 Block diagram of cMUT optimal command to reach target signal x at output. 120

5.6 Simulation of the recursive optimization of the cMUT output when the target signal to be reached is a sine wave signal of 1 MHz and amplitude representing a membrane displacement u_{mb} of $\pm 10\%$ of the size of the cavity. (a) cMUT Command at the top. Normalized cMUT output in relation to the cavity size, target signal and error at the bottom. (b) Spectrum of the cMUT command at the top. Spectrum of target signal and cMUT output before and after optimization at the bottom. 122

LIST OF FIGURES

5.7 Simulation of the iterative optimization of the cMUT output when the target signal to be reached is a sine wave signal of 1 MHz and amplitude representing a membrane displacement u_{mb} of $\pm 10\%$ of the size of the cavity. (a) Mean quadratic error between the target signal MSE and the membrane displacement u_{mb} during the iterations k with the input parameters of the system. (b) cMUT command at the top. Normalized cMUT output in relation to the cavity size, target signal and error at the bottom. (b) Spectrum of the cMUT command at the top. Spectrum of target signal and cMUT output before and after optimization at the bottom. 123

5.8 Simulation of the iterative optimization of the cMUT output when the target signal to be reached is a sine wave signal of 1 MHz and amplitude representing a membrane displacement u_{mb} of $\pm 15\%$ of the size of the cavity. (a) Mean quadratic error between the target signal MSE and the membrane displacement u_{mb} during the iterations k with the input parameters of the system. (b) cMUT command at the top. Normalized cMUT output in relation to the cavity size, target signal and error at the bottom. (c) Spectrum of the cMUT command at the top. Spectrum of target signal and cMUT output before and after optimization at the bottom. 124

5.9 Simulation of the iterative optimization of the cMUT output when the target signal to be reached is a sine wave signal of 1 MHz, in opposite phase to the target signal presented in Fig. 5.7b, and amplitude representing a membrane displacement u_{mb} of $\pm 10\%$ of the size of the cavity. (a) Mean quadratic error between the target signal MSE and the membrane displacement u_{mb} during the iterations k with the input parameters of the system. (b) cMUT command at the top. Normalized cMUT output in relation to the cavity size, target signal and error at the bottom. (c) Spectrum of the cMUT command at the top. Spectrum of target signal and cMUT output before and after optimization at the bottom. 125

5.10 Simulation of the iterative optimization of the cMUT output when the target signal to be reached is a sinusoidal frequency-modulated signal where $f_0 = 1$ MHz and $\beta_1 = 20$ GHz/s, and amplitude representing a membrane displacement u_{mb} of $\pm 10\%$ of the size of the cavity. (a) Mean quadratic error between the target signal MSE and the membrane displacement u_{mb} during the iterations k with the input parameters of the system. (b) cMUT command at the top. Normalized cMUT output in relation to the cavity size, target signal and error at the bottom. (c) Spectrum of the cMUT command at the top. Spectrum of target signal and cMUT output before and after optimization at the bottom. 126

5.11 Simulation of the iterative optimization of the cMUT output when the target signal to be reached is a sinusoidal frequency-modulated signal where $f_0 = 1$ MHz and $\beta_1 = -20$ GHz/s, and amplitude representing a membrane displacement u_{mb} of $\pm 10\%$ of the size of the cavity. (a) Mean quadratic error between the target signal MSE and the membrane displacement u_{mb} during the iterations k with the input parameters of the system. (b) cMUT command at the top. Normalized cMUT output in relation to the cavity size, target signal and error at the bottom. (c) Spectrum of the cMUT command at the top. Spectrum of target signal and cMUT output before and after optimization at the bottom. 127

B.1 Simulation of the empirical search of the CTR maximum as a function of the frequencies f_1 and f_2 of the truncated half-sine waves in pulse inversion imaging by for a pressure level $A_0 = 400$ kPa. The automatic searches are reported in black for the gradient algorithm and in white for the NELDER-MEAD algorithm. 146

B.2 Simulations of the automatic optimizations using the frequencies f_1 and f_2 of the truncated half-sine waves in pulse inversion imaging for different pressure levels A_0 by the algorithm based on the gradient (a) and the NELDER-MEAD (b). The frequencies f_1 are written in solid lines, while the frequencies f_2 are dotted. 146

LIST OF FIGURES

B.3 Synthetic image in pulse inversion imaging for a pressure level of $A_0 = 400$ kPa and with the optimal values of $f_{1,opt}$ and $f_{2,opt}$ 147

B.4 Simulations of the optimizations using the amplitude ratio α ratio in pulse inversion imaging for different pressure levels A_0 . (a) Empirical searches of the CTR maxima as a function of α . The automatic optimization path for the pressure level $A_0 = 400$ kPa is marked in black. (b) Automatic search of CTR using α by an algorithm using the gradient. 147

B.5 Synthetic image in pulse inversion imaging for a pressure level of $A_0 = 400$ kPa and with the optimal values of $f_{1,opt}$ and $f_{2,opt}$, and after optimization of α 148

B.6 Simulations of automatic optimizations using the frequencies f_1 and f_2 , and the amplitude ration α in pulse inversion imaging for different pressure levels A_0 . The frequencies f_1 are written in solid lines, while the frequencies f_2 are dotted. 149

B.7 Synthetic image in pulse inversion imaging for a pressure level of $A_0 = 400$ kPa after optimization of f_1 , f_2 and α 149

C.1 Simulations of optimizations using the excitation frequency f_0 in imaging by phase and amplitude modulation for different pressure levels A_0 . (a) Empirical investigations of the CTR maxima as a function of the excitation frequency $f_{0,k}$. The automatic optimization path for the pressure level $A_0 = 400$ kPa is depicted in black. (b) Automatic search of the CTR using the excitation frequency $f_{0,k}$ by an algorithm using the gradient. 152

C.2 Synthetic images in imaging by phase and amplitude modulation for a pressure level of $A_0 = 400$ kPa where the excitation frequency f_0 is (a) the center frequency f_c of the transducer ($f_c = 3.5$ MHz), (b) the two-thirds of the center frequency f_c of the transducer ($2/3f_c = 2.33$ MHz), (b) the optimal frequency ($f_{0,opt} = 2.28$ MHz). 152

C.3 Experiment of automatic optimization using the frequency of excitation f_0 in imaging by phase and amplitude modulation by a gradient algorithm. 153

C.4 Simulation of the empirical search of the *CTR* maximum as a function of the frequencies f_1 and f_2 of the truncated half-sine waves in imaging by phase and amplitude modulation for a pressure level $A_0 = 400$ kPa. The automatic searches are reported in black for the gradient algorithm and in white for the NELDER-MEAD algorithm. 154

C.5 Simulations of the automatic optimizations using the frequencies f_1 and f_2 of the truncated half-sine waves in imaging by phase and amplitude modulation for different pressure levels A_0 by the algorithm based on the gradient (a) and the NELDER-MEAD (b). The frequencies f_1 are written in solid lines, while the frequencies f_2 are dotted. 154

C.6 Synthetic image in imaging by phase and amplitude modulation for a pressure level of $A_0 = 400$ kPa and with the optimal values of $f_{1,opt}$ and $f_{2,opt}$ 155

C.7 Simulations of the optimizations using the amplitude ratio α ratio in imaging by phase and amplitude modulation for different pressure levels A_0 . (a) Empirical searches of the *CTR* maxima as a function of α . The automatic optimization path for the pressure level $A_0 = 400$ kPa is marked in black. (b) Automatic search of *CTR* using α by an algorithm using the gradient. 155

C.8 Synthetic image in imaging by phase and amplitude modulation for a pressure level of $A_0 = 400$ kPa and with the optimal values of $f_{1,opt}$ and $f_{2,opt}$, and after optimization of α 156

C.9 Simulations of automatic optimizations using the frequencies f_1 and f_2 , and the amplitude ration α in imaging by phase and amplitude modulation for different pressure levels A_0 . The frequencies f_1 are written in solid lines, while the frequencies f_2 are dotted. 157

C.10 Synthetic image in imaging by phase and amplitude modulation for a pressure level of $A_0 = 400$ kPa after optimization of f_1 , f_2 and α . . 157

LIST OF FIGURES

- D.1 Simulation of the iterative optimization of the cMUT output when the target signal to be reached is a sine wave signal of a frequency $f_{res}/2$ and amplitude representing a membrane displacement u_{mb} of $\pm 10\%$ of the size of the cavity. (a) Mean quadratic error between the target signal MSE and the membrane displacement u_{mb} during the iterations k with the input parameters of the system. (b) cMUT command at the top. Normalized cMUT output in relation to the cavity size, target signal and error at the bottom. (c) Spectrum of the cMUT command at the top. Spectrum of target signal and cMUT output before and after optimization at the bottom. 160
- D.2 Simulation of the iterative optimization of the cMUT output when the target signal to be reached is a sine wave signal of a frequency $f_{res}/2$ and amplitude representing a membrane displacement u_{mb} of $\pm 17.5\%$ of the size of the cavity. (a) Mean quadratic error between the target signal MSE and the membrane displacement u_{mb} during the iterations k with the input parameters of the system. (b) cMUT command at the top. Normalized cMUT output in relation to the cavity size, target signal and error at the bottom. (c) Spectrum of the cMUT command at the top. Spectrum of target signal and cMUT output before and after optimization at the bottom. 161
- D.3 Simulation of the iterative optimization of the cMUT output when the target signal to be reached is a sine wave signal of a frequency $f_{res}/2$, in opposite phase to the target signal presented in Fig. D.1b, and amplitude representing a membrane displacement u_{mb} of $\pm 10\%$ of the size of the cavity. (a) Mean quadratic error between the target signal MSE and the membrane displacement u_{mb} during the iterations k with the input parameters of the system. (b) cMUT command at the top. Normalized cMUT output in relation to the cavity size, target signal and error at the bottom. (c) Spectrum of the cMUT command at the top. Spectrum of target signal and cMUT output before and after optimization at the bottom. 161

D.4 Simulation of the iterative optimization of the cMUT output when the target signal to be reached is a sinusoidal frequency-modulated signal where $f_0 = f_{res}/2$ and $\beta_1 = 20$ GHz/s, and amplitude representing a membrane displacement u_{mb} of $\pm 10\%$ of the size of the cavity. (a) Mean quadratic error between the target signal MSE and the membrane displacement u_{mb} during the iterations k with the input parameters of the system. (b) cMUT command at the top. Normalized cMUT output in relation to the cavity size, target signal and error at the bottom. (c) Spectrum of the cMUT command at the top. Spectrum of target signal and cMUT output before and after optimization at the bottom. 162

D.5 Simulation of the iterative optimization of the cMUT output when the target signal to be reached is a sinusoidal frequency-modulated signal where $f_0 = f_{res}/2$ and $\beta_1 = -20$ GHz/s, and amplitude representing a membrane displacement u_{mb} of $\pm 10\%$ of the size of the cavity. (a) Mean quadratic error between the target signal MSE and the membrane displacement u_{mb} during the iterations k with the input parameters of the system. (b) cMUT command at the top. Normalized cMUT output in relation to the cavity size, target signal and error at the bottom. (c) Spectrum of the cMUT command at the top. Spectrum of target signal and cMUT output before and after optimization at the bottom. 162

List of Notations

α	Ratio of the amplitudes of half truncated sinusoids
β_1	Linear modulation coefficient
β_2	Quadratic modulation coefficient
β_3	Cubical modulation coefficient
ε_{mb}	Relative electric permittivity of the membrane of cMUT
ε_0	Electric vacuum permittivity
ζ	Damping coefficient
η_1	Dynamic viscosity coefficient of liver
η_2	Dynamic viscosity coefficient of blood
η_{lipid}	Dynamic viscosity coefficient of phospholipid monolayer of microbubble
κ	Polytropic exponent of sulfur hexafluoride
λ	LAGRANGE multiplier
λ_o	Forgetting factor
μ	Convergence coefficient of optimization algorithm
ρ	Density
ρ_1	Density of liver
ρ_2	Density of blood
σ	Surface tension of microbubble
σ_{blood}	Surface tension of blood
ϕ	Phase
χ	Elastic modulus of the phospholipid monolayer of microbubble
Ω	Reference medium
Ω_m	Medium studied

A	Amplitude of the wave
A_0	Amplitude of the reference wave
A_1	Amplitude of the first truncated half sine
A_2	Amplitude of the second truncated half sine
B/A	Coefficient of non-linearity of the propagation
c	Speed of sound
c_1	Speed of sound in liver
c_2	Speed of sound in blood
CTR	Contrast to tissue ratio
$CTHF$	Contrast between harmonic components of the tissue and the fundamental components
d_s	Shell thickness of the microbubble
e	Error
E	Energy
\mathbb{E}	Expected value
ET	Topological Energy
f_0	Central frequency of excitation
f_1	Frequency of the first truncated half sine
f_2	Frequency of the second truncated half sine
f_c	Central frequency of transducer
f_{res}	Resonance frequency
F_{elec}	Electrostatic force
F_{fluid}	Fluid force on the membrane of cMUT
g	Topological Gradient
h	Impulse response
h_{eq}	Equivalent height of the cMUT cavity
h_{GAP}	Height of the cMUT cavity
h_{mb}	Height of the cMUT membrane
k	Iteration
$k_{stiffness}$	Constant of stiffness
J	Cost-function

LIST OF NOTATIONS

K	Order of nonlinear autoregressive filter
l	Line number of ultrasound image
m_{mb}	Mass of membrane cMUT
M	Memory of nonlinear autoregressive filter
MSE	Mean Squared Error
N_c	Cycle number of excitation
N_{el}	Element number of ultrasound probe used for focusing
\mathcal{N}	Symbol of Gaussian Statistics
p	Acoustic pressure
p_{bubble}	Pressure on the microbubble surface
p_0	Hydrostatic pressure
$p_{driving}$	Driving pressure incident of microbubble
P_x	Power of signal x
R	Radius of microbubble
R_0	Radius of microbubble at the equilibrium
S	Surface of cMUT
t	Time
T_1	Period of the first truncated half sine
T_2	Period of the second truncated half sine
T_{tot}	Time length of excitation
u	Displacement of particle by a wave
u_{mb}	Displacement of cMUT membrane
V	Voltage
y	System output
\hat{y}	Model of signal of output system
\mathbf{w}	Set of optimization parameters
w	Optimization parameter among parameters \mathbf{w}
z	Signal after post-processing and imaging method
z_L	Signal of linear component
z_Q	Signal of quadratic component

PROOFREADING

Introduction

SINCE the presentation of the first ultrasound scanner by J. J. WILD and J. REID in 1951 [Wild and Neal, 1951], the ultrasound imaging systems have steadily increased to provide physicians with better quality images [Wild and Neal, 1951]. Ultrasonography has become one of the major imaging modalities for its help in the early diagnoses and in the monitoring of diseases.

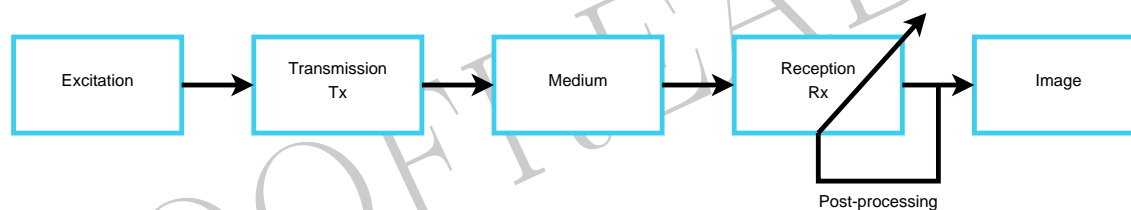


Figure 1 – Block diagram of an unoptimized ultrasound imaging system.

Each sub-process system has undergone major improvements whether at the level of sensors, electronics, signal processing or beamforming. The systems are thus more sensitive. But the general principle of ultrasound imaging system [Szabo, 2004] remains the same (Fig. 1):

1. a signal with a given form excites the ultrasound probe;
2. the ultrasound probe composed of many transducer elements converts the electrical signal into an ultrasound wave. Each signal associated with an element of the ultrasound probe is more or less delayed, depending on the chosen beamforming [Lingvall, 2004], so that the wave focuses on a spot in the medium to be imaged;
3. the ultrasound wave propagates into tissues;

4. the echoes are collected by the probe by applying the rules of beamforming. A line of the image is reconstructed by the signal envelope. Its amplitude gives information about the nature of the spot probed while the time given information about the depth of the point probed;
5. the first four operations are repeated with a focus on a close point. The image is performed line by line.

The main issues of the ultrasound imaging in which the research needs have shown an interest concern three interrelated topics: the contrast, the signal to noise ratio and the resolution. The majority of image enhancements have focused either on beamforming [Misaridis, 2001, Synnevag et al., 2007] or on the post-processing of the received signals [Szabo, 2004, Idier, 2008]. In all the cases, the received signal depends on the transducers in transmission and in reception of the transmitted acoustic wave.

From our point of view, open loop imaging systems can provide the optimum operating conditions only if the command of the system is properly pre-set. However, such knowledge is difficult to accurately identify, knowing that from one patient to another, the physical characteristics of tissues differ slightly. Moreover, the non-linearities of the system and of the medium explored make it difficult to explore analytical problem solving.

The difficulty is thus to find a method which optimizes the desired criterion by an optimal setting of the system command and without *a priori* knowledge of this system. To automatically find the optimal settings for the system, we propose to use the information of the output signal, *i.e.* the signals constituting the final ultrasound image. The open loop imaging system is transformed into a closed loop imaging system, but whose properties are preserved (bandwidth, physical properties, *etc.*).

To validate this concept of optimal command in ultrasound imaging, the manuscript is divided into three parts. The first part is devoted to an introduction of the general issue of optimal command in ultrasound imaging. In the second part, from chapters 2 to 4, our concept is applied to the native and contrast harmonic ultrasound imaging. The simulation models will be presented first, then the experiments and finally the approaches that seemed suitable for real-time imaging. We will present in

chapter 3 parametric suboptimal methods using known families of signals. Instead, in chapter 4, we will present non-parametric sub-optimal methods maximizing a waveform, although we will modify the parameters of a filter. Finally, in the last part of this thesis, we will present our vision of the optimal command in coded imaging using cMUTs. Finally, we will conclude and we will suggest several perspectives to this research work.

PROOFREADING

PROOFREADING

— PART I —

**PRINCIPLE OF THE OPTIMAL
COMMAND IN ULTRASOUND IMAGING**

PROOFREADING

Chapter 1

Introductions to Optimized Ultrasound Imaging Systems

SINCE the advent of the first ultrasound imaging systems, their improvement has mainly focused on post-processings of the received signal. However, these methods can not be fully effective in the presence of poor quality signal. The improvement of ultrasound images therefore require a suitable choice of command systems.

In this chapter, we will briefly explain the operation of a ultrasound imaging system optimized by a closed-loop. Then we will draw up a state of the art of existing optimal commands. Finally, we will introduce the concept of parametric optimization.

1.1 Feedback and Closed Loop

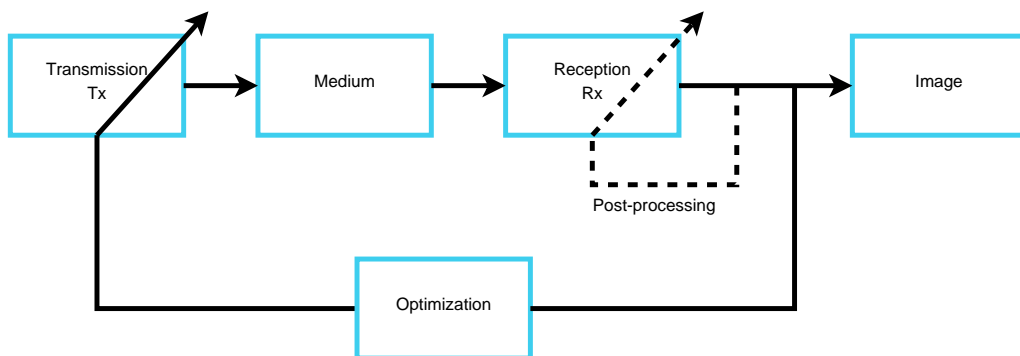


Figure 1.1 – Block diagram of an ultrasound imaging system optimized by feedback.

The optimization by closed loop consists in seeking the best tunings for a system which maximizes a cost function J . In our case, the parameters of the excitation (or command) are sought to maximize a criterion at the output of the system studied. Such a system is optimized by using a feedback from the output to the input (Fig. 1.1).

1.2 Acoustic Optimization

Since the 1990s, a few closed-loop methods have been proposed to optimize the signal-to-noise ratio (SNR) and the resolution. They are based on invariance properties such as the time reversal method [Fink, 1992].

1.2.1 Time Reversal

Time reversal is a method of adaptive beamforming through an aberrator medium using the physical properties of the medium. The goal is twofold. On the one hand, the resolution can be increased by reducing the size of the focusing spot. On the other hand, the signal-to-noise ratio can be maximized at the focusing spot while the energy around the focal spot is minimized. The echo from the scatterers at the focusing spot is more important than the echoes from other scatterers.

If the system performs linearly, it is possible to use the formalism of convolution such as:

$$y(t) = h(t) * x(t), \quad (1.1)$$

where $*$ is the convolution operator, t the time, $h(t)$ the impulse response of the system and $x(t)$ the system input. Maximizing the output $y(t)$ of the system is equivalent to performing an autocorrelation by settling the command, or if it is a post-processing, to adjusting the filter impulse response by settling $x(t) = h(-t)$.

To achieve this correlation, the time reversal method (Fig. 1.2) suggests to send a wave and to receive its echo (switch in position 1) in a first step. In a second step, the echo is reversed temporarily and sent to the medium (switch in position 2). The wave exactly follows the reverse path and focuses at the spot of echo emission. The

1.2. ACOUSTIC OPTIMIZATION

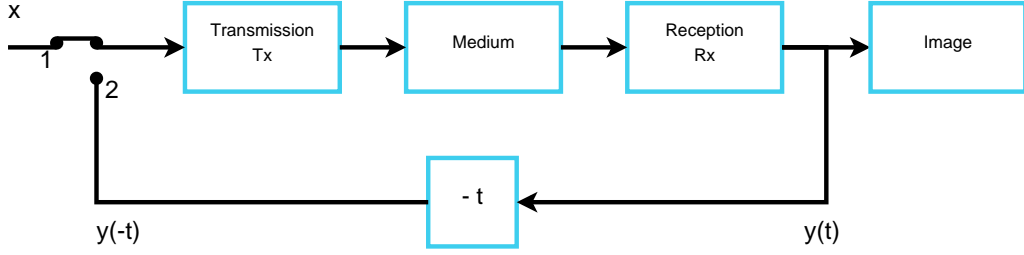


Figure 1.2 – Block diagram of the imaging time reversal.

signal y_{opt} at the output system after optimization becomes:

$$y_{opt}(t) = h(t) * y(-t) = h(t) * h(-t) * x(-t). \quad (1.2)$$

This principle has been generalized in the case of the use of a multi-element ultrasound probe [Prada and Fink, 1994] :

$$y_j(t) = \sum_{i=1}^{N_{el}} h_{ji}(t) * x_i(t), \quad (1.3)$$

where y_j is the backscattering for the element j of the ultrasound probe with N_{el} elements used for the wave focusing.

However to find the optimal command when the system is non-linear, the non-linearity of the system should be taken into account. If we want to draw a parallel between our approaches and time reversal, we should propose a formalism which takes into account the non-linearities for example by using the VOLTERRA series [Lacoume et al., 1997] :

$$y_j(t) = \sum_{i=1}^{N_{el}} \left(\sum_{k_1} h_{j1}(k_1) \cdot x(t - k_1) + \sum_{k_1, k_2} h_{j2}(k_1, k_2) \cdot x(t - k_1) \cdot x(t - k_2) + \dots + \sum_{k_1, \dots, k_K} h_{jK}(k_1, \dots, k_K) \cdot x(t - k_1) \dots x(t - k_K) \right), \quad (1.4)$$

where K is the order of the decomposition. Note that the first term of the decomposition corresponds to the convolution. When the decomposition is at the first order,

the equation 1.4 describes the time reversal defined by the equation 1.2.

Finding the optimal command of a nonlinear system is probably possible. In the case of a line of ultrasound image, the optimization problem of the output $y(t)$ can be written with the following equation:

$$\arg \max_{x(t)} (y(t)) = \arg \max_{x(t)} \left(h_1(t) * x(t) + h_2(t_1, t_2) * x(t) + \dots \right) \quad (1.5)$$

where $*$ is the symbol of N -dimensional convolution.

A first sub-optimal approach could be to maximize each one of the terms of the decomposition such as:

$$\max_{x(t)} (y(t)) \Leftrightarrow \max_{x(t)} \left(h_1(t) * x(t) \right) + \max_{x(t)} \left(h_2(t_1, t_2) * x(t) \right) + \dots \quad (1.6)$$

This optimization amounts therefore to finding the command $x(t)$ which would satisfy the maximization of each term. But this problem is not easy, since the problem involves a cost function with many simultaneous cost-functions, and therefore “single objective” optimization should become a “multi-objective” optimization.

In this work, the maximization problem is rather solved by using a decomposition with a nonlinear autoregressive model. To complete the list of the existing techniques in optimal command, we have to mention the technique of the maximization of the topological energy.

1.2.2 Topological Energy in Time Domain

The topological energy in time domain is an imaging method from the topological energy optimization with the constraint of the wave equation. From our point of view, this problem is conceptually closer to our approach than the time reversal imaging, for which the cost-function to be maximized with a constraint (the differential equations of propagation and of ultrasound contrast agent oscillations) is made mathematically explicit.

Here, the inverse problem aims at finding the topological properties of the medium observed. Created for the non-destructive testing [Dominguez et al., 2005], it is also applied to biological tissues [Sahuguet et al., 2010]. However, in this case, the process requires a quantification of the acoustic impedance distribution.

1.2. ACOUSTIC OPTIMIZATION

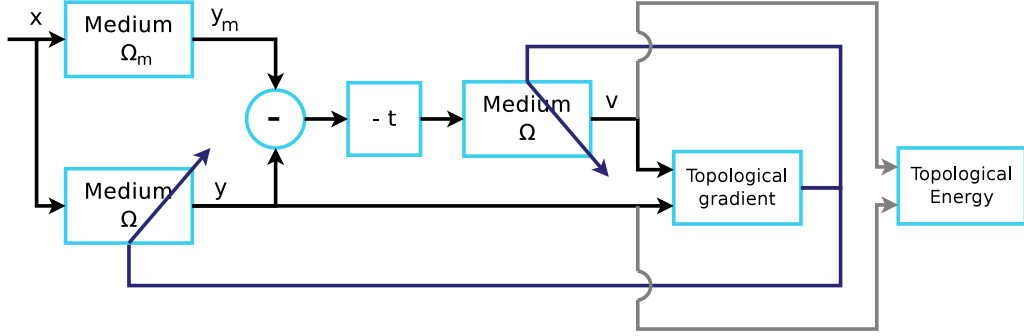


Figure 1.3 – Block diagram of the topological energy in time domain.

This method, described in Fig. 1.3, evaluates the correlation between the responses of a virtual medium Ω and of an unknown medium being explored Ω_m . The topological optimization thus consists in minimizing the difference between the ultrasound response y_m of Ω_m and the ultrasound response y of Ω such as:

$$J(\Omega) = \frac{1}{2} \int_0^{T_{obs}} \left(\int_{\Gamma_m} |y - y_m|^2 d\vec{r} \right) dt, \quad (1.7)$$

where T_{obs} is the observation duration. In practice, to initialize the optimization, the physical properties of the medium Ω are chosen homogeneous and as close as possible to the medium Ω_m . Starting from the reference medium Ω in which some infinitesimal “holes”^a are virtually and gradually inserted, the iterative optimization can deduce the medium topology.

To calculate the topological energy, it is necessary to solve two problems: the forward problem and the adjoint problem.

The forward problem consists in simulating the ultrasound field y generated by the propagation of the ultrasound wave in the medium Ω . The sensitivity of the variation $d\Omega$ of the medium Ω is determined from the asymptotic expansion of first order:

$$J(\Omega + d\Omega) = J(\Omega) + f(d\Omega)g(\vec{r}) + o(f(d\Omega)), \quad (1.8)$$

where $\forall d\Omega$, the boundary conditions are $f(d\Omega) > 0$, $\lim_{d\Omega \rightarrow 0} f(d\Omega) = 0$ and the function $g(\vec{r})$ is the topological gradient.

The adjoint problem is the second digital problem of the ultrasound propagation

^aArea whose properties have a high contrast in comparison with those of the surrounding medium.

of the time reversed difference v between the response y of the medium Ω and the response y_m of the medium Ω_m .

The topological gradient can be written from y and v such as:

$$g(\vec{r}) = \int_0^{T_{obs}} y(\vec{r}, t) \cdot v(\vec{r}, t) dt, \quad (1.9)$$

where $\vec{r} \in \Omega$. The positions in which the topological gradient is negative corresponds to the positions where infinitesimal holes have to be inserted. The topology thus tends toward the medium to be explored.

Finally, to see the result, it is possible to calculate the topological energy ET such as:

$$ET(\vec{r}) = \int_0^{T_{obs}} \|y(\vec{r}, t)\|^2 \cdot \|v(\vec{r}, t)\|^2 dt. \quad (1.10)$$

1.3 Optimal Command for imaging system

The optimal command [Åström and Wittenmark, 1994] has been created in 1960s in the aeronautics field. The aim was to determine the optimal parameters for the autopiloting.

1.3.1 Problem of Optimal Command with Constraints

The optimal command theory is derived from the variational calculus [Kirk, 2004]. By using LAGRANGE multipliers, the optimal command problem with constraint can be rewritten without constraint. The cost-function of the optimal command with constraint have to be minimized and it can be written:

$$J(x(t)) = \int_0^{T_{obs}} x^2(t) - \int_0^{T_{obs}} \lambda(t)G(t)dt, \quad (1.11)$$

where $\lambda(t)$ is the LAGRANGE multiplier and G the differential equation which describes the dynamic system. In the case of imaging systems, the function G has to take into account many nonlinear phenomena, such as the nonlinear propagation, the presence of ultrasound contrast agents or the sensor nonlinearities. If we want to take into account the largest number possible of phenomena, the problem solving

has no analytical solution. It is thus easier to understand a parametric optimization problem rather than a shape optimization problem [Girault, 2010].

1.3.2 Toward a Parametric Problem

We propose to apply an optimal command which optimizes the output by setting the system command on the principle of a closed loop system. However, as the existing algorithms which determine the command are sample to sample, it is not always possible to apply this solving in ultrasound imaging. Indeed, in the case of ultrasound imaging in which we want to optimize an image quality criterion, the latter has to be calculated before the new parameter values of the command. In these conditions, we try to apply “signal to signal” methods rather than sample to sample methods. **This last item constitutes one of the most important foundations of our concept, by adjusting well known techniques of adaptive filter to the ultrasound imaging field.**

To validate this concept, we tested the feasibility through a first experiment [Ménigot et al., 2010] where the aim was to optimize the contrast between the energy E_{agents} from the ultrasound contrast agents and the energy E_{tissue} from the surrounding medium. To simplify the experiment, we first focused on the energy backscattered by the ultrasound contrast agents such as:

$$\max_{\mathbf{w}}(E_{agents}) \quad (1.12)$$

where \mathbf{w} is the parameter filter.

The principle is described by the scheme 1.4 and it consists in:

1. sending a sinusoidal wave train $x(t)$ through the medium with PZT single element transducer (Sofranel, Sartrouville, France) centred at 2.25 MHz and with a bandwidth of 74%;
2. measuring the signal backscattered by ultrasound contrast agents $y(t)$ with a PZT single element transducer centred at 3.5 MHz and with a bandwidth of 63% (Sofranel, Sartrouville, France) ;

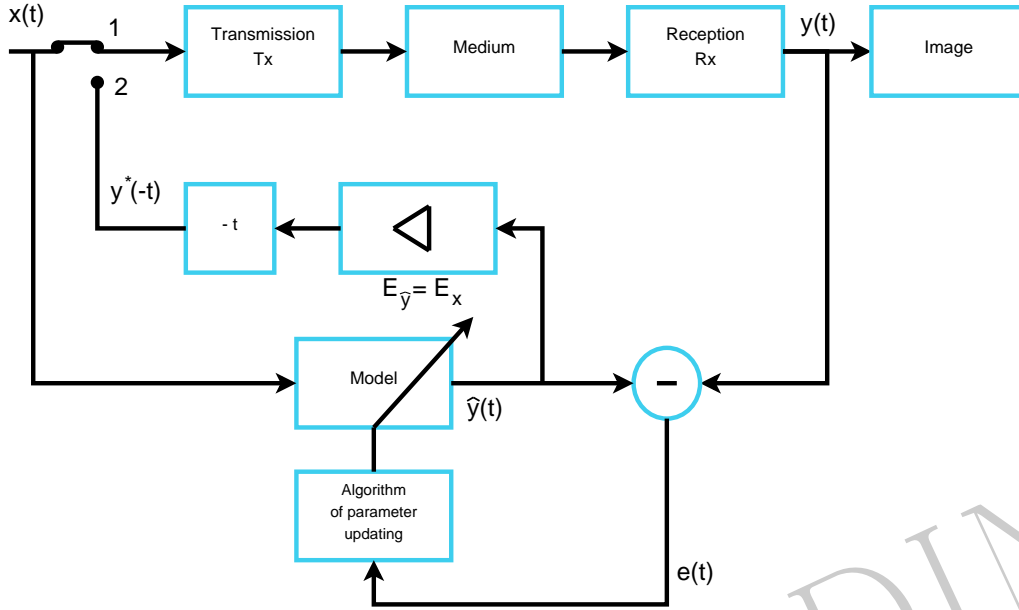


Figure 1.4 – Block diagram of ultrasound imaging by matched filter.

3. identifying the signal $y(t)$ by $\hat{y}(t)$ with an autoregressive filter of order four [Michaut, 1992]:

$$\hat{y}(t) = \sum_{i=1}^4 w_i y(t - i). \quad (1.13)$$

The parameters w of the filter are determined by the recursive least square method (RLS);

4. normalizing the amplitude of the signal $\hat{y}(t)$ so that its energy $E_{\hat{y}}$ is identical to the energy E_x of the transmitted signal $x(t)$. This signal is called $y^*(t)$;
5. the new excitation is $y^*(t)$ and return to step 2.

Fig. 1.5 represents the gain between the backscattered energy when the system excitation is $y^*(t)$ and the backscattered energy when the system excitation is $x(t)$. Note that the matched filter does not take into account the step 3 with $\hat{y} = y$.

The main idea of our approach is to identify the signal $y(t) = h(t) * x(t)$ of the imaging system (transducer and medium) during a learning step (switch in position 1). Then, when the learning step is completed (switch in position 2), the signal $\hat{y}(t)$ is time-reversed and sent instead of $x(t)$.

This technique provides the foundations of our optimal command principle, since the main advantage is that no *a priori* information is required to find an

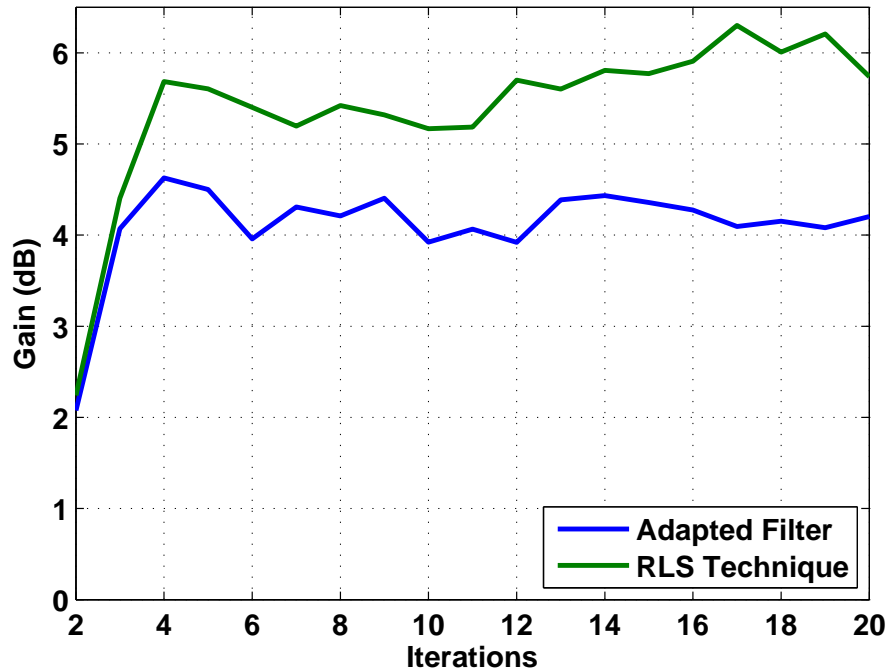


Figure 1.5 – Experiment with an initial sinusoidal signal and with a pressure level A_0 of 137 kPa.

optimal command of the system. However, in this case, the assumption of the contrast optimization by only maximizing the energy backscattered by ultrasound contrast agents is a too restrictive assumption, since it does not take into account the minimization of energy backscattered by the surrounding tissue. Conversely, the suppression of tissue harmonic contribution [Couture et al., 2008] increases the contrast, but certainly without reaching the contrast global maximum. Moreover, knowing that the matched filter does not let the free choice of the cost-function, we have to imagine other ways to optimize our cost-function, which we suggest in the next part.

1.4 Conclusion

Up to now in the ultrasound imaging field, researches in optimal command for ultrasound imaging are limited or even nonexistent. Only some studies are references [Fink, 1992, Reddy and Szeri, 2002, Dominguez et al., 2005, Mleczko et al., 2007]. Time reversal, although widely used, is not really one of the optimal command techniques, since no explicit cost-function is optimized. Our research work on optimal command clearly and show the different kinds of cost-function to optimize. They are distinct from existing works, since they are mainly based on optimal adaptive filtering. For now, we think sensing just a part of the high potential of such methods. Besides, the preliminary results shown previously partly confirm this potential. We therefore propose to continue in this way taking as a line of sight the applicability of this method for ultrasound imaging, especially the medical field.


— PART II —

**OPTIMAL COMMAND IN ULTRASOUND
CONTRAST HARMONIC IMAGING**

PROOFREADING

Chapter 2

Ultrasound Harmonic Imaging and Simulation Models

 OVER the past twenty years, improvements in the sensitivity of medical ultrasound imaging systems have provided more accurate medical diagnoses through intravenous injection of ultrasound contrast agents containing microbubbles. The perfusion imaging thus obtained, in the myocardium or in tumors for example, has provided physiological and pathological information [Frinking et al., 2000]. Initially, only the linear interactions between the microbubbles and the ultrasound waves were operated in B-mode to increase the sensitivity between the tissue and the microbubbles. However, the use of ultrasound contrast imaging was revolutionized in clinical practice when the nonlinear interaction between microbubbles and ultrasound wave was taken into account. The nonlinearity of the contrast agent response has become one of the major focus of research to obtain the best contrast. Indeed, soft tissue are known to be essentially linear scatterers [Borsboom et al., 2009], while the microbubbles have a high nonlinear behaviour during the ultrasound interaction. Unfortunately, obtaining an ideal method has been limited by two factors. First, good separation of the harmonic components requires a limited pulse bandwidth [Averkiou, 2000], which reduces the axial resolution, like in second harmonic imaging [Burns, 2002]. Secondly, the effects of the ultrasound wave propagation limit the *CTR* because of the presence of nonlinear components generated in tissue [Frinking et al., 2000].

Several imaging methods have been proposed to improve contrast and/or resolution. Some of the best-known techniques are methods with discrete or continuous encoding of the amplitude, of the phase or of the frequency of the transmitted

ultrasound wave. While the non-encoded techniques use post-processing such as filtering, the others use a combination of excitations to extract the nonlinearities.

In this chapter, we will explain the ultrasound contrast harmonic imaging device that we have, as well as implemented imaging methods. An ultrasound scanner driven by a personal computer makes an image of a phantom mimicking tissue in which ultrasound contrast agents flow. We will first explain our simulation model mimicking our experimental device. Then we will introduce this experimental device. Finally, we will detail different imaging methods.

2.1 Imaging Device

The implemented imaging device follows the principle described in Scheme 2.1. A digital signal computed is transmitted to an ultrasound system which has programmable analogue transmitters. The ultrasound probe converts this signal to an ultrasonic wave. It propagates in a medium in which contrast agents can circulate in a pipe. The signal is then collected by the same probe and eventually applied it some post-processing.

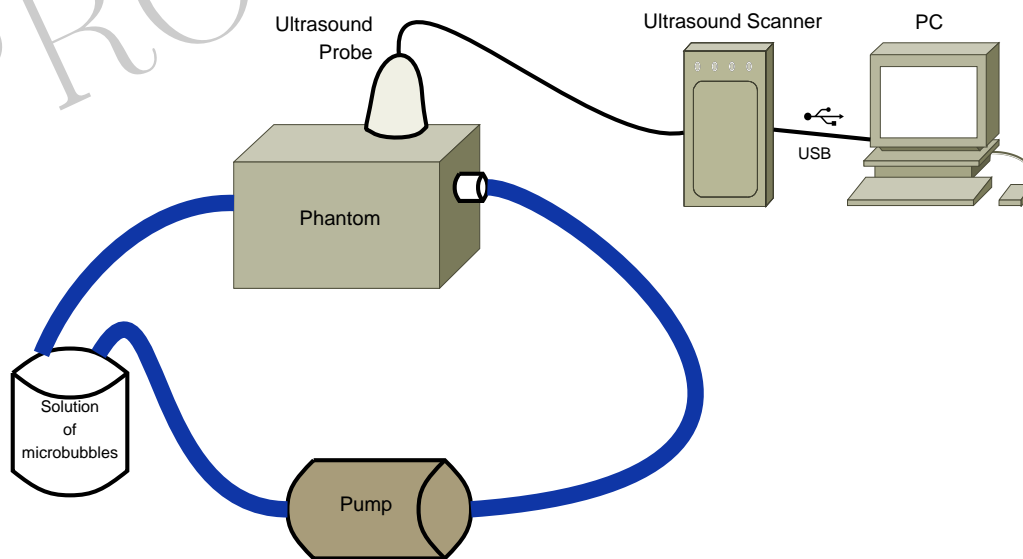


Figure 2.1 – Scheme of the experimental setup

2.1.1 Simulation model

The simulation model follows the same process as the experimental device (Fig. 2.2). We have joined several several existing models (propagation and microbubble) to provide a full model that is able to simulate the process of contrast imaging.

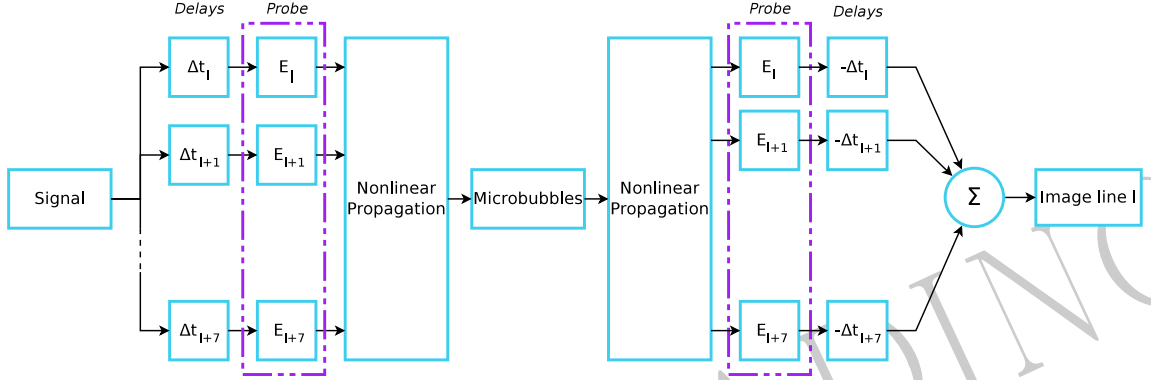


Figure 2.2 – Block diagram of the principle of the simulation model.

2.1.1.1 Excitation

A signal is calculated numerically by using ® (Mathworks, Natick, Massachusetts, USA). This signal is transmitted to the medium to be explored. However, in order to get as close as possible to a real imaging system, it is necessary to add a step of beamforming with a linear sweeping [Szabo, 2004]. Each line of an image is made from eight elements (N_{el}) of the probe so that the wave focuses to 15 mm and with an angle of zero degrees. The signal is duplicated eight times with different delays.

The signals is thus transmitted to the ultrasound probe centred at 3,5 5 MHz with a bandwidth of 63% to -3 . Note that the central frequency f_c of the probe is deliberately chosen lower than the experimental device in order to limit the computation time.

2.1.1.2 Nonlinear Wave Propagation and Medium Explored

The wave then propagates nonlinearly in a medium whose properties have been adjusted to mimic the liver. This medium is defined by two grids (Fig. 2.3): one for the speed c of the wave and the other for the density ρ of the medium. The grid has the properties of liver density ρ_1 and where the speed of the wave is denoted c_1 . In

addition, an 10 mm-diameter artery is at a depth of 15 mm and in which the density ρ_2 is the blood, and when the speed of the wave is denoted c_2 . Each grid point has physical properties chosen randomly according to the Gaussian laws presented in table 2.1. However, the coefficient of nonlinearity B/A is constant throughout the grid with the value 6,7.

Liver	ρ_1	$\mathcal{N}(1050 \text{ kg/m}^3, 30 \text{ kg}^2/\text{m}^6)$
	c_1	$\mathcal{N}(1578 \text{ m/s}, 30 : \text{m}^2/\text{s}^2)$
Blood	ρ_2	$\mathcal{N}(1060 \text{ kg/m}^3, 2.5 \text{ kg}^2/\text{m}^6)$
	c_2	$\mathcal{N}(1584 : \text{m/s}, 2.5 : \text{m}^2/\text{s}^2)$

Table 2.1 – Mechanical properties of the medium to be explored [Szabo, 2004].

The wave propagation in the medium (eq. 2.1 and 2.2) is solved by a model developed by ANDERSON [Anderson, 2000].

$$\rho \frac{\delta^2 u}{\delta t^2} = -\nabla p, \quad (2.1)$$

$$p = -K \left(\nabla \cdot u + \frac{1}{2} \frac{B}{A} (\nabla \cdot u)^2 \right) \quad (2.2)$$

où $K = \rho c^2$.

The solver uses a pseudo-spectral method to compute the spatial derivatives of the pressure and of the speed of wave. Moreover, the equation of the propagation 2.1 is solved by using the ADAMS-BASHFORTH's method at the fourth order [Ghrist et al., 2001]. The values of the pressure and of the speed of wave are updated at each half time step for each point in the space. However the derivative computation in the FOURIER domain can cause GIBBS phenomena [Wojcik et al., 1997]. They are greatly eliminated by applying a perfectly-matched boundary layer). Its effect is to simulate an infinite space.

To introduce the ultrasound contrast agents in the area simulating blood, two passes of propagation computation are required. The first identifies the incident wave for each microbubble. Ten microbubbles are randomly distributed according a Gaussian law near to the focal spot and in the area with the blood properties. Note that for each simulation of a line of the image, ten microbubbles are always placed in the medium in order to enable a RAYLEIGH diffusion. The second pass, after the

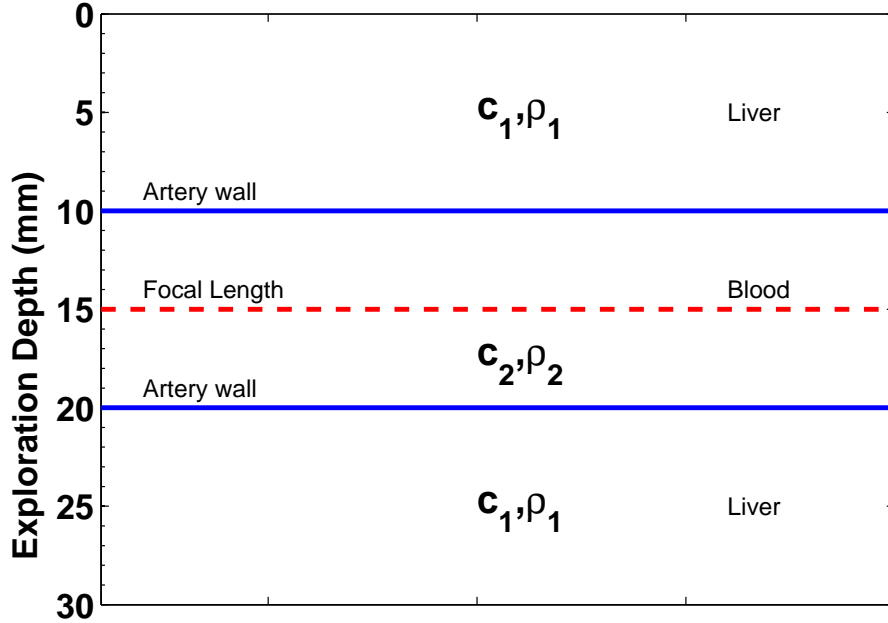


Figure 2.3 – Representation of the grid of speed c of wave speed and of the grid of the density ρ that define the medium to be explored. The ultrasound probe is located at the depth 0 at the top of the representation.

solving of the oscillation of each microbubble, injects the microbubble wave. The signals are recorded in the second pass at the sensor position.

2.1.1.3 Microbubbles

The ultrasound contrast agents simulated are microbubbles encapsulated of SonoVue™ (Bracco Research SpA, Geneva, Switzerland). A phospholipid monolayer imprisons gas of Sulfur hexafluoride (SF_6) [Greis, 2004] whose polytropic exponent κ is 1,095. The microbubbles used had the following properties:

- their diameters are randomly selected according to the distribution shown in Fig. 2.4 with an average diameter $2,5 \mu\text{m}$ [Greis, 2004];
- their average frequency of resonance is 2,6 MHz [van der Meer et al., 2004].

The acoustic response of the contrast agents is computed for a single microbubble by the MARMOTTANT's model [Marmottant et al., 2005] based on the RAYLEIGH-PLESSET [Plesset, 1949] equation modified and polytropic transformation. Radial

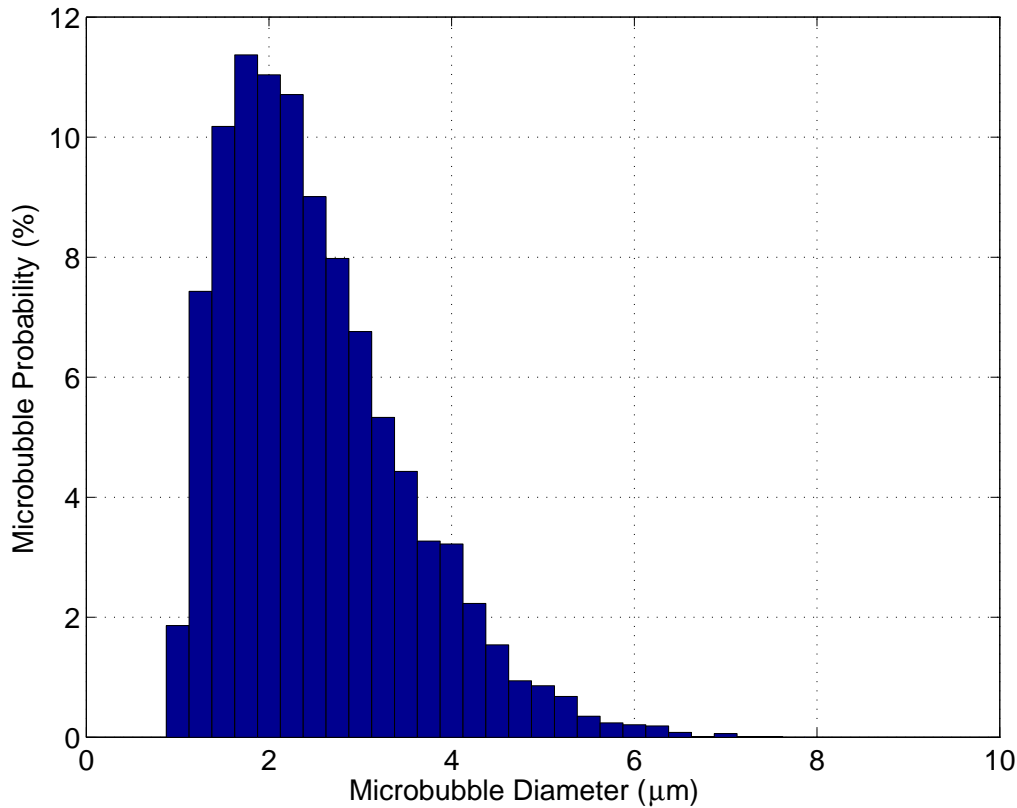


Figure 2.4 – Histogram of the size distribution of microbubbles.

oscillations are not considered because of the assumption of spherical symmetry. The model advantage is to be validated with optical observations of the oscillation of microbubbles SonovueTM. In addition, it takes into account the phenomena of shell buckling and of shell rupture. To do so, the surface tension varies according three states depending on the microbubble surface (Fig. 2.5):

- Buckled state: below a threshold $S_{buckling}$ of the microbubble surface, the microbubble can remain spherical and deforms. The surface tension σ tends to zero;
- Ruptured state: conversely, during the microbubble expansion, the available surface per molecule increases and the surface tension of σ ;
- Elastic state: between these two extreme cases, in the linear regime, the surface tension is described by using the elastic modulus of the shell and the surface of the microbubble [Pauzin, 2009].

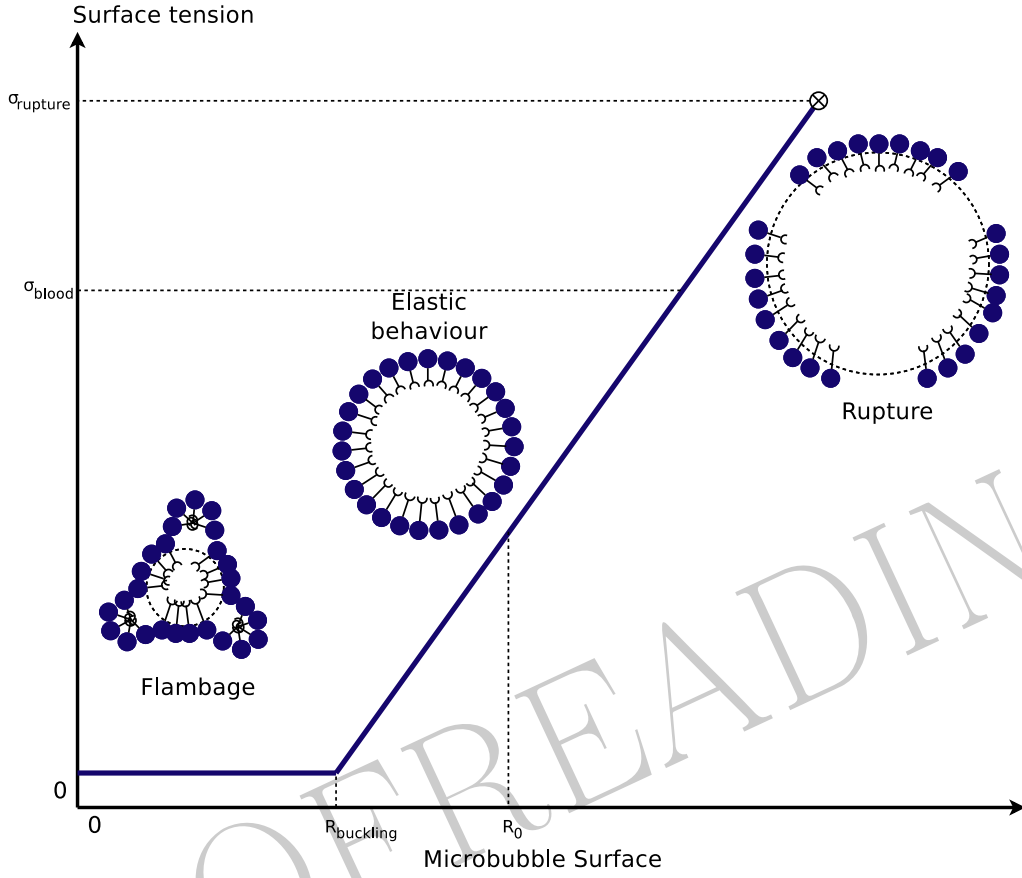


Figure 2.5 – Modelisation of the effective surface tension of a monolayer of phospholipid of a microbubble.

The surface tension describing these three states is described by the equation 2.3:

$$\sigma(R) = \begin{cases} 0 & \text{if } R \leq R_{buckling} \\ \chi \left(\frac{R^2}{R_{buckling}^2} - 1 \right) & \text{if } R_{buckling} \leq R \leq R_{rupture} \\ \sigma_{blood} & \text{if } R \geq R_{rupture} \end{cases}, \quad (2.3)$$

where $\chi = 0,38 \text{ N/m}$, $\sigma_{blood} = 0,058 \text{ N/m}$, $R_{buckling} = R_0$ and $R_{rupture} = 2R_0$.

The dynamic model of the bubble is described by the following equation:

$$\rho_2 \left(R\ddot{R} + \frac{3}{2}\dot{R}^2 \right) = \left[p_0 + \frac{2\sigma(R_0)}{R_0} \right] \left(\frac{R}{R_0} \right)^{-3\kappa} \left(1 - \frac{3\kappa}{c_2} \dot{R} \right) - \frac{2\sigma(R)}{R} - \frac{4\eta_2\dot{R}}{R} - \frac{4\kappa_S\dot{R}}{R^2} - p_\infty(t), \quad (2.4)$$

where the derivatives are denoted with the NEWTON notation, $\kappa_s = 2d_s\eta_{lipid} = 2,4 \cdot 10^{-9}$ N and $p_\infty(t)$ the pressure sum p_0 and $p_{driving}(t)$.

The solving of this model is carried out by the RUNGE-KUTTA's method at the fourth order for the ten microbubbles studied. From NAVIER-STOCKES equations, the pressure at the surface of the microbubble is deducted:

$$p_{bubble}(R) = \rho_2 \left(R\ddot{R} + \frac{3}{2}\dot{R}^2 \right). \quad (2.5)$$

This pressure is transmitted to the microbubble position in the grid of the propagation model.

2.1.2 Experimental Setup

The experimental device is described by the block diagrams 2.1 and 2.6. The transmitted signal is first generated digitally by a computer. Then it is sent to the system. The transmission chain of the ultrasound scanner transmits the signal to the medium by using an ultrasonic probe. This wave propagates the medium constituted of tissus and microbubbles. The reception chain collects the signals and computes a line of the ultrasound image to display.

Let's detail the various important functions of the experimental device.

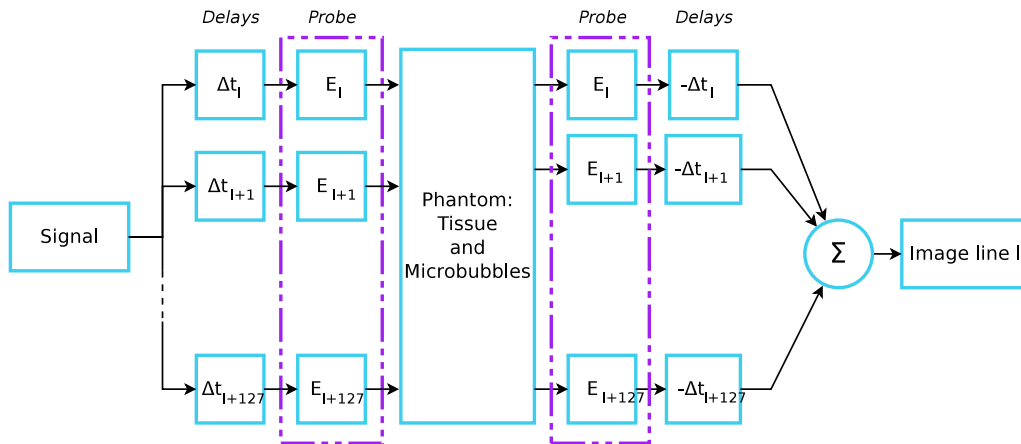


Figure 2.6 – Block diagram of the experimental device.

2.2. CONTRAST IMAGING TECHNIQUES

2.1.2.1 Ultrasound Scanner and Transducers

The excitation signal is sent to an “open” ultrasound scanner (MultiX WM, M2M, Les Ulis, France) via USB. The scanner automatically duplicates the signal for each element of the ultrasound probe. It automatically applies the required delays to obtain a native beamforming of kind of [Szabo, 2004]. The signals are finally transmitted to a linear array of 128 elements (Vermont SA, Tours, France) centred at 4 MHz and with a bandwidth of 53% at -3 dB 3dB. The wave then focuses to 28 mm from the surface.

The transfer time of excitation for a focus is substantial since it requires about two seconds per line (RF). In order to get closer to a time of a real examination, we proposed to achieve our experiments only on an ultrasound image of five lines sweeping angle $0^{\circ}25'$. Thus we want to limit the destruction of microbubbles by reducing the time of the experiment.

2.1.2.2 Medium Explored

The wave propagates through a phantom mimicking tissues (model 524, Peripheral Vascular Flow Phantom, ATS Laboratories Inc., Bridgeport, CT, United States of America). The phantom is penetrated by a tube 4 mm in diameter in which circulates a solution of SonoVueTM diluted $1/2,000^{\text{th}}$.

2.2 Contrast Imaging Techniques

Several imaging methods have been developed in order to enhance the contrast. They follow the principle described by scheme 2.7 shared by all ultrasound imaging. Some methods require step before propagation in the medium. Others are only post-processings. Finally, some are a combination of both.

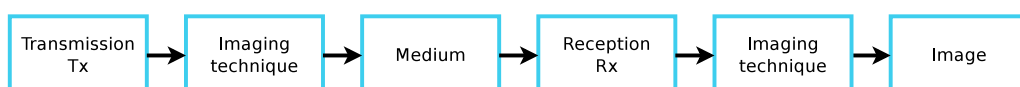


Figure 2.7 – Block diagram of ultrasound imaging.

The non-encoded methods are conceptually easier, since they require only a single excitation to extract the harmonic components in post-processing. Here is a non-exhaustive list:

- second harmonic imaging [Frinking et al., 2000];
- imaging by nonlinear autoregressive filtering [Phukpattaranont and Ebbini, 2003];
- subharmonic imaging [Forsberg et al., 2000];
- superharmonic imaging [Bouakaz et al., 2002].

Other methods are encoding techniques. They use the differences of the nonlinear acoustic signatures between microbubbles and tissues, as for example:

- impulsion inversion [Simpson et al., 1999];
- amplitude modulation [Brock-fisher et al., 1996];
- amplitude and phase modulation [Phillips and Gardner, 2004];
- pulse subtraction [Borsboom et al., 2009];
- harmonic imaging by *chirp*^a [Borsboom et al., 2005];
- reversal *chirps* [Bouakaz, 2008].

In this study, we have chosen to implement several imaging method which we can explain; as for example: imaging by nonlinear autoregressive filtering, pulse inversion imaging, imaging by amplitude and phase modulation, and imaging by chirp inversion.

2.2.1 Harmonic Imaging by Nonlinear Autoregressive Filtering

Harmonic imaging by nonlinear autoregressive filtering is the most widely used non-encoded method. We implemented harmonic imaging by nonlinear autoregressive filter [Phukpattaranont and Ebbini, 2003] because it has better results compared to a simple frequency filtering. The principle of harmonic imaging which consists in a

^aor harmonic imaging by frequency modulation

2.2. CONTRAST IMAGING TECHNIQUES

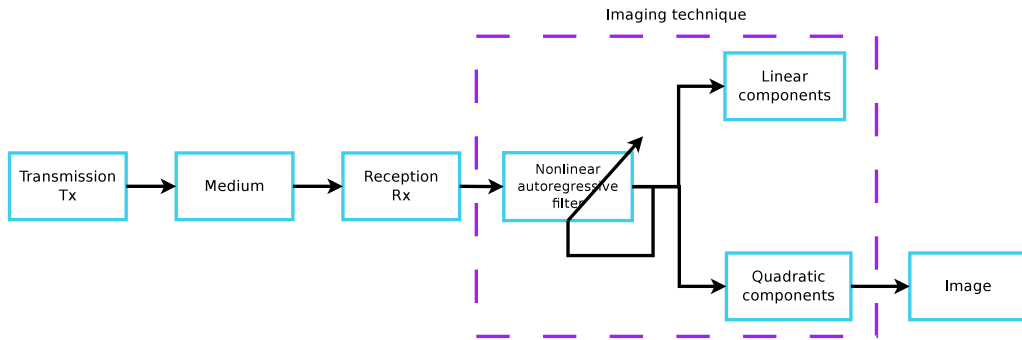


Figure 2.8 – Block diagram of the harmonic imaging by nonlinear autoregressive filtering.

post-processing extraction is the same whatever the method (Fig. 2.8), except for the extraction method itself.

In the case of harmonic imaging, the incident wave propagates at the frequency f_0 . The image is reconstructed from signals which are within the bandwidth around the frequency $2f_0$. The difficulty in these methods lies in the fact that the frequency component to $2f_0$ must come only harmonic components and not from the direct transmission. This is achieved by transmitting signals narrow frequency band (Fig. 2.9) but obviously at the expense of axial resolution of the imaging system.

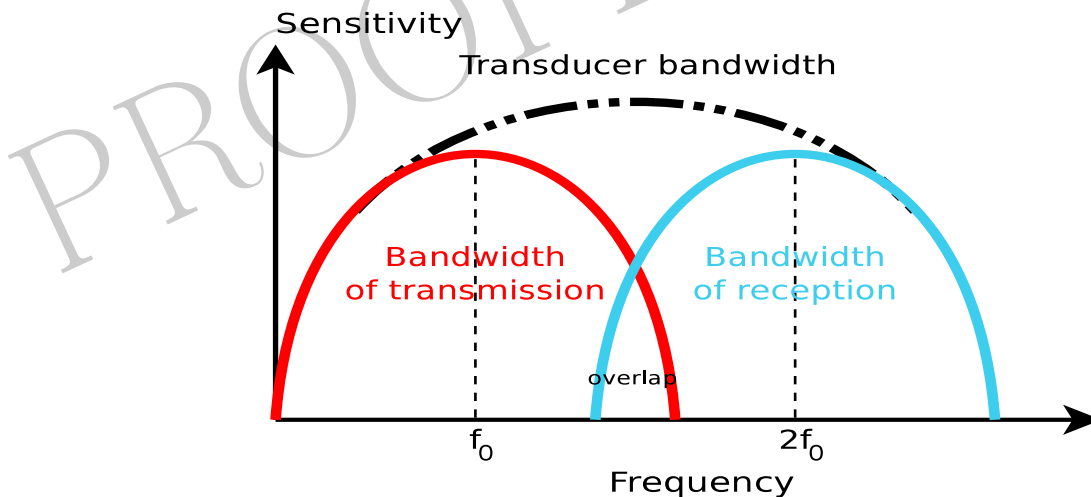


Figure 2.9 – Bandwidth transducer showing the overlap between the transmission bandwidth and the receiver bandwidth for harmonic imaging.

Moreover, the ultrasound propagation is gone along with the generation of harmonic frequency components for sufficiently high acoustic pressures. These nonlinear components are linearly reflected by microbubbles and tissues. They contaminate or hide the nonlinear component at $2f_0$ generated by microbubbles. Thus, all the

contrast imaging methods based on the nonlinearity of microbubbles are damaged because of the residual harmonic component from the tissues. Therefore, the transmitted acoustic amplitude should be reduced to minimize this influence. Although the nonlinear propagation process is undesirable in ultrasound contrast imaging, it was found that tissue imaging harmonic mode is very interesting. Harmonic imaging of tissue, called native harmonic imaging, greatly improves the image quality compared to fundamental imaging method.

Quadratic component extraction of backscattered signal $y(t)$ is performed by using a nonlinear autoregressive filter of second order and with a memory $M = 2^b$. The first step is to describe a synthetic model $\hat{y}(t)$ of the backscattered signal $y(t)$ from its past samples:

$$\begin{aligned}\hat{y}(t) &= z_L(t) + z_Q(t) \\ &= \sum_{i=1}^{M-1} h_L(i)y(t-i) + \sum_{j=1}^{M-1} \sum_{k=j}^{M-1} h_Q(j,k)y(t-j)y(t-k),\end{aligned}\quad (2.6)$$

where h_L and h_Q are linear and quadratic coefficients respectively, z_L et z_Q the signals describing the linear and quadratic components, respectively. For convenience, let's write the filter in matrix form::

$$\hat{y}(t) = \psi^T(t)\mathbf{h}(t), \quad (2.7)$$

with

$$\psi_n^T = [y(t-1), y(t-2), \dots, y(t-M+1), y^2(t-1), y(t-1)y(t-2), \dots, y^2(t-M+1)],$$

$$\mathbf{h} = [h_L(1), h_L(2), \dots, h_L(M-1), h_Q(1,1), h_Q(1,2), \dots, h_Q(M-1, M-1)]^T.$$

The optimal parameter vector \mathbf{h} can be written simply by using a matrix inversion [Golub and van Loan, 1989] such as:

$$\mathbf{h}_{opt} = \Theta^{-1}\mathbf{G}_y, \quad (2.8)$$

with

$$\mathbf{G}_y = [y(t), y(t+1), \dots, y(t+N-1)]^T,$$

^bThis memory is selected to provide a quick data processing and experimental application.

2.2. CONTRAST IMAGING TECHNIQUES

$$\Theta = [\psi(t), \psi(t+1), \dots, \psi(t+N-1)]^T,$$

where N is the number of parameters equals to $\sum_{i=1}^K \frac{(M+i-1)!}{(M-1)!i!}$ with K the filter order and M the filter memory. Note that to increase the robustness of the inversion matrix, a singular value decomposition may be performed. However in cases where the matrix is not invertible, it is necessary to provide a step of regularization.

The identification of the filter coefficients \mathbf{h} can also be achieved by least squares, *i.e.* the minimization of the mean square error MSE between the output $y(t)$ and its estimated $\hat{y}(t)$ such as:

$$\mathbf{h}_{opt} = \min_{\mathbf{h}} MSE = \min_{\mathbf{h}} \mathbb{E} [(y(t) - \hat{y}(t))^2]. \quad (2.9)$$

The optimal parameter vector is then written as follow:

$$\mathbf{h}_{opt} = (\Theta\Theta^T)^{-1} \Theta\mathbf{G}_y. \quad (2.10)$$

Finally, in the case of harmonic imaging by nonlinear autoregressive filtering, the signal used to reconstruct the image is the signal z_Q reconstructed from the coefficients of quadratic components. Note that the signal z_Q describes more nonlinearities than the signal z_L since z_Q is reconstructed from $x^2(t)$ which does not contain the fundamental component.

2.2.2 Pulse Inversion Imaging

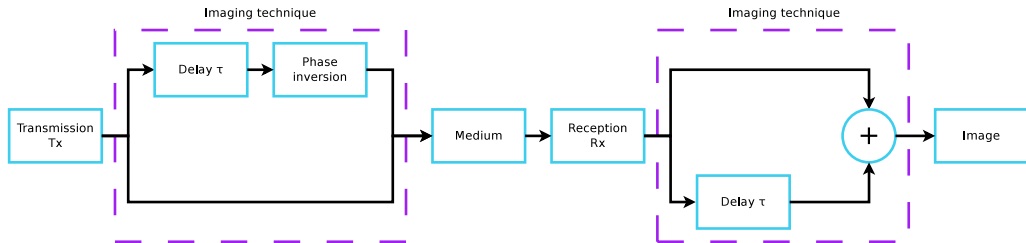


Figure 2.10 – Block diagram of pulse inversion imaging.

Pulse inversion imaging inversion pulse [Simpson et al., 1999] (or phase inversion) is one of the most used to increase the contrast while maintaining good spatial resolution methods. Its principle is described in Fig. 2.10. This technique is based

on the asymmetry of the microbubbles of the oscillations between the compression phase and expansion phase.

A sequence of two successive excitations $x_1(t)$ and $x_2(t)$ is transmitted. The second wave $x_2(t)$, transmitted after an appropriate delay, is a replica but in opposite phase in comparison with the first wave $x_1(t)$. When the medium behaves linearly, the sum of the two echoes is zero, which is no longer true if the nonlinearities of the medium components are composed of even components (Fig. 2.11).

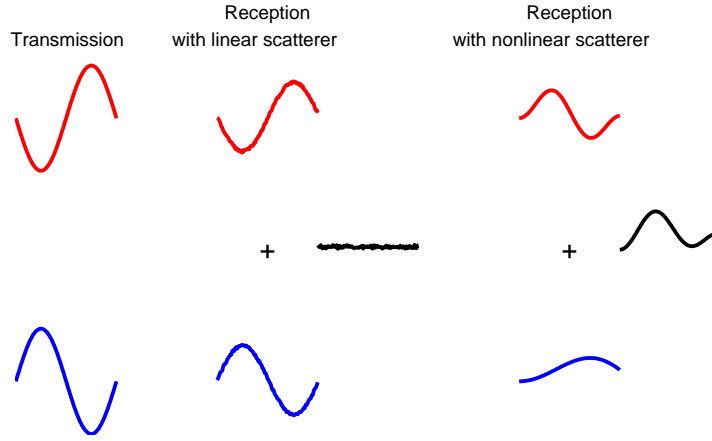


Figure 2.11 – Principle of pulse inversion imaging.

The method thus detects even harmonic components. To demonstrate it, consider a nonlinear system whose output $y(t)$ can be written as a decomposition of power series from the input signal $x(t)$ such that:

$$y(t) = \text{echoe}(x(t)) = \sum_{p=1}^{+\infty} w_p x^p(t) = w_1 x(t) + w_2 x^2(t) + w_3 x^3(t) + \dots, \quad (2.11)$$

where w_p are coefficients amplitudes. Now calculate the sum of echoes for excitations in opposite phases:

$$\begin{aligned} S(t) &= \text{echoe}(x(t)) + \text{echoe}(-x(t)) = \sum_{p=1}^{+\infty} w_p x^p(t) + \sum_{p=1}^{+\infty} w_p (-x(t))^p \\ S(t) &= w_1 x(t) + w_2 x^2(t) + w_3 x^3(t) + \dots - w_1 x(t) + w_2 x^2(t) - w_3 x^3(t) + \dots \\ &= 2w_2 x^2(t) + 2w_4 x^4(t) + \dots \end{aligned} \quad (2.12)$$

2.2. CONTRAST IMAGING TECHNIQUES

Following the same principle, the echo difference $D(t)$ for excitations in opposite phases can extract only the odd harmonics. Moreover, to demonstrate that the pulse inversion only preserves nonlinearities generated by the system, it is possible to assume: the signal $x(t)$ containing several harmonics can be decomposed into several components, *e.g.*, eg $x(t) = a_1x_1(t) + a_2x_1^2(t)$. In this case, the sum only contains some terms from a nonlinear transformation of the system (eq. 2.13). The quadratic components of $x(t)$ undergone a linear transformation are eliminated.

$$\begin{aligned}
 S(t) &= 2w_1x^2(t) + 2w_4x^4(t) + \dots \\
 &= 2w_2 [a_1x_1(t) + a_2x_1^2(t)]^2 + \dots \\
 &= 2w_2a_1x_1^2(t) + 4w_2a_1a_2x_1^3(t) + 2w_2a_2x_1^4(t) + \dots
 \end{aligned} \tag{2.13}$$

The pulse inversion imaging therefore makes possible to increase the detection of microbubbles echoes while minimizing the echoes from the other structures such as tissue. It has the advantage of working on the full band of the transducer, which does not deteriorate the resolution. But the price is reduced the framerate, which makes the method sensitive to movement.

2.2.3 Imaging by Phase and Amplitude Modulation

Imaging by phase and amplitude modulation [Phillips and Gardner, 2004], known as “*Contrast Pulse Sequence*”, is a method which combines the pulse inversion (shown above) and amplitude modulation [Brock-fisher et al., 1996]. It uses a sequence of excitations by varying both amplitude and phase (Fig. 2.12).

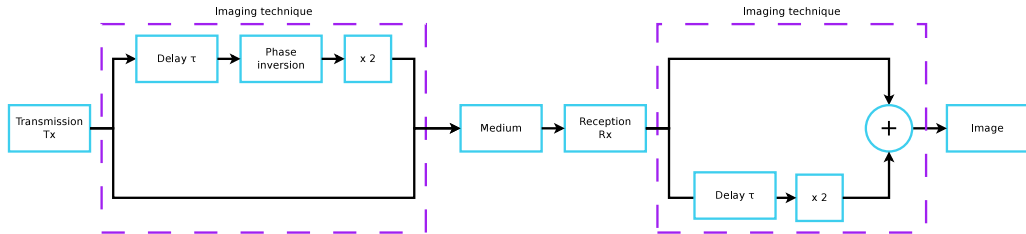


Figure 2.12 – Block diagram of the imaging by phase and amplitude modulation.

Several possible sequences exist. The simplest consists of two excitations $x_1(t)$ and $x_2(t)$. The second wave $x_2(t)$, transmitted after a suitable time, is a replica

of $x_1(t)$ in opposite phase and whose amplitude is double. In this example, the echo of the first excitation $x_1(t)$ is multiplied by two and added to the echo of the second excitation $x_2(t)$. When the medium behaves linearly, this sum is zero, which is not often the case when the reflector is nonlinear as microbubbles. The phase and amplitude modulation only eliminates the fundamental frequency in contrast with the inversion pulse where even or odd components are only kept. To demonstrate this, let us take our hypothesis described by the equation 2.11. Thus the sum of two echoes eliminates the contribution to the fundamental frequency:

$$\begin{aligned}
 S(t) &= 2\text{echo}(x(t)) + \text{echo}(-2x(t)) = 2 \sum_{p=1}^{+\infty} w_p x^p(t) + \sum_{p=1}^{+\infty} w_p (-2x(t))^p \\
 &= 2w_1x(t) + 2w_2x^2(t) + 2w_3x^3(t) + \dots - 2w_1x(t) + 4w_2x^2(t) - 8w_3x^3(t) + \dots \\
 &= 6w_2x^2(t) - 6w_3x^3(t) + \dots
 \end{aligned} \tag{2.14}$$

The method has the advantage of being insensitive to small movements, and especially as the number of pulses in the sequence is high, but at the expense of frame rate [Tranquart et al., 2007a].

2.2.4 Imaging by Frequency Modulation

The last recently years have seen the emergence of imaging methods involving excitations with frequency modulation also called chirp. These imaging methods have the advantage of significantly reducing the pressure level, since the energy is distributed in time. It also makes possible to increase the lifespan of contrast agents. However, to maintain an axial resolution, it is necessary to add a so-called “compression ” step on the reception signal developed for radar systems [Klauder et al., 1960] and suitable for ultrasound imaging [Rao, 1994, Misaridis and Jensen, 2005].

Three methods of imaging using frequency modulation have been developed:

- harmonic imaging by chirp [Borsboom et al., 2003];
- imaging by chirp inversion [Chiao and Hao, 2005];
- imaging by chirp reversal [Bouakaz, 2008].

2.2. CONTRAST IMAGING TECHNIQUES

The first, harmonic imaging by chirp is the simplest. The excitation of microbubbles is a sinusoid frequency-modulated by a law such as $f(t) = f_0 + \beta_1 t$. Finally, the echo is compressed by a matched filter around $2f_0$. This step consists in applying a filter whose impulse response is also sinusoidal frequency-modulated but with a law $f(t) = 2f_0 - 2\beta_1 t$. At low levels of pressure, the frequency modulation can significantly increase the nonlinearities in comparison to a excitation with the same bandwidth but without modulation.

The second method, imaging by chirp inversion, combines the frequency modulation and pulse inversion imaging. It has already been applied to tissue imaging, but not in contrast imaging. The principle is identical to the inversion pulse. The first wave x_1 is frequency modulated and transmitted to the medium. Then a second wave x_2 is modulated with the same law, but in opposite phase in comparison to x_1 . Each of the respective echoes y_1 and y_2 is compressed with a matched filter for each $y_{1,c}$ and $y_{2,c}$. The image is made from the sum of compressed signals $y_{1,c}$ et $y_{2,c}$.

The third, imaging by chirp reversal, also uses coded excitations. A first excitation $x_1(t)$ is modulated with a law such as $f(t) = f_0 + \beta_1 t$. A second excitation $x_2(t)$ is modulated but with an opposite slope such that $f(t) = f_0 - \beta_1 t$ and transmitted after an appropriate delay. Each of the signals is compressed with the matched filter that suits its for $y_{1,c}$ and $y_{2,c}$ respectively for the first and second echoes. The image is made from the difference between the signals $y_{1,c}$ and $y_{2,c}$.

PROOFREADING

Chapter 3

Optimal Command by Signal Families

ULTRASOUND harmonic contrast imaging has a large number of methods to enhance contrast. However, these techniques have difficulties to ensure both good spatial resolution and good contrast. According to the medical application, this compromise may have the advantage of contrast or of resolution. For example, in contrast echocardiography, contrast is preferred even if resolution decreases [Burns, 2002].

Anyway, the setting parameters of the system are crucial, because they require *a priori* knowledge of the medium, of the system and of the transducer. Indeed, there are many unknowns such as:

- the pressure level is not accessible in the tissues, since the effects of diffraction and of attenuation can vary from one patient to another;
- the level and number of nonlinear components created during tissue propagation are unknown according to depth, as they can vary with depth of exploration.

Moreover, most techniques do not allow the clinical examination to adjust itself to changes in:

- the microbubble concentration which evolves during the examination and which remains inaccessible, hence unknown [Becher and Burns, 2000];
- the distribution of the microbubble sizes which is not known with precision and which changes during the examination [Soetanto and Chan, 2000].

In order to solve this problem, new innovative imaging methods must guarantee an optimal contrast automatically throughout the examination duration. In this chapter, we propose to take up this challenge.

In this chapter, we propose an imaging system which optimizes the *CTR* (*Contrast-to-Tissue Ratio*) and which can select the system parameter \mathbf{w} automatically among a solution family::

$$\max_{\mathbf{w}} (CTR), \quad (3.1)$$

The *CTR* is defined as the ratio between the backscattered power of the medium perfused by the microbubbles and the backscattered power of the non-perfused medium [Phukpattaranont and Ebbini, 2003] such as:

$$CTR_k = \frac{\frac{1}{N_l \cdot t_1} \sum_{l=1}^{N_l} \sum_{t=t_0}^{t_1} z_{k,l}(t)^2}{\frac{1}{N_l \cdot t_3} \sum_{l=1}^{N_l} \sum_{t=t_2}^{t_3} z_{k,l}(t)^2}, \quad (3.2)$$

where N_l is the line number of the image, $z_{k,l}(t)$ the l -line of the image after post-processing (including imaging techniques) at the optimization iteration k . The two areas are delimited by the limits $[t_0, t_1]$ axially for the medium perfused by the microbubbles, and the limits $[t_2, t_3]$ for the non-perfused medium.

We hypothesize that it exists a suitable choice of the excitation parameters (frequency, amplitude, phase, duration, energy, *etc.*) which can optimize the contrast without prior knowledge of the medium, the transducer and the parameters of excitation [Ménigot et al., 2009]. Moreover, we also assume that the region perfused by the microbubbles is already identified. We detected the zones manually. But this detection could, for example, be automated by a segmentation method adapted to ultrasound imaging [Tauber, 2005]. Finally, the method must be independent of the simulation model or the experiments performed, in absolute terms.

3.1 Methods

Our method follows the principle described by the diagram 3.1 where we have added a feedback to loop the ultrasound imaging system. In addition, this work is in

3.2. OPTIMAL COMMAND BY FAMILY OF TRUNCATED HALF-SINE WAVES

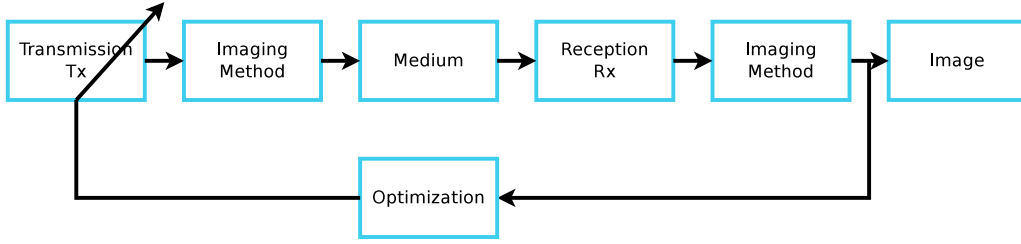


Figure 3.1 – Block diagram of closed-loop ultrasound imaging.

the context of ultrasound contrast imaging. This configuration has the advantage of being able to easily identify a quality criterion of the image (for example the contrast). Indeed, the region of interest containing the microbubbles is easily identifiable. However, this principle remains true apart from the context of ultrasound contrast imaging.

We restricted our choice to two signal families. These choices seem to be the most relevant given the results presented in the literature. The first family consists of truncated half-sinusoids and the second is a family of sinusoids modulated in frequency.

3.2 Optimal Command by Family of Truncated Half-Sine Waves

The starting point of our study has its origin in the work of the analytical optimization of contrast in pulse inversion of impulses [Reddy and Szeri, 2002]. This solution being analytical, we have apprehended this solution from a suboptimal point of view. To approximate the analytical waveform (Fig. 3.2), we propose to cut a period of the wave into two truncated half-sine waves with respective amplitudes A_1 and A_2 and with respective durations T_1 and T_2 .

The system command is computed numerically and iteratively. The parameters which describe the truncated half-sine waves are determined at each iteration k . The signal consists of several cycles of a sub-optimal wave (for example, the curve in green dotted line in Fig. 3.2) and is modulated by a [Tranquart et al., 2007b] such as:

$$x'_{k,\varphi}(t) = \exp \left[- \left(\frac{2(f_{1,k} + f_{2,k})t}{N_c} \right)^2 \right] \xi_{k,\varphi}(t), \quad (3.3)$$

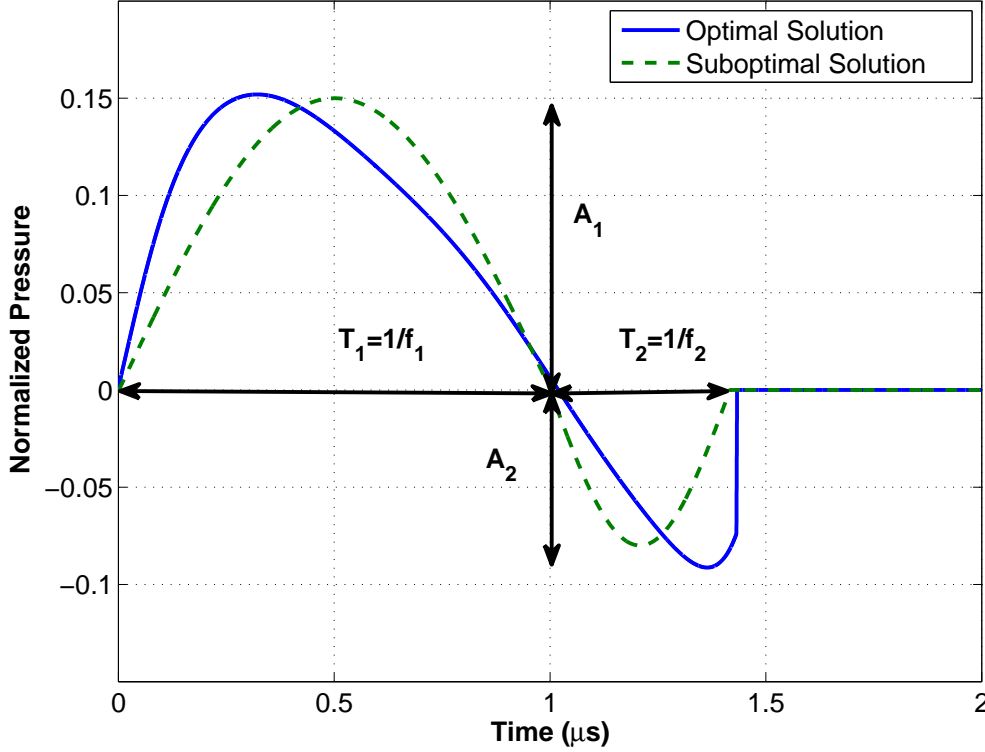


Figure 3.2 – Optimal solution computed analytically [Reddy and Szeri, 2002] and sample suboptimal solution defined for our family of truncated half-sine waves.

where k is the optimization iteration, t the time and $f_{1,k} = 1/T_{1,k}$, respectively $f_{2,k} = 1/T_{2,k}$, are the frequencies of the truncated first half-sine wave, respectively of the truncated second sine wave, at the k iteration. The number of cycles of the excitation N_c is chosen as a function of the imaging method. Thus, for a non-coded method such as harmonic imaging by nonlinear autoregressive filtering, because of the need for a restricted bandwidth, the cycle number N_c is equal to four, *i.e.* 50% of relative bandwidth^a at the center frequency f_c of the transducer. In coded methods, the cycle number is set to 2.3, or 100 % of the bandwidth relative to the center frequency f_c of the transducer.

The signal $\xi_k(t)$ represents the signal composed of the two truncated half-sine waves not modulated by the Gaussian and defined by equation 3.4:

$$\xi_{k,\varphi}(t) = \xi_{1,k,\varphi}(t) - \xi_{2,k,\varphi}(t), \quad (3.4)$$

^aThe relative bandwidth is defined as the percentage of the signal bandwidth in the transducer bandwidth

3.2. OPTIMAL COMMAND BY FAMILY OF TRUNCATED HALF-SINE WAVES

where $\xi_{1,k,\varphi}(t)$, respectively $\xi_{2,k,\varphi}(t)$ are the two truncated half-sine waves described in equations 3.5 and 3.6.

$$\left\{ \begin{array}{l} \xi_{1,k,\varphi} = \sin\left(\frac{2\pi t}{T_{1,k}} + \phi_\varphi\right) \sum_{i=-\infty}^{+\infty} \text{Rect}_{\frac{T_{1,k}}{2}} \left[t - i \frac{T_{1,k}}{4} \right], \\ \xi_{2,k,\varphi} = \alpha_k \sin\left(\frac{2\pi(t - \frac{T_{1,k}}{2})}{T_{2,k}} + \phi_\varphi\right) \sum_{i=-\infty}^{+\infty} \text{Rect}_{\frac{T_{2,k}}{2}} \left[t - i \left(\frac{T_{1,k}}{2} + \frac{T_{2,k}}{4} \right) \right], \end{array} \right. \quad (3.5)$$

where $\alpha_k = A_{1,k}/A_{2,k}$, $\text{Rect}_{T_l}(t - T_c)$ is a rectangle function centred in T_c with a width of T_l , the phase ϕ_φ is zero if $\varphi = 1$ and $\phi_\varphi = 180^\circ$ if $\varphi = 2$. However, for non-coded methods, ϕ_φ is always zero (or $\varphi = 1$).

Then, the pressure level A is set so that the energy of the excitation $x_k(t)$ is constant such as:

$$A_k \cdot A_{1,k} = \sqrt{\frac{A_0^2 \cdot P_{x_{ref}}}{P_{x'_{k,\varphi}}}}, \quad (3.7)$$

where A_0 is the pressure level of the reference signal x_{ref} . This signal x_{ref} is computed at the central frequency f_c of the transducer. Its power $P_{x_{ref}}$ is the reference power. The power of the transmitted wave is then constant by adjusting the amplitude of the signal:

$$x_{k,\varphi}(t) = A_k \cdot A_{1,k} \cdot x'_{k,\varphi}(t). \quad (3.8)$$

This signal $x_k(t)$ constitutes the excitation of the imaging system to optimize the CTR (equation 3.2).

In this section, we present our results obtained in optimal empirical and automatic command for simulations and experiments. We aggregated the results by imaging methods. We first start with harmonic imaging obtained by nonlinear autoregressive filtering, then by pulse inversion imaging and finally by phase modulation and amplitude imaging.

To show the feasibility of our approach, we begin by presenting the simplest method to know the harmonic imaging by nonlinear autoregressive filtering. Then, we explore the possibilities of optimization with the second imaging method. Finally, the last imaging method allows us to demonstrate that our method can be adapted to all imaging methods. The various optimizations are summarized in the following table:

Optimization Parameters	HI-NAR	PI	CPS
f_0	empirical and automatic	empirical and automatic	empirical and automatic
f_1, f_2	empirical and automatic	empirical and automatic	empirical and automatic
α with $f_{1,opt}$ and $f_{2,opt}$	empirical and automatic	empirical and automatic	empirical and automatic
f_1, f_2 and α	automatic	automatic	automatic

Table 3.1 – Optimizations for the family of truncated sine waves (HI-NAR: harmonic imaging by nonlinear autoregressive filtering, PI: pulse inversion imaging, CPS: phase modulation and amplitude imaging).

3.2.1 Harmonic Imaging by Nonlinear Autoregressive Filtering

To demonstrate the feasibility of our method, we propose to carry out a series of simulations and an experimentation. We demonstrate, through simulations, the optimality of our closed loop system in two steps:

1. we empirically check that the cost function (the CTR) has a global maximum;
2. we check that the system automatically looks for the parameters of the excitation.

To compare with non-optimized imaging, we chose two values of excitation frequencies f_0 usually chosen empirically: the central frequency f_c of the transducer and two-thirds of this same frequency [Hossack et al., 2000]. Finally, we validate our concept through experimental measurements.

3.2.1.1 Setting of the Excitation Frequency

This first optimization is the simplest case, since we hypothesize that the CTR is a function of the excitation frequency f_0 with $f_0 = f_1 = f_2$ and $\alpha = 1$. The expression of the excitation signal is therefore defined by the following equation:

$$x_{k,\varphi}(t) = A \cdot \exp \left[-\frac{\pi f_{0,k} t}{N_c} \right] \sin (2\pi f_{0,k} t + \phi_\varphi), \quad (3.9)$$

3.2. OPTIMAL COMMAND BY FAMILY OF TRUNCATED HALF-SINE WAVES

with, for this imaging method, $\varphi = 1$ and therefore $\phi_\varphi = 0$.

We begin by showing our results of simulations, then our experimental results.

The Fig. 3.3 presents the empirical and automatic optimizations of the excitation frequency $f_{0,k}$ for different pressure levels A_0 .

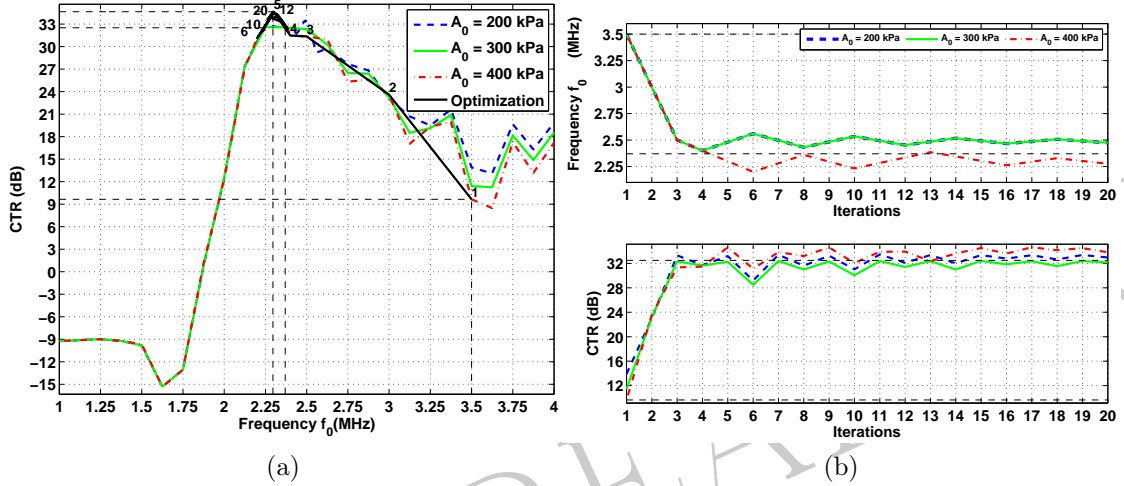


Figure 3.3 – Simulations of optimizations using the excitation frequency f_0 in harmonic imaging by nonlinear autoregressive filter for different pressure levels A_0 . (a) Empirical investigations of the CTR maxima as a function of the excitation frequency $f_{0,k}$. The automatic optimization path for the pressure level $A_0 = 400$ kPa is depicted in black. (b) Automatic search of the CTR using the excitation frequency $f_{0,k}$ by an algorithm using the gradient.

In a first step, a first simulation, shown in Fig. 3.3a empirically searches for the excitation frequency that optimizes the CTR for different pressure levels A_0 (from 200 to 400 kPa). We observe the following points:

- first, the CTR have a global maximum whatever the pressure level. This property is interesting because it facilitates an automatic search by a gradient based algorithm;
- secondly, the frequency of this global maximum changes slightly with the pressure level. We attribute this variation to the resonance frequency of the microbubbles, which depends on the pressure level. However, the effects of the transducer bandwidth limit the measurement of nonlinearities, causing a slight variation in the optimal frequency $f_{0,opt}$;
- Third, the different pressure levels A_0 provide a equivalent CTR . Indeed, for a lower pressure level, the nonlinearities of the microbubbles and the tissue are low. When the pressure level is higher, the nonlinearities of the tissue increase

to the detriment of the nonlinearities of the microbubbles, which does not increase the CTR . Thus, the maximum values of CTR are between 32.2 dB and 34.5 dB, for pressure levels A_0 from 200 to 400 kPa. The corresponding gains are about 2.35 dB over the CTR obtained at two-thirds of the central frequency f_c .

In the second step, an automatic search of this maximum is carried out by the gradient algorithm described in appendix A.1. The results are presented in Fig. 3.3b. We have copied the CTR evaluated at each iteration k in bottom. At the top of the Fig. 3.3b, we have plotted the evolution of the excitation frequency $f_{0,k}$ during iterations k . The automatic optimization finds the maximum of CTR . The excitation frequency $f_{0,k}$ converges to a stable value after six iterations, whatever the pressure level A_0 . Moreover, as an illustration, Fig. 3.3a shows the twenty iterations that confirm the convergence after the first six iterations. Similarly, the CTR reached its maximum when the excitation frequency converged. Note that the values of the CTR and the gain obtained automatically do not have “bias” compared to those obtained empirically during the first simulation.

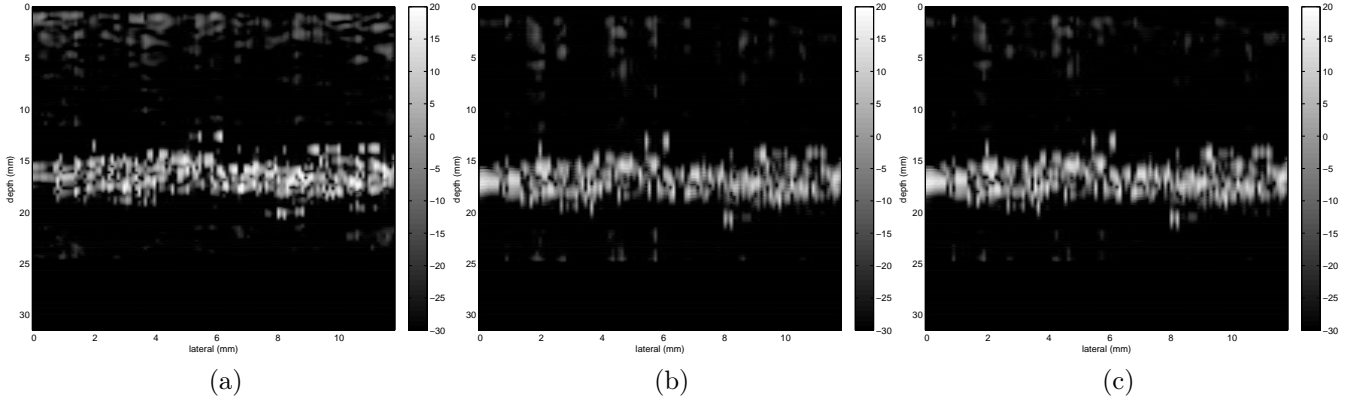


Figure 3.4 – Synthetic images in harmonic imaging by nonlinear autoregressive filter for a pressure level of $A_0 = 400$ kPa where the excitation frequency f_0 is (a) the center frequency f_c of the transducer ($f_c = 3.5$ MHz), (b) the two-thirds of the center frequency f_c of the transducer ($2/3f_c = 2.33$ MHz), (c) the optimal frequency ($f_{0,opt} = 2.28$ MHz).

In summary, these results confirm the presence of a CTR maximum at about 34 dB that can be retrieved automatically. The strong point of our method is that no *a priori* knowledge is required, except for the choice of the first three frequencies that condition the speed of convergence. To our great surprise, the optimum obtained

3.2. OPTIMAL COMMAND BY FAMILY OF TRUNCATED HALF-SINE WAVES

is not at the recommended empirical frequencies (the central frequency f_c of the transducer and two-thirds of this frequency).

As an illustration, Fig. 3.4 shows synthetic images for the three frequencies: the central frequency f_c of the transducer, two-thirds of the center frequency f_c of the transducer and the optimal frequency $f_{0,opt}$ for a pressure level A_0 of 400 kPa. Note that all the images presented have also undergone a logarithmic compression.

In the first image at the frequency f_c , the tissue is highly visible, reducing the contrast. The two latter (at frequencies $2/3f_c$ and $f_{0,opt}$) reduce the contribution of the tissue while enhancing the signal from the microbubbles. The third image at $f_{0,opt}$ slightly increases the contrast by reducing a little more the contribution of the tissue (upper and lower parts of the image).

To confirm the good results of simulations, we present the experimental results. The excitation is chosen with a pressure level A_0 of 400 kPa at the focal length.

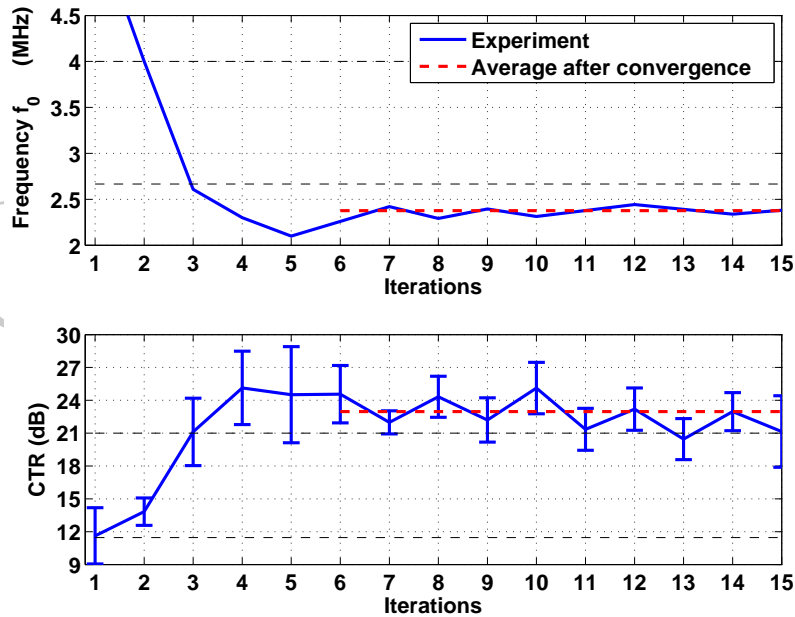


Figure 3.5 – Experiment of automatic optimization using the frequency of excitation f_0 in harmonic imaging by nonlinear autoregressive filter by a gradient algorithm.

The experimental results, presented in Fig. 3.5, show the evolution of the excitation frequency $f_{0,k}$ and of the CTR during the iterations. The CTR converges to its optimal value after six iterations for an excitation frequency $f_{0,k}$ of 2.38 MHz. The mean CTR after convergence is about 23 dB, *i.e.* an average gain of 2 dB compared to two-thirds of the center frequency f_c of the transducer.

3.2.1.2 Setting of the Frequencies of Truncated Half-Sine Waves

Now, we propose to add an additional degree of freedom by introducing the simultaneous search of the frequencies f_1 and f_2 of the two truncated half-sine waves. We start with an empirical search, then with an automatic search. We observe performance on synthetic images.

Fig. 3.6 shows an empirical search of the CTR as a function of as a function of the frequencies of the truncated half-sine waves $f_{1,k}$ and $f_{2,k}$, for a pressure level A_0 of 400 kPa. The function has many local maxima, which does not facilitate a robust automatic search. The empirical optimum is computed for $f_{1,opt} = 2.89$ MHz and $f_{2,opt} = 2.26$ MHz. This CTR maximum is greater by 5.4 dB than that obtained by the only optimization of the frequency $f_{0,opt}$.

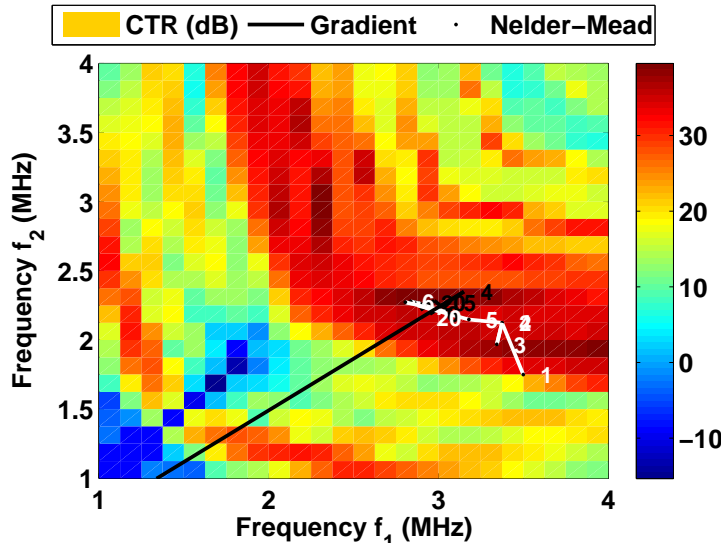


Figure 3.6 – Simulation of the empirical search of the CTR maximum as a function of the frequencies f_1 and f_2 of the truncated half-sine waves in harmonic imaging by nonlinear autoregressive filter for a pressure level $A_0 = 400$ kPa. The automatic searches are reported in black for the gradient algorithm and in white for the NELDER-MEAD algorithm.

Fig. 3.7 presents the automatic optimizations for different pressure levels A_0 by the gradient algorithm (appendix A.1) and the NELDER-MEAD algorithm (appendix A.2). These algorithms find the maximum identified during the empirical search. However, it is necessary to correctly initialize the algorithms and in particular the gradient algorithm, in order to find the global maximum. Note that we have reported

3.2. OPTIMAL COMMAND BY FAMILY OF TRUNCATED HALF-SINE WAVES

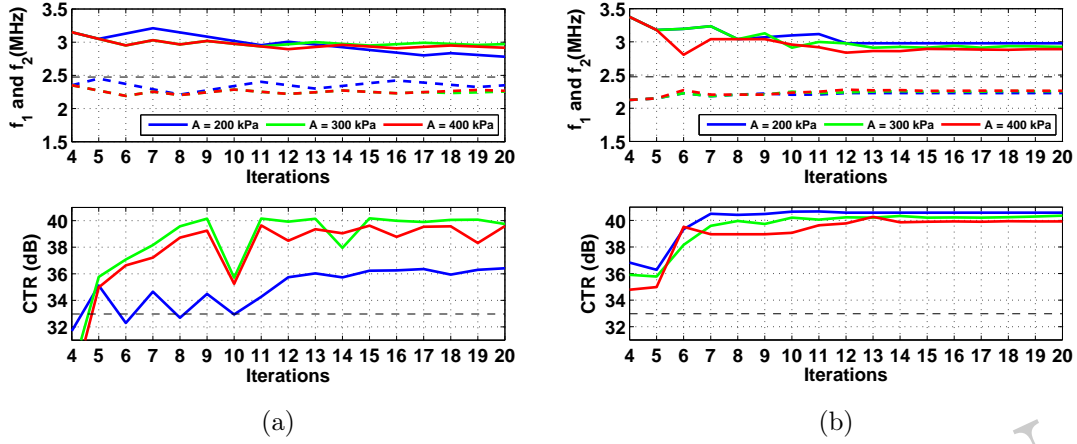


Figure 3.7 – Simulations of the automatic optimizations using the frequencies f_1 and f_2 of the truncated half-sine waves in harmonic imaging by nonlinear autoregressive filter for different pressure levels A_0 by the algorithm based on the gradient (a) and the NELDER-MEAD (b). The frequencies f_1 are written in solid lines, while the frequencies f_2 are dotted.

the automatic optimizations by a black line for the gradient algorithm, and by a white line for the NELDER-MEAD algorithm in Fig. 3.6.

On the basis of these results, we compute a new suboptimal synthetic image (Fig. 3.8).

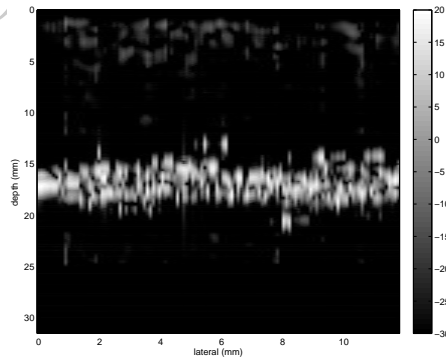


Figure 3.8 – Synthetic image in harmonic imaging by nonlinear autoregressive filter for a pressure level of $A_0 = 400$ kPa and with the optimal values of $f_{1,opt}$ and $f_{2,opt}$.

Unfortunately, we were not able to experimentally test this configuration and the subsequent ones because of the limitations of our experimental setup. Indeed, these optimizations require several CTR measurements by iterations, which increases the experimentation duration. Our experimental device does not allow us to realize measurements in real time.

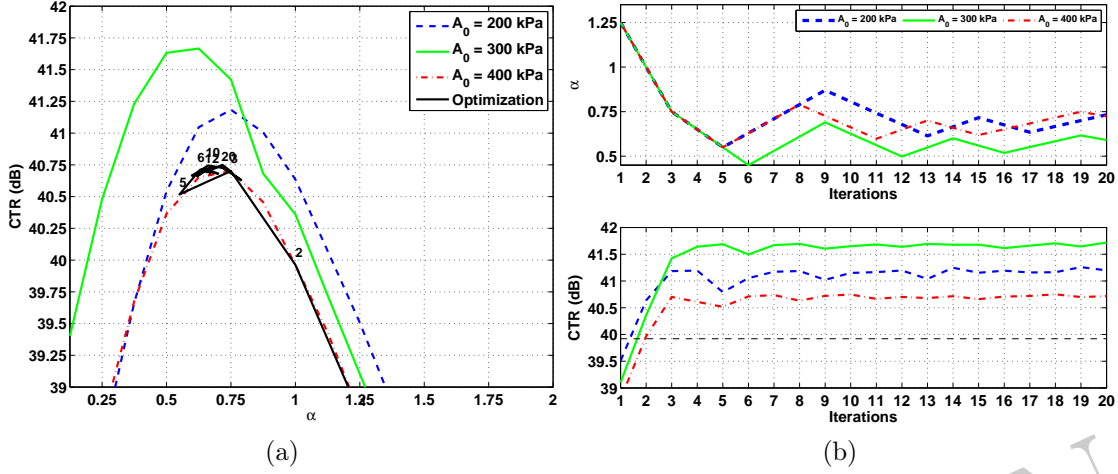


Figure 3.9 – Simulations of the optimizations using the amplitude ratio α ratio in harmonic imaging by nonlinear autoregressive filter for different pressure levels A_0 . (a) Empirical searches of the CTR maxima as a function of α . The automatic optimization path for the pressure level $A_0 = 400$ kPa is marked in black. (b) Automatic search of CTR using α by an algorithm using the gradient.

3.2.1.3 Setting of the Amplitude Ratio Between the Truncated Half-Sine Waves

As the other configurations, the hypothesis on which our study is based is that there is an global maximum of the cost function, here the CTR . Our goal is to check this hypothesis.

This configuration consists in finding the coefficient α which sets the amplitude ratio between the truncated half-sine waves, while keeping in memory the optimal values of the frequencies $f_{1,opt}$ and $f_{2,opt}$ of the previous optimization. So when α is less than 1, A_1 is greater than A_2 ; and reciprocally when α is greater than 1.

We start with an empirical search of the ratio α that maximizes the CTR . Fig. 3.9 shows the empirical and automatic optimizations of the amplitude ration α for different pressure levels A_0 .

On Fig. 3.9a, we observe that the CTR has a global maximum whatever the pressure level A_0 (from 200 to 400 kPa).

The automatic search for this maximum is carried out by the gradient algorithm and is presented in Fig. 3.9b. At the bottom of Fig. 3.9b, the CTR is evaluated on each iteration k . At the top of Fig. 3.9b, the evolution of α_k is depicted during iterations k . Automatic optimization finds the maximum of CTR . As an illustration illustration, Fig. 3.9a shows the first twenty iterations. The gain obtained by

3.2. OPTIMAL COMMAND BY FAMILY OF TRUNCATED HALF-SINE WAVES

optimizing the amplitude ratio varies from 1.31 dB to 0.74 dB for pressure levels A_0 respectively from 200 to 400 kPa.

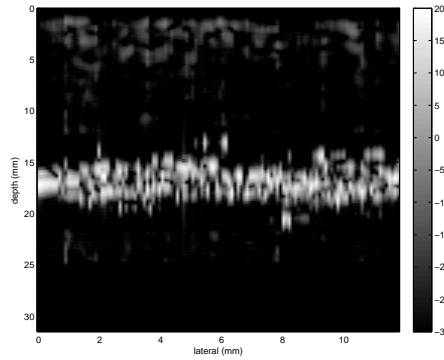


Figure 3.10 – Synthetic image in harmonic imaging by nonlinear autoregressive filter for a pressure level of $A_0 = 400$ kPa and with the optimal values of $f_{1,opt}$ and $f_{2,opt}$, and after optimization of α .

Given the small CTR gain obtained with an optimization of the amplitudes in comparison with an optimization without amplitudes, the synthetic image 3.10 is very close to the image shown in Fig. 3.8.

3.2.1.4 Setting of the Frequencies and the Amplitude Ratio of the Truncated Half-Sine Waves

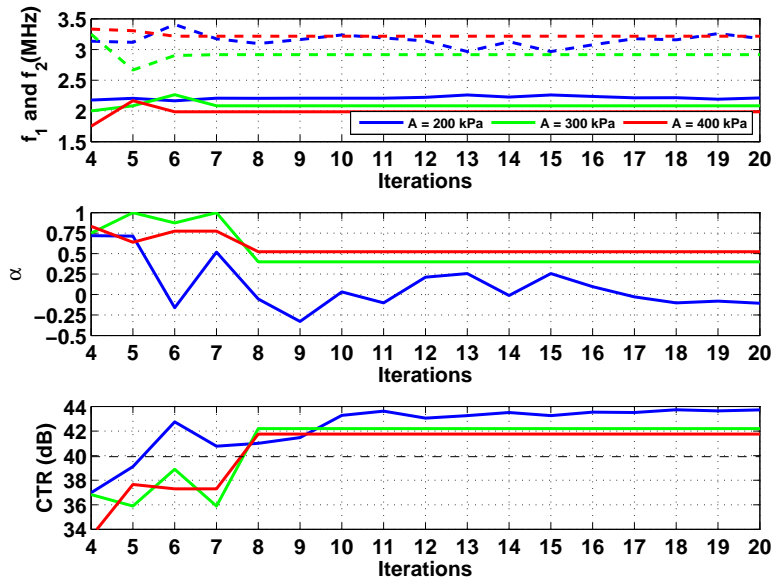


Figure 3.11 – Simulations of automatic optimizations using the frequencies f_1 and f_2 , and the amplitude ratio α in harmonic imaging by nonlinear autoregressive filter for different pressure levels A_0 . The frequencies f_1 are written in solid lines, while the frequencies f_2 are dotted.

This automatic setting can also be set simultaneously. We perform this simulation using the NELDER-MEAD algorithm . Fig. 3.11 shows the CTR as a function of the iterations k at the bottom and the parameters at the top in both figures. In only about fifteen iterations, this optimization can determine the optimal parameters that maximize the CTR .

The results show that it is still possible to maximize the CTR by simultaneously adjusting the frequencies f_1 , f_2 and the amplitude ratio α . Note that contrary to the cases presented in Fig. 3.7, the frequency f_1 is lower than the frequency f_2 .

The synthetic image associated with this maximum is shown in Fig. 3.12.

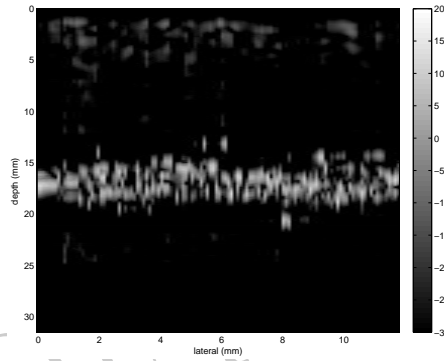


Figure 3.12 – Synthetic image in harmonic imaging by nonlinear autoregressive filter for a pressure level of $A_0 = 400$ kPa after optimization of f_1 , f_2 and α .

3.2.1.5 Discussions

The settings of parameters of the truncated half-sine waves in harmonic imaging by nonlinear autoregressive filtering is performed automatically and without taking into account the system knowledge (tissue, microbubble or transducer). It optimizes the CTR while ensuring optimal adjustment of the nonlinear autoregressive filter (table 3.2).

Optimization Parameters	f_0	f_1, f_2	α with $f_{1,opt}$ and $f_{2,opt}$	f_1, f_2 and α
CTR (dB)	34.49	39.92	40.72	41.75

Table 3.2 – Optimal CTR of simulations in harmonic imaging by nonlinear autoregressive filter according to different optimal settings for a pressure level A_0 of 400 kPa.

3.2. OPTIMAL COMMAND BY FAMILY OF TRUNCATED HALF-SINE WAVES

Conventionally, only an empirical adjustment of the frequency is realized and based on the knowledge of the transducer features (central frequency f_c and bandwidth). However, the empirical settings never take into account the imperfections of the transducer. In addition, the properties of the explored medium are ignored in the setting choice. Our method of automatic adjustment accommodates these unknowns. It is made from objective measurements to optimize an image criterion, such as contrast. It finds the optimal setting that is difficult to predict analytically.

One or more parameters can be set. The optimal choice of frequencies f_1 and f_2 seems to be the most efficient in comparison with the complexity of the optimization. The adjustment of the amplitudes does not bring a gain as large, given the restricted bandwidth of the transducers.

Finally, a real-time implementation can be envisaged in view of the low calculation time of the optimization. However, there are several disadvantages. First, it is necessary to have a programmable analogue transmitter. Secondly, although our technique can propose optimal parameters for each line of the image, it is preferable to perform optimization on the whole image. The image is thus more homogeneous with a single resolution.

3.2.2 Imaging by Pulse Inversion

This second imaging method is the most used technique. It is therefore important to confirm the previous results. Moreover, a first study has already shown its interest in optimal command [Mleczko et al., 2007].

To demonstrate the feasibility and the interests of our method, we propose to carry out a series of simulations and an experimentation. We will demonstrate, through simulations, the optimality and the adaptability of our closed loop system in three steps:

1. we check empirically that the cost function (the *CTR*) does have an global maximum;
2. we check that the system automatically searches for optimal excitation parameters;

3. we check that with a variation of the microbubble population, our adaptive system automatically provides the best CTR during the full examination duration.

Finally, we validate our concept through experimental measurements.

3.2.2.1 Setting of the Excitation Frequency

This first optimization, the simplest, is based on the same principle as before with the optimization in harmonic imaging by nonlinear autoregressive filtering. Note, however, that the CTR we want to maximize operates on the pulse inversion summation signal. First, we will begin by confirming the existence of a maximum and its automatic search. Then we will check the adaptive nature of our method. Finally, we will integrate an axial resolution constraint.

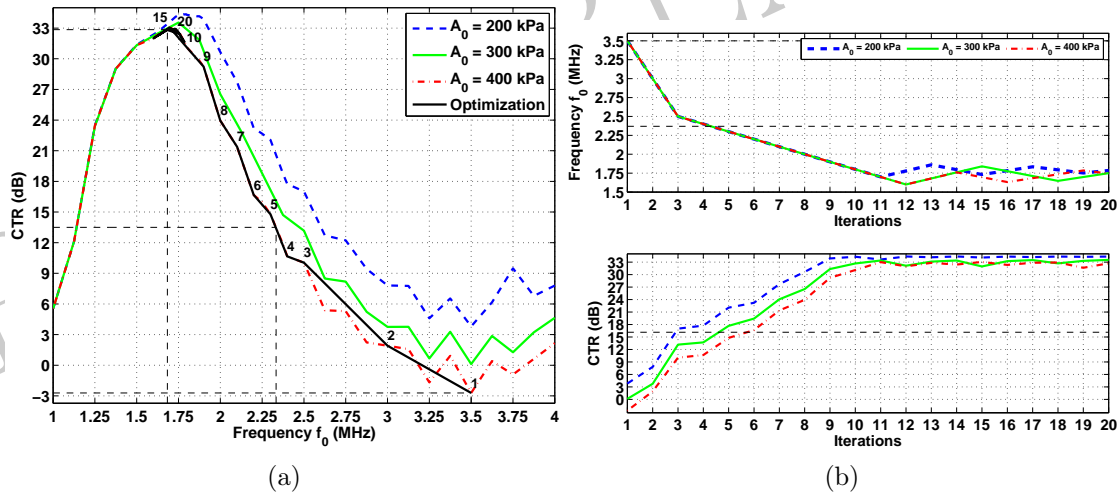


Figure 3.13 – Simulations of the optimizations using the excitation frequency f_0 in pulse inversion imaging for different pressure levels A_0 . (a) Empirical searches of the CTR maxima as a function of $f_{0,k}$. The automatic optimization path for the pressure level $A_0 = 400$ kPa is marked in black. (b) Automatic search of CTR using $f_{0,k}$ by an algorithm using the gradient.

3.2.2.1.1 Case 1 : For this first case, Fig. 3.13a shows the CTR as a function of the excitation frequency f_0 . The CTR maximum reaches 32.73 dB for an optimal frequency of 1.75 MHz if the A_0 pressure level is 400 kPa. Then, an automatic optimization by the gradient algorithm is presented in Fig. 3.13b. Fig. 3.13b at the top shows the evolution of the frequency $f_{0,k}$ as a function of the iterations k , while

3.2. OPTIMAL COMMAND BY FAMILY OF TRUNCATED HALF-SINE WAVES

Fig. 3.13b at the bottom shows the corresponding CTR . Note that the optimization for a pressure level A_0 of 400 kPa is also reported in 3.13a with a black line.

The results are close to those observed in harmonic imaging by nonlinear autoregressive filtering. However, the optimal frequencies are very different, and the corresponding CTR . The imaging method thus has a strong influence in the choice of the excitation parameters to optimize the CTR .

As previously, Fig. 3.14 shows three synthetic images for the three frequencies: the central frequency f_c of the transducer, two-thirds of the center frequency f_c of the transducer and the optimal frequency $f_{0,opt}$ for a pressure level A_0 of 400 kPa. We can make the same remarks as before, *i.e.* that the best image is that obtained for the optimal frequency $f_{0,opt}$.

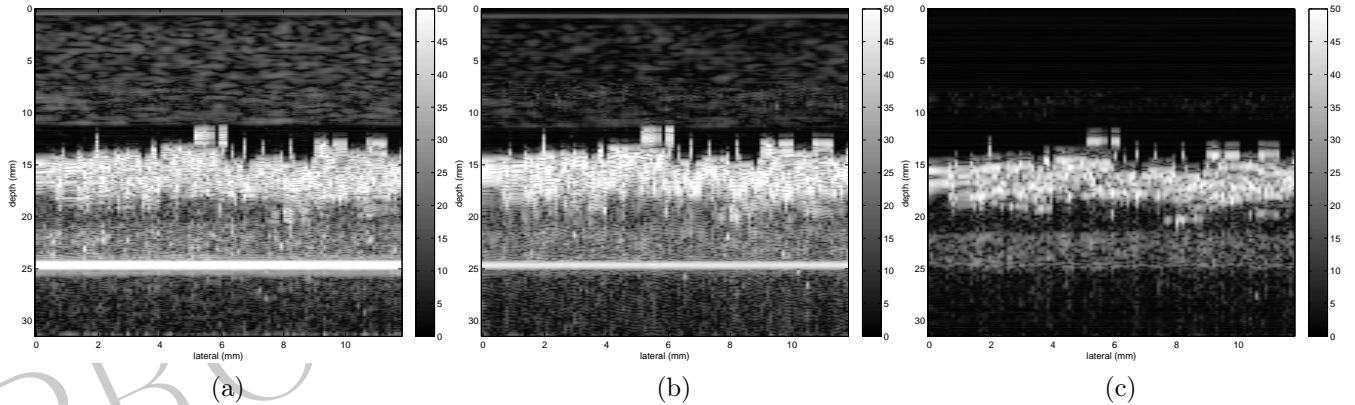


Figure 3.14 – Synthetic images in pulse inversion imaging for a pressure level of $A_0 = 400$ kPa, where the excitation frequency is (a) the central frequency f_c of transducer ($f_0 = 3.5$ MHz), (b) the two-thirds of the center frequency f_c of the transducer ($f_0 = 2.33$ MHz), (c) the optimal frequency ($f_{0,opt} = 1.77$ MHz).

Fig. 3.15 shows the experimental results which the frequency $f_{0,k}$ is plotted as a function of the iterations, and the CTR measurements corresponding. The optimization converges after about six iterations. Note that the large variations of the CTR are due to the microbubbles movement and the evolution of the insonified population.

3.2.2.1.2 Case 2 : This second case presents a new property of our method: the ability to adapt itself to the medium in order to always offer the best CTR during the examination. In order to check that our method proposes optimal and adaptive values of the excitation parameters, we carry out three simulations. In Fig. 3.16,

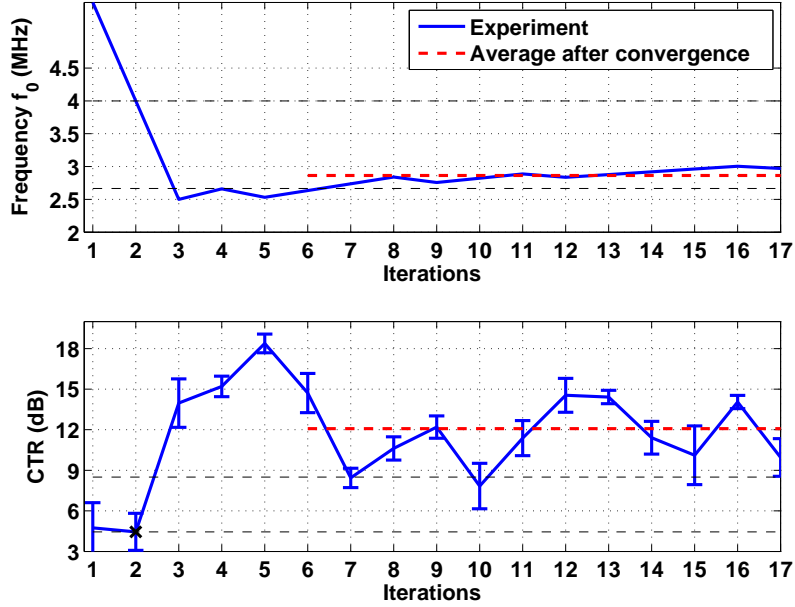


Figure 3.15 – Experiment of automatic optimization using the excitation frequency f_0 in pulse inversion imaging by a gradient algorithm.

we plotted the CTR evolution and the evolution of the excitation frequency f_0 as a function of the iterations k and when:

1. ten microbubbles of radius R_0 are present;
2. five microbubbles of radius $2R_0$ are present;
3. the microbubble number is ten with a radius R_0 up to the tenth iteration, then there are only five with a radius of $2R_0$. This choice looks like microbubble destruction. In this case, the smaller ones disappear first.

The results shown in Fig. 3.16 show that for each microbubble population, the frequency and the CTR converge to a stable value. When the microbubble population changes during the examination, the technique adapts itself without bias. We check that the radius has an impact on the optimal frequency and on the CTR , since it affects the microbubble resonance frequency. The optimal frequency is thus different for each type of microbubbles, and also for backscattered energy.

3.2.2.1.3 Case 3 : Finally for the last configuration, we want to take into account the modification of the axial resolution of the image. Indeed, when the

3.2. OPTIMAL COMMAND BY FAMILY OF TRUNCATED HALF-SINE WAVES

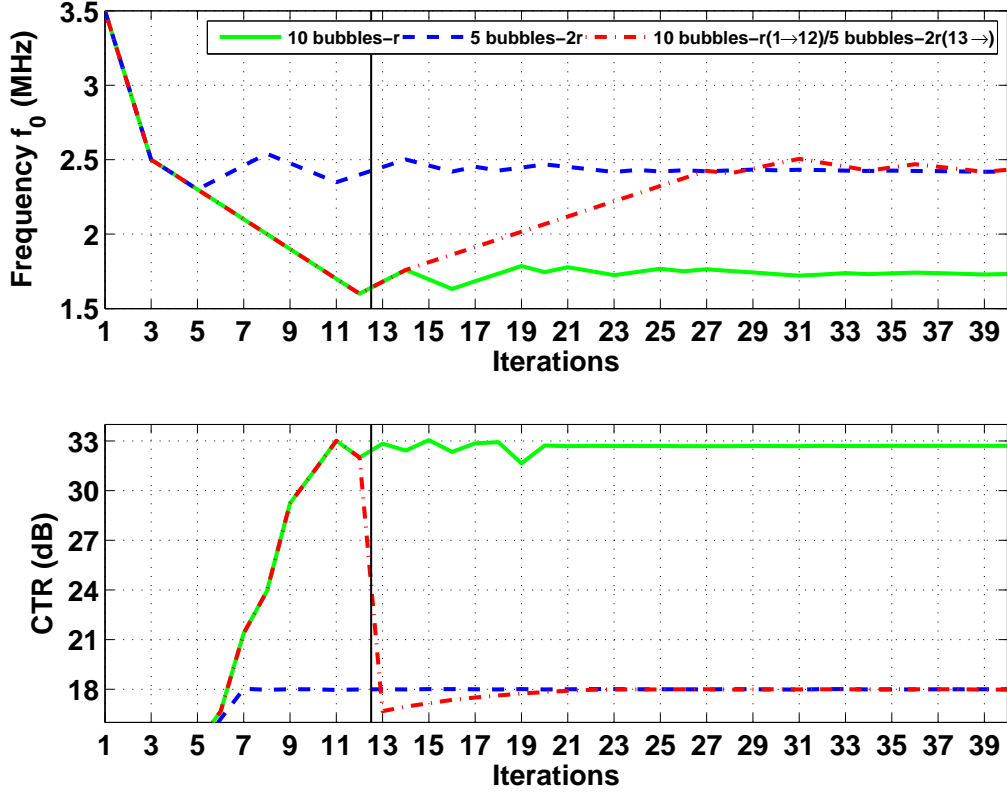


Figure 3.16 – Simulations of the CTR optimizations for a pressure level A_0 of 400 kPa in the presence of an evolution of the microbubble properties during the optimization. The first optimization is performed with ten microbubbles of radius R_0 ; the second with five microbubbles of radius $2R_0$. The third optimization starts with ten microbubbles of radius R_0 up to iteration 10 and then with five microbubbles of radius $2R_0$.

proposed frequency is lower than the central frequency f_c of the transducer, the resolution is degraded in favor of the contrast. However, we can apply a constraint that sets the resolution. For this reason, the number of cycles N_{c_k} becomes dependent on the iteration and therefore on the frequency $f_{0,k}$ so that the excitation duration is constant whatever the frequency $f_{0,k}$:

$$\frac{N_c(k)}{2f_{0,k}} = 2T_{tot}(k)^2 = cte, \quad (3.10)$$

where $2T_{tot}(k)^2$ is the time length of the excitation at the iteration k . In this case, $N_c(k)$ decreases when $f_{0,k}$ decreases.

Fig. 3.17 shows the CTR optimization by the frequency $f_{0,k}$ by applying the constraint of a constant axial resolution. Fig. 3.17a shows the empirical search of the CTR maximum as a function of the excitation frequency f_0 and the transmission

bandwidth. Fig. 3.17b shows the optimization by the gradient algorithm of the excitation frequency f_0 . Note that the CTR and the gains are less important in this configuration, since the small number of cycles N_c reduces the good separation of the harmonic components. Finally, the system converges to the maximum CTR with the same speed as in the simulation presented in Fig. 3.13b.

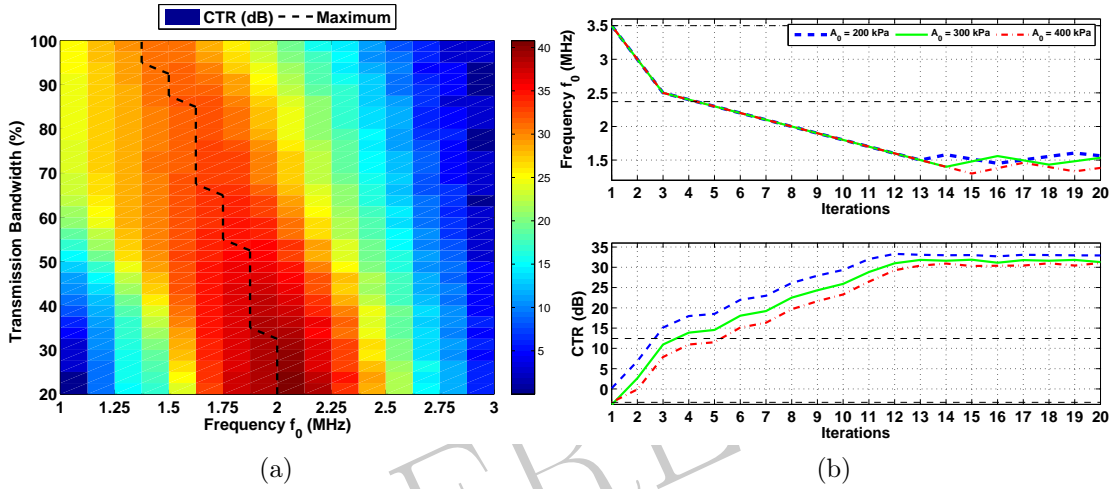


Figure 3.17 – Simulations of optimizations using the excitation frequency f_0 in pulse inversion imaging for different pressure levels A_0 and with constant axial resolution. (a) Empirical search of the CTR maxima as a function of the excitation frequency $f_{0,k}$ for different transmission bandwidths. (b) Automatic search of the CTR using the excitation frequency $f_{0,k}$ for a transmission bandwidth of 100 %, or a constant axial resolution of from 0.43 mm.

Two new synthetic images are calculated. The first is calculated when the excitation frequency is two-thirds of the center frequency f_c with an axial resolution of 0.43 mm, while the second is at the optimal frequency $f_{0,opt}$ previously obtained. Note that the image at the center frequency f_c of the transducer has already been calculated and presented in Fig. 3.14a.

We tested pulsed inversion imaging in the same way as nonlinear autoregressive harmonic imaging. The detailed results are presented in appendix B (p. 145). The corresponding CTR are presented in the table 3.3. We check that by increasing the degree of freedom, the optimized CTR can increase.

3.2.2.2 Discussions

The CTR optimization in pulse inversion imaging is carried out automatically and simply, without taking into account any *a priori* knowledge of the medium and

3.2. OPTIMAL COMMAND BY FAMILY OF TRUNCATED HALF-SINE WAVES

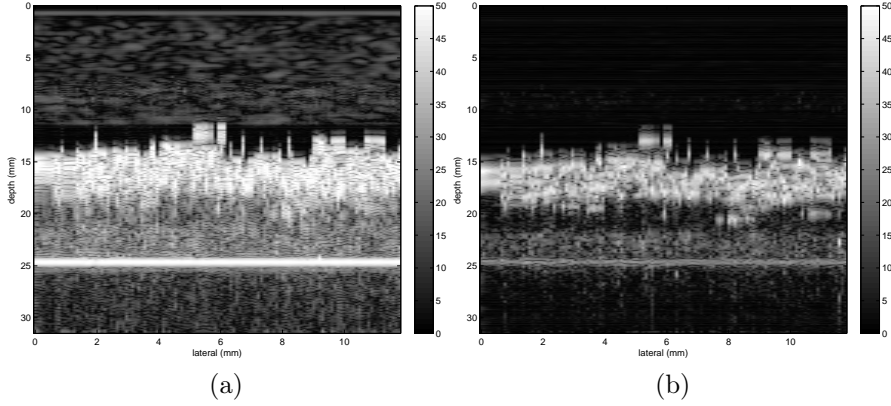


Figure 3.18 – Synthetic images in pulse inversion imaging for a pressure level of $A_0 = 400$ kPa and with a constant axial resolution of 0.43 mm, where the frequency of the excitation is (a) two thirds of the center frequency f_c of the transducer ($f_0 = 2.33$ MHz), (b) the optimal frequency ($f_{0,opt} = 1.38$ MHz).

of the transducer ^b. The performances are summarized in the table 3.3. Our method is simple for two reasons. First, optimization is performed iteratively using simple implementation algorithms. Then, the optimization is carried out only with a reduced number of parameters (maximum three). It offers a suitable choice of parameters in just a few iterations.

Optimization Parameters	f_0	f_1, f_2	α with $f_{1,opt}$ and $f_{2,opt}$	f_1, f_2 and α
<i>CTR</i> (dB)	32.73	34.32	34.36	34.84

Table 3.3 – *CTR* optimization simulations in pulse inversion imaging in different optimal settings for a A_0 of 400 kPa pressure level. The *CTR* increases with the number of optimization parameters.

The optimization is obtained by feedback. This closed loop system finds the best compromise between the transducer bandwidth and the frequency response of microbubbles and tissue. Usually, this compromise was made empirically. However, achieving this compromise requires the most accurate knowledge of the contrast medium, tissue and transducer. With our optimization algorithm, no prior knowledge is required. The algorithm adapts itself the excitation parameters, so that the energy backscattered by the microbubbles is maximized, while minimizing that backscattered by the tissue, in the transducer bandwidth. Other techniques only propose the maximization of the microbubble contribution or only the minimization

^bExcept the first three values of frequency, but their choices only affect the rate of convergence.

of the tissue contribution [Couture et al., 2008]. Our method has the advantage of realizing both simultaneously. Several remarks can be made.

First, the optimal frequency for the *CTR* is neither the center frequency f_c of the transducer nor the resonant frequency of the microbubbles.

Secondly, the contrast is realized on the harmonic components of the backscattered signal in pulse inversion imaging. It is therefore necessary to find an excitation which allows the reception of these harmonics over the greatest bandwidth.

Third, our optimization method adapts itself the frequency throughout the examination, *i.e.* by taking into account the changes in the properties of the microbubble. Experimentally, even if contrast agents are non-stationary, the optimization proposes new optimal parameters to adapt itself to the remaining microbubble population. If contrast agents does not change, the *CTR* does not change. This adaptability is also valid if the tissue or transducer varies. Note that the speed of convergence can allow us to reset the parameter μ_k of the optimization algorithm if the environment evolves a lot.

For example, our method can particularly well adjust to contrast echocardiography. In this case, our optimization with a choice of frequency resolution offers the best compromise between the *CTR* and the resolution, which privileges the *CTR* to the detriment of the resolution. In both cases of the resolution choice, an increase of the *CTR* leads to an improvement in the contrast of the image. This improvement can help the physician to propose a better diagnosis.

3.2.3 Imaging by Phase and Amplitude Modulation

This latter imaging method is also widely used. It allows us to validate definitively our concept in contrast imaging, and to observe the influence of the imaging method on the optimal parameters.

Imaging by phase and amplitude modulation was tested in the same way as other imaging methods. To avoid overloading this thesis, the detailed results are moved in appendix C (p. 151). Only the table 3.4 summarizing the results is presented below.

For this last imaging method, the parameter optimization has led us to maximize the contrast without *a priori* knowledge of the medium, the transducers and more

3.2. OPTIMAL COMMAND BY FAMILY OF TRUNCATED HALF-SINE WAVES

generally the system. The performances that are summarized in the table 3.4 confirm that the more the number of optimization parameters increases, the more the CTR increases.

Optimization Parameters	f_0	f_1, f_2	α with $f_{1,opt}$ and $f_{2,opt}$	f_1, f_2 and α
CTR (dB)	32.17	32.58	32.95	34.92

Table 3.4 – CTR optimization simulations in imaging by phase and amplitude modulation in different optimal settings for a A_0 of 400 kPa pressure level. The CTR increases with the number of optimization parameters.

3.2.4 Application to Tissue Harmonic Imaging

The latter case shows the method flexibility. We have placed ourselves in a context of native harmonic imaging, *i.e.* without microbubbles. The objective is then to maximize the harmonic energy backscattered. To do this, it is sufficient to modify only the cost function. To optimize the harmonic energy by reducing the fundamental energy, we propose to maximize the ratio $CTHF$ (“*Contrast to Tissue Harmonic and Fundamental*”) between the backscattered harmonic and the backscattered fundamental energy:

$$\max_{\mathbf{w}} (CTHF) = \max_{\mathbf{w}} \left(\frac{E_{2H}(\mathbf{w})}{E_F(\mathbf{w})} \right), \quad (3.11)$$

where E_{2H} is the harmonic energy of the backscattered signal and E_F the energy of the fundamental. We focus only on the setting of the excitation frequency f_0 with $\mathbf{w} = f_0$.

Fig. 3.19 represents the automatic optimization of the $CTHF$ ratio during the iterations k ; while at the top, the associated excitation frequency f_0 is noted during the iterations k . As for the CTR optimization, the harmonic energy in comparison with the fundamental energy is maximized in just a few iterations. The optimal frequency is again different from that usually proposed.

First, we can note that the optimization converges to different optimal frequencies as a function of the pressure level A_0 , which is not taken into account in the usual empirical choice. Then, the optimal frequency $f_{0,opt}$ does not correspond to the usual empirical choices. Moreover, the optimal choice of the transmit frequency provides better harmonic reception than the usual choice.

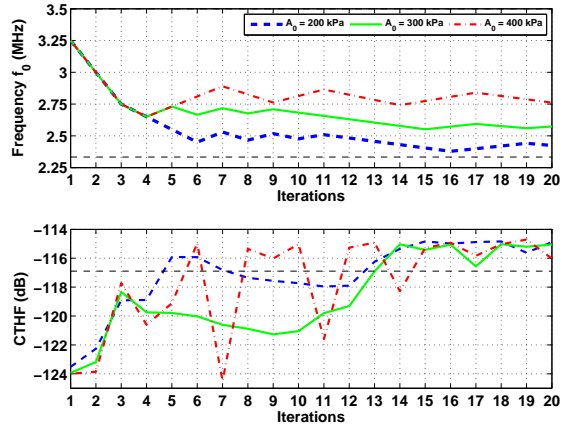


Figure 3.19 – Simulation of the optimizations using the excitation frequency f_0 in tissue harmonic imaging for different pressure levels A_0 using the excitation frequency f_k by an algorithm using the gradient.

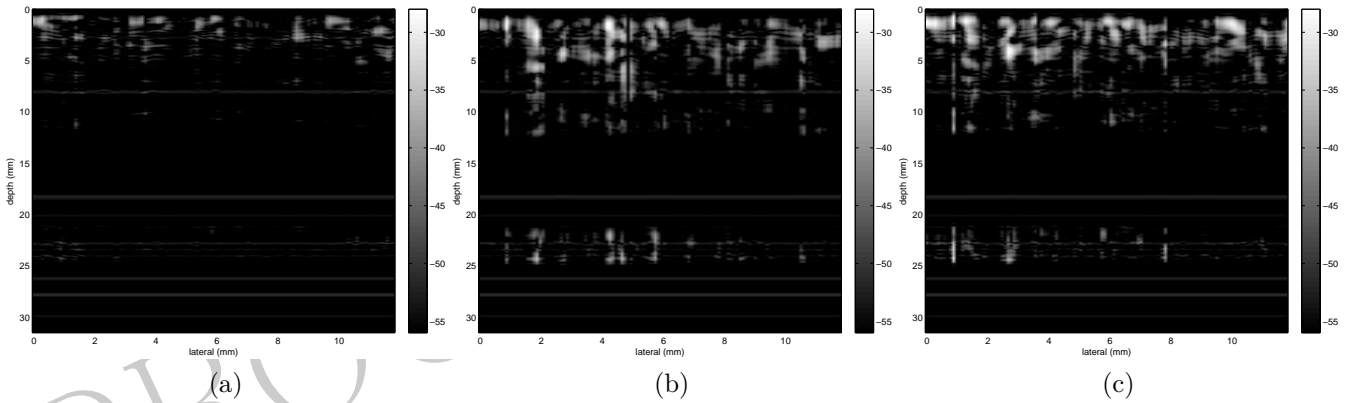


Figure 3.20 – Synthetic images in tissue harmonic imaging for a pressure level of $A_0 = 400$ kPa where the excitation frequency f_0 is (a) the center frequency f_c of the transducer ($f_c = 3.5$ MHz), (b) the two-thirds of the center frequency f_c of the transducer ($2/3f_c = 2.33$ MHz), (c) the optimal frequency ($f_{0,opt} = 2.79$ MHz).

We can observe these results on synthetic images. We compute here several cases: the first where the excitation is at the central frequency f_c of the transducer, the second at two-thirds of this frequency and the latter at the optimal frequency $f_{0,opt}$ for a pressure level A_0 of 400 kPa.

The goal was to enhance harmonic energy from the tissues. Figs. 3.20b and 3.20c show the tissue response (above the pipe) that we wanted to enhance. The image calculated with an excitation at the optimal frequency (Fig. 3.20c) makes it possible to distinguish tissue areas that were not visible in the other images.

To validate the concept, a first experiment was carried out under the same conditions as the previous simulation. Images of sixty lines have been made on

3.2. OPTIMAL COMMAND BY FAMILY OF TRUNCATED HALF-SINE WAVES

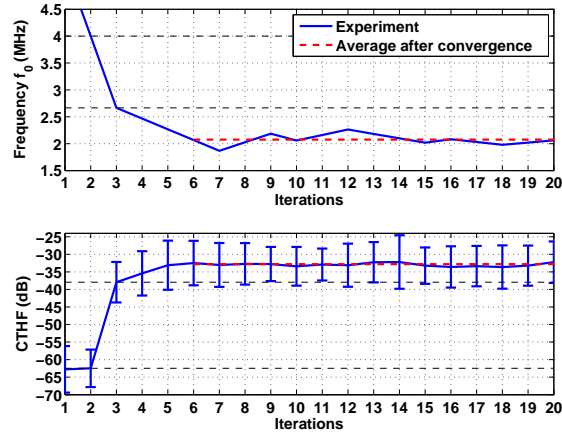


Figure 3.21 – Experiment of automatic optimization using the frequency of excitation f_0 in tissue harmonic imaging by a gradient algorithm.

a tissue phantom (Model 054GS “*General Purpose Ultrasound Phantom*”, CIRS, Norfolk, VA, USA) where a hyper-echogenic inclusion of a 8 mm-diameter is present at a depth of 4 cm. Fig. 3.21 shows the automatic optimization of the $CTHF$ ratio during the iterations k at the bottom; while at the top, the associated excitation frequency f_0 is noted during the iterations k . These results confirm those presented above. As an illustration, Fig. 3.22 shows the non-optimized images and the optimized image. The latter has a better contrast due to a lower energy of the surrounding tissue compared to the hyperechoic inclusion.

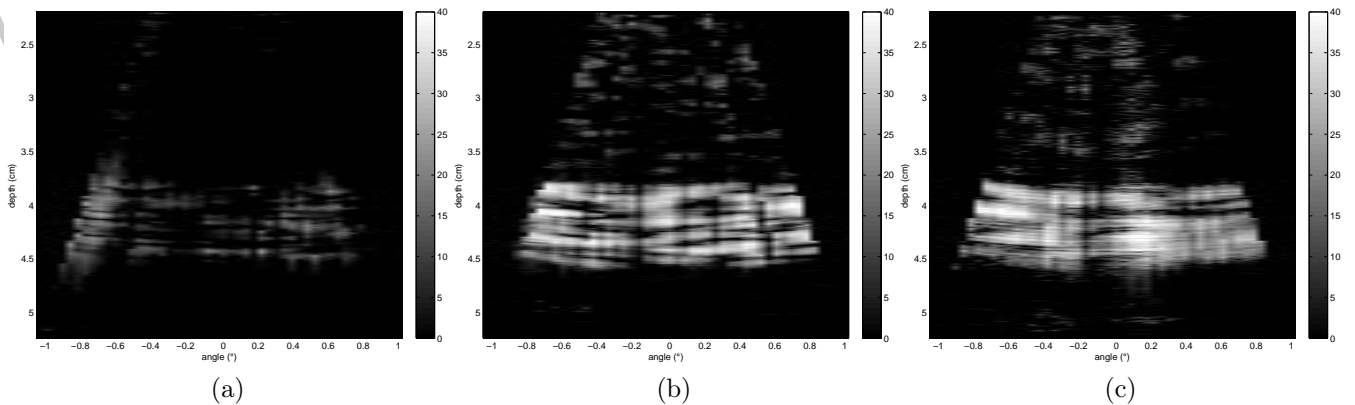


Figure 3.22 – Experimental images in tissue harmonic imaging where the excitation frequency f_0 is (a) the center frequency f_c of the transducer ($f_c = 4$ MHz), (b) the two-thirds of the center frequency f_c of the transducer ($2/3f_c = 2.67$ MHz), (c) the optimal frequency ($f_{0,opt} = 2.02$ MHz).

In a second experiment, we want to increase the number of input command parameters. To solve this problem and demonstrate the adaptation facility to

different imaging techniques, we choose to search for the pulse inversion imaging command (see page 67). The parameter number is increased to three, that is f_1 , f_2 and α . Fig. 3.23a represents the $CTHF$ as a function of the iterations k at the bottom and the parameters in the top of both figures. As an illustration, Figs. 3.23b and 3.23c show a non-optimized image and optimized image. These results confirm the correct functioning of our method for a large number of cases of ultrasound imaging.

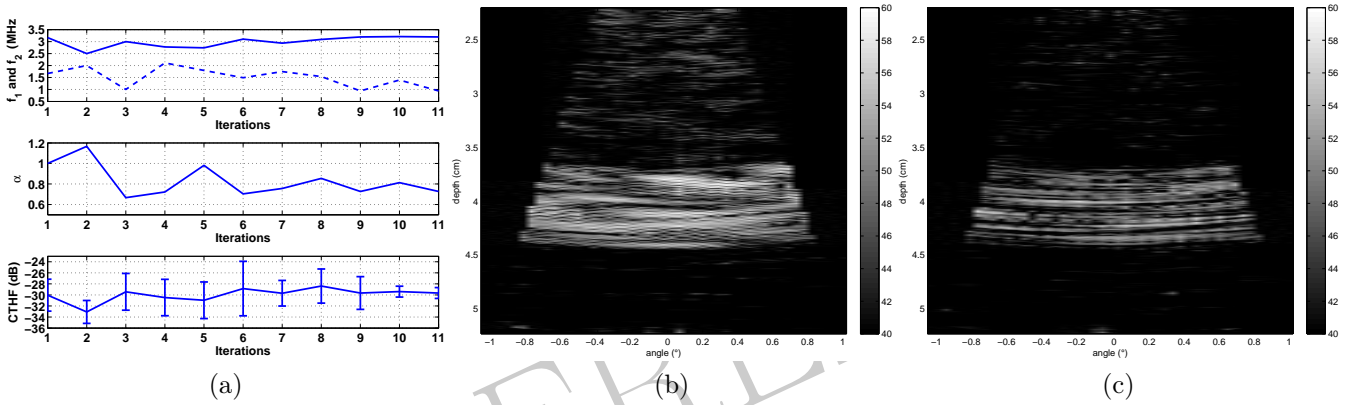


Figure 3.23 – (a) Experiment of automatic optimization using the transmit frequency f_0 by the NELDER-MEAD algorithm in tissue pulse inversion imaging by a gradient algorithm. The frequencies f_1 are written in solid lines, while the frequencies f_2 are dotted. Associated experimental images, where the frequency of excitation is (b) the two thirds of the center frequency f_c of the transducer ($f_0 = 2.67$ MHz) and (c) the optimal frequency ($f_{0,opt} = 2.02$ MHz).

3.2.5 Conclusion

Optimization of an image quality criterion can be achieved by correctly adjusting excitation parameters. This method is simple since it regulates a restricted number of parameters that describe the excitation. The usual choice determined empirically proves to provide only exceptionally the global maximum of the CTR . However, we do not advocate any adjustment values, since this role belongs to our method. It has the advantage of taking into account the specificities of the microbubbles, the tissue, the transducers and the imaging method. We have summarized in the table 3.5 the different excitation settings according to different imaging methods for a pressure level A_0 of 400 kPa. While it was common to use the same excitation parameters whatever the imaging method, our simulations and experiments show that it is important to distinguish. But it becomes very difficult to determine this

3.2. OPTIMAL COMMAND BY FAMILY OF TRUNCATED HALF-SINE WAVES

choice empirically by taking into account as much information as possible. Our method proposes to free from all the *a priori* information inaccessible in practice to determine the maximum of the cost function (here *CTR* or *CTHF*). Moreover, although some parameters did not make a significant gain, other imaging methods might have a different behavior. For example, recent studies show that the compression phase is the most important phase for a microbubble to generate sub-harmonics [de Jong et al., 2007]. In this case, the α ratio could be important.

Optimization Parameters	HI-NAR	PI	CPS
f_0 (MHz)	2.28	1.75	1.69
f_1 (MHz)	2.89	1.86	1.73
f_2 (MHz)	2.26	1.67	1.69
α with $f_{1,opt}$ and $f_{2,opt}$	0.72	0.99	0.93
f_1	3.22	1.4	1.31
f_2	1.99	2.23	2.15
α	0.52	0.4	0.45

Table 3.5 – Optimal parameters of the simulations according to the different optimizations for a pressure level A_0 of 400 kPa (HI-NAR: harmonic imaging by nonlinear autoregressive filtering, PI: pulse inversion imaging, CPS: imaging by phase and amplitude modulation).

Moreover, our method is adaptive. It can adapt itself to changes in the medium to be imaged, such as the evolution of the microbubble population or the sensor aging.

We did not wish to compare the performances between the different techniques. The results between the different techniques are difficult to compare since many criteria in the image change. Thus harmonic imaging by nonlinear autoregressive filtering offers a better contrast, but it is to the detriment of the resolution that other techniques can propose.

Finally, our method can also be applied to all ultrasound imaging techniques and not only to contrast imaging. It is sufficient to find a cost function adapted to the criteria we wish to optimize. This could be, for example, a criterion on resolution. We have shown by our simulations that this adaptation is possible.

3.3 Optimal Command by Family of Sine Waves Modulated in Frequency

The second family consists of sine waves modulated in frequency. Analytical models of microbubbles have shown that the parameter choice for the modulation law is important in order to find the optimal microbubble backscattering [Barlow et al., 2011]. However, this work uses only a linear law. A study in tissue harmonic imaging has shown its interest in the search for a nonlinear modulation law [Song et al., 2011]. We propose to look for the law parameters. We make the choice of a polynomial law such as:

$$f_k(t) = f_{0,k} + \beta_{1,k}t + \beta_{2,k}t^2 + \beta_{3,k}t^3 \quad (3.12)$$

The signal is a sine wave modulated in frequency whose envelope is Gaussian [Wilhjelm, 1993] such as:

$$x_{k,\varphi}(t) = A \cdot \exp \left[-2 \left(\frac{\varpi(tp - t_0)}{t_m} \right)^2 \right] \sin \left(2\pi (f_{0,k} + \beta_{1,k}t + \beta_{2,k}t^2 + \beta_{3,k}t^3) t + \phi_\varphi \right), \quad (3.13)$$

where $t_m = 5.7 \mu\text{s}$ and $\varpi = 3$. Note that for compression step, the filter $c(t)$ is written:

$$c_{k,\varphi}(t) = A \cdot \exp \left[-2 \left(\frac{\alpha(tp - t_0)}{t_m} \right)^2 \right] \sin \left(4\pi (f_{0,k} - \beta_{1,k}t - \beta_{2,k}t^2 - \beta_{3,k}t^3) t + \phi_\varphi \right). \quad (3.14)$$

	CHI	CPI
Backscattered Energy (dB)	-36.2	-31.6
f_0 (MHz)	3.6	2.9
β_1 (THz/s)	37.5	-1.6

Table 3.6 – Simulations of the global maxima of the backscattered energy by a non-encapsulated microbubble with a $2.5 \mu\text{m}$ -radius when the excitation is a chirp and associated parameters of the modulation law (CHI: harmonic imaging by chirp; CPI: imaging of chirp inversion).

In a preliminary study, we looked for the parameters of the modulation law $f(t) = f_0 + \beta_1 t$ which maximize the energy backscattered by a non-encapsulated microbubble of $2.5 \mu\text{m}$ radius without taking into account the propagation. The energy transmitted to the microbubble is normalized in such a way that it is constant. We have observed that the imaging by chirp inversion obtained better performances

3.3. OPTIMAL COMMAND BY FAMILY OF SINE WAVES MODULATED IN FREQUENCY

in terms of harmonic energy backscattered by microbubbles than harmonic imaging by chirp (table 3.6).

We have therefore chosen to use imaging of chirp inversion.

Moreover, we have shown that increasing the polynomial order can increase the energy backscattered by the microbubble (table 3.7). These promising results led us

Polynomial order of the modulation law	1	2
Backscattered maximum energy (dB)	-31.6	-29.2

Table 3.7 – Simulations of the global maxima of the backscattered energy by a non-encapsulated microbubble with a 2.5 μm -radius when the excitation is a chirp and associated parameters of the modulation law (CHI: harmonic imaging by chirp; CPI: imaging of chirp inversion).

to test this method with a more sophisticated cost function: the *CTR*.

We distinguish several possible optimizations. In a first step, we consider a linear modulation law. Then we complicate this law by increasing the polynomial order from two to three.

3.3.1 Setting of a Linear Modulation Law

This first case considers a linear modulation law such as:

$$f_k(t) = f_{0,k} + \beta_{1,k}t \quad (3.15)$$

Fig. 3.24 presents the optimization of f_0 and β_1 . Fig. 3.24a shows the empirical optimization of *CTR* as a function of f_0 and β_1 , while Fig. 3.24b presents the automatic optimization by the NELDER-MEAD algorithm. *CTR*, β_1 and f_0 are as a function of the iterations k , respectively at the bottom, the middle and the top. Note that the automatic optimization is plotted by a white line on Fig. 3.24a.

These results show that the *CTR* has a maximum when the signal is modulated ($\beta_1 \neq 0$) and can be retrieved automatically in a few iterations k .

3.3.2 Setting of a Quadratic Modulation Law

This second case considers a quadratic term supplementary to the first law such as:

$$f_k(t) = f_{0,k} + \beta_{1,k}t + \beta_{2,k}t^2 \quad (3.16)$$

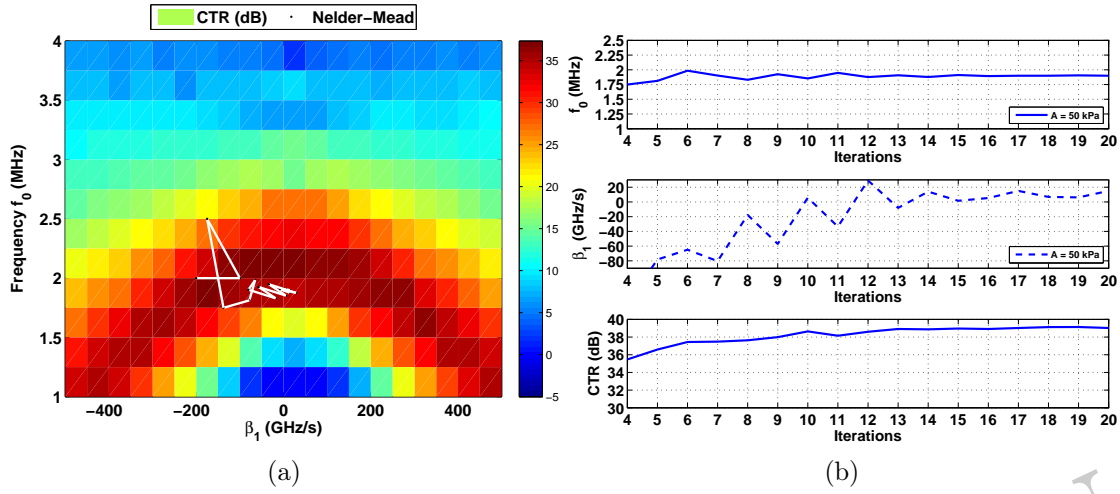


Figure 3.24 – Simulations of the optimization of linear modulation law in imaging by chirp inversion for a pressure level A_0 of 50 kPa. (a) Empirical search of the CTR maximum as a function of f_0 and β_1 . The automatic optimization path is written in black. (b) Automatically search for CTR using f_0 and β_1 with the NELDER-MEAD algorithm.

Fig. 3.25 shows the optimization of f_0 , β_1 and β_2 . Fig. 3.25a represents the empirical optimization of CTR as a function of β_1 and β_2 where f_0 is set to the optimal value during the optimization of linear law. Fig. 3.25 presents the automatic optimization of the CTR as a function of the iterations k , β_1 and β_2 (middle) and f_0 (top).

These results show first that the CTR has a maximum when the law has a non-zero quadratic term ($\beta_2 \neq 0$). However, the gain with respect to the linear law is low, probably because of the restricted bandwidth of the transducers. Moreover, the empirical optimization reveals the presence of several local maxima. The automatic search can find the global maximum only if the algorithm initialization is correctly chosen.

3.3.3 Setting of a Cubic Modulation Law

This third and last case adds a cubic term to the law as defined by the equation 3.12. Fig. 3.26 shows the automatic optimization where the CTR (bottom) is as a function of the iterations k , β_2 and β_3 (middle), finally f_0 and β_1 (top).

These results show first that the CTR has a maximum when the law has a non-zero cubic term ($\beta_3 \neq 0$). However, the gain with respect to the quadratic law is small, probably because of the restricted bandwidth of the transducers.

3.3. OPTIMAL COMMAND BY FAMILY OF SINE WAVES MODULATED IN FREQUENCY

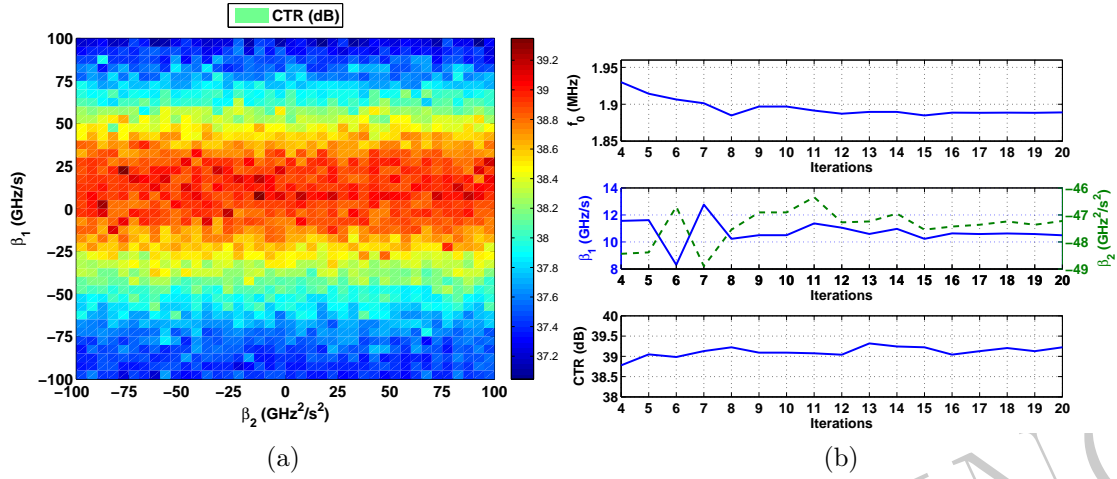


Figure 3.25 – Simulations of the optimization of the quadratic modulation law in imaging by chirp inversion for a pressure level A_0 of 50 kPa. (a) Empirical search of the CTR maximum as a function of f_0 , β_1 and β_2 . The automatic optimization path is written in black. (b) Automatically search for CTR using f_0 , β_1 and β_2 by the Nelder-Mead algorithm.

3.3.4 Discussions

The optimization with this second signal family shows that it is possible to optimize a cost function such as CTR by different signal families. This choice is made on the basis of *a priori* knowledge. However once done, no further information is needed to reach the maximum.

Law	Linear	Quadratic	Cubic
CTR (dB)	39	39.2	39.3
f_0 (MHz/s)	1.89	1.88	1.91
β_1 (GHz/s)	14.95	10.5	10.3
β_2 (GHz ² /s ²)	-	-47.2	-47
β_3 (GHz ³ /s ³)	-	-	-16.8

Table 3.8 – Optimal simulation parameters according to the different optimizations for a pressure level A_0 of 400 kPa in imaging by chirp inversion.

The choice of the modulation law makes it possible to improve the performances. We stopped at order three. However, the order increase always allowed to reach a greater maximum when the order was greater (table 3.8). Moreover, the parameter values do not change much with the order increase. This observation could allow to make a first optimization of f_0 and β_1 , followed by optimizations of a single parameter until the desired order.

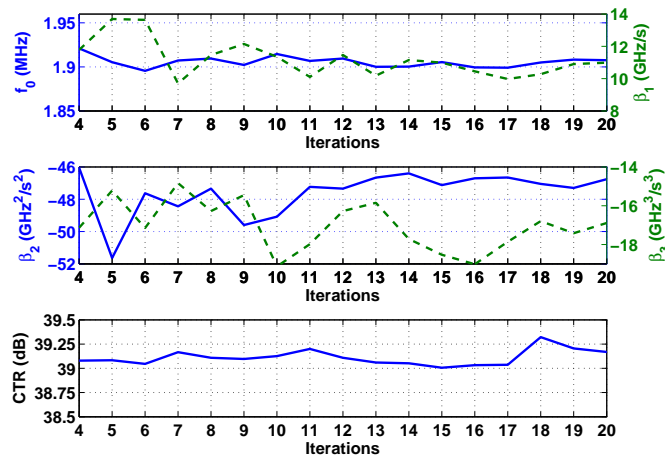


Figure 3.26 – Simulation of the automatic optimization of the cubic modulation law in imaging by chirp inversion for a pressure level A_0 of 50 kPa using f_0 , β_1 , β_2 and β_3 by the Nelder-Mead algorithm.

However, note that the CTR optimization is not as important as the empirical search for backscattered energy for the non-encapsulated microbubble could show. This can be explained, on the one hand, by the fact that the CTR takes into account the tissue behaviour and, on the other hand, because the microbubble properties tested were not the same. The parameters optimization of a polynomial law is therefore highly dependent on the contrast product used. The advantage of our method is to always offering the maximum of CTR .

Chapter 4

Optimal Command of Transmitted Waveform

IN the previous chapter, we have imposed a suboptimal waveform determined from a family of parametrized signals. The disadvantage of this technique is to order the prior knowledge of *a priori* information to choose the signal family. But its advantage is to simplify the evaluation of parameters. We therefore investigate a new technique that avoids any *a priori* knowledge. Moreover, the method must provide performance at least similar to an optimization per family of signals.

We will therefore begin by explaining the principle of our method. To understand its operation, we will write about the problem of optimal command in the case where the medium is linear. Finally, we will optimize the contrast in the same condition as for the previous chapter.

4.1 Method

The principle of the optimal command of transmitted waveform follows the diagram 4.1. The idea consists in exciting a filter, of the non-linear autoregressive kind with variable parameters, by any signal (sinus wave or random). Here, the excitation signal serves to *a priori* and simply send energy into the system to be studied. The filter parameters which guarantee the maximum criterion are then optimized iteratively. The signal thus created converges towards an optimal solution.

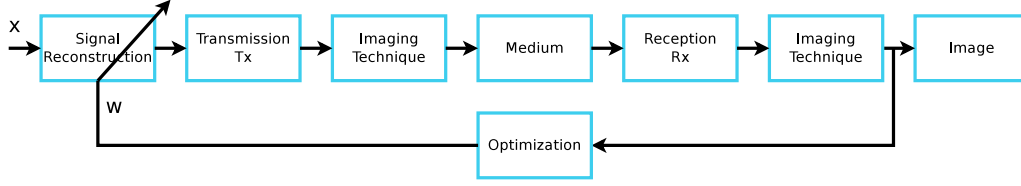


Figure 4.1 – Block diagram of optimal command of transmitted waveform for a linear medium with sinus wave excitation.

The optimization parameters are the \mathbf{w} parameters of a nonlinear autoregressive filter described by the following equation:

$$\hat{x}_k(t) = \mathbf{x}_t^T \mathbf{w}_k, \quad (4.1)$$

where T is the symbol of the transpose and

$$\mathbf{x}_t = [x_{t-1}, x_{t-2}, \dots, x_{t-M+1}, x_{t-1}^2, x_{t-1}x_{t-2}, \dots, x_{t-M+1}^2, x_{t-1}^3, x_{t-1}^2x_{t-2}, \dots, x_{t-M+1}^3]^T,$$

$$\mathbf{w} = [w_1(1), w_1(2), \dots, w_{M+1}, w_2(1, 1), w_2(1, 2), \dots, w_2(M-1, M-1), w_3(1, 1, 1), w_3(1, 1, 2), \dots, w_3(M-1, M-1, M-1)]^T.$$

The memory M of the filter is chosen to be three, so as to reduce the number of parameters to nineteen.

This signal constitutes the system excitation where the parameters are searched using the NELDER-MEAD algorithm.

4.2 Optimal Command of Waveform for a Linear Medium

In order to understand the principle of our method, we first optimize the backscattered energy E_{bubble} of a system in linear operation:

$$\max_{\mathbf{w}} (E_{bubble}). \quad (4.2)$$

We use the microbubble model without propagation with a low pressure level. The signal $x(t)$ is chosen as the reference signal described by the equation 3.8 at the central frequency of the transducer, *i.e.* a sine wave signal apodized by a Gaussian

4.2. OPTIMAL COMMAND OF WAVEFORM FOR A LINEAR MEDIUM

function. At the first iteration, the filter parameters are initialized and the signal $x(t)$ is transmitted to the studied medium. Then, from the signal backscattered by the microbubble and the chosen cost function, the optimization process of the parameters is activated. At the second iteration, the signal $x(t)$ is modified by a filter composed of new parameters. The optimization process is then repeated until a solution is converged.

Fig. 4.2 represents the optimized command when the process has converged. The waveform of this signal corresponds, as expected, to the signal backscattered by the microbubble returned temporally. We also decomposed the backscattered signal into a linear and quadratic component using a nonlinear autoregressive filter. We compare the decomposition of the input signal with the output signal.

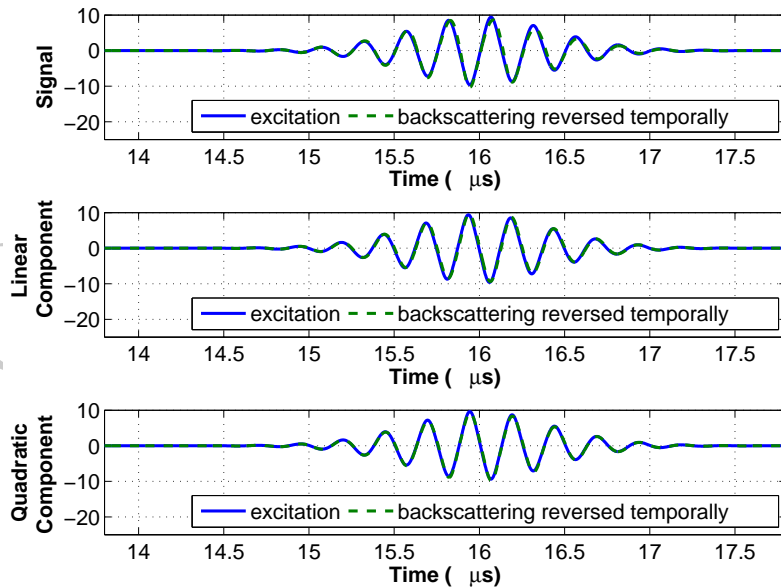


Figure 4.2 – Comparison between the excitation after optimization and the backscattered signal for a linear system (at the top the excitation signal and the backscattered signal, in the middle their linear components of a nonlinear autoregressive filter; their quadratic components of a nonlinear autoregressive filter). The ordinate axis corresponds to normalized pressure values.

The results in Fig. 4.2 show that the optimal command proposes an excitation which corresponds to the time reversal of the backscattered signal. Each component of the excitation is also the time reversal components of the backscattered signal. This result confirms the well-known results of matched filtering (or time reversal).

4.3 Optimal Command of Waveform for a Nonlinear Medium

Before to apply the method to full imaging systems, we continue our analysis.

4.3.1 Optimal Command of Backscattering

We replace the linear system with a nonlinear system. This system is always composed of a microbubble, without taking into account the propagation. However, the incident pressure level exciting the microbubble is much higher.

Fig. 4.3 represents the same signals as the figure ref fig: part2: chap3: fig2, but considering this non-linear system.

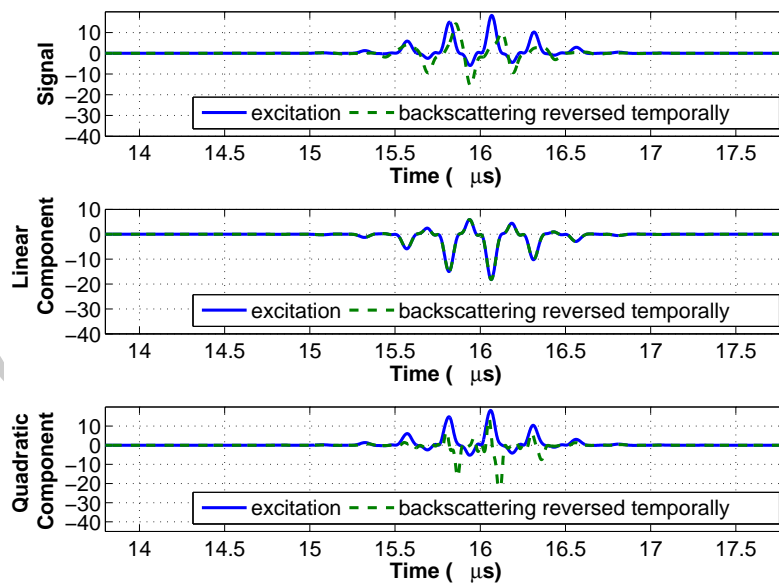


Figure 4.3 – Comparison between the excitation after optimization and the backscattered signal for a nonlinear system (at the top the excitation signal and the backscattered signal, in the middle their linear components of a nonlinear autoregressive filter; their quadratic components of a nonlinear autoregressive filter). The ordinate axis corresponds to normalized pressure values.

The results show that it is much more difficult to interpret them when the system is nonlinear. The linear component of the decomposition shows us that the excitation signal is exactly the opposite of the backscattering linear component. If we compare it with the time reversal, our method tries to take into account the nonlinearities. While the temporal reversal considers only a simple convolution described by the

4.3. OPTIMAL COMMAND OF WAVEFORM FOR A NONLINEAR MEDIUM

equation 1.1, our method extends this concept by a decomposition such as:

$$y(t) = \sum_{i=1}^M w_1(i)x(t-i) + \sum_{i=1}^M \sum_{j=i}^M w_2(i,j)x(t-i)x(t-j) + \dots \quad (4.3)$$

Finally, our adaptive approach indicates that the optimal signal does not correspond to the higher order signals returned. This concept is checked for the first order, but not for higher orders. One way to detect the nonlinearity degree could be to quantify the temporal non-reversal criterion of higher orders.

4.3.2 Optimal Command of Waveform in Imaging by Pulse Inversion

We now place ourselves in a context of harmonic contrast imaging where the cost function to be optimized is the *CTR*. The principle is described by the diagram 4.4. To avoid the choice of the signal $x(t)$, we propose to excite the system by a noise. The simulation model that we use is a simplified model which does not take propagation into account and which assimilates the tissue behaviour to fat scatterers. This last choice was made to have a reference.

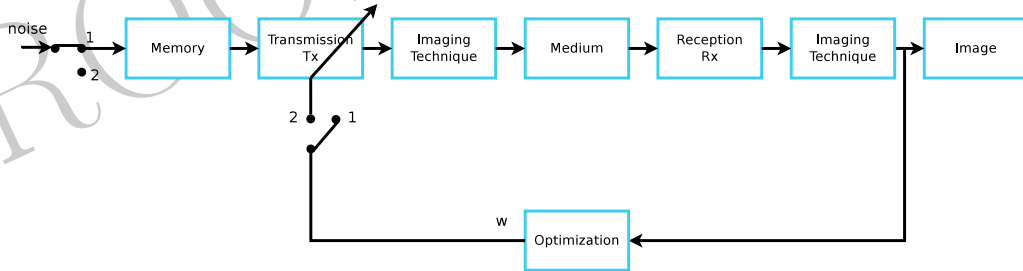


Figure 4.4 – Block diagram of optimal waveform in imaging by pulse inversion.

We repeat this operation ten thousand times to note the *CTR* values obtained without optimization. Fig. 4.5 shows the histogram of the *CTR* measurements when the excitation is a noise. If the *CTR* distribution is approximated by a Gaussian distribution of mean 26.7 dB and variance 2 dB². Note that when the excitation is a sine wave modulated by a Gaussian at the optimal frequency $f_{0,opt}$ of 2.5 MHz, the *CTR* reaches its maximum 30.44 dB (for sine wave excitation). When the system input is a sine wave excitation at the center frequency f_c of the transducer (ie 3.5 MHz) then the *CTR* reaches 26.18 dB.

From the histogram, we deduce by the MONTE-CARLO methodindexMethod!Monte-Carlo that it is necessary to test a hundred noises to find at least one which gives a CTR greater than or equal to the maximum CTR obtained by sine wave excitation (switches in position 1). This optimal “noise” constitutes the signal $x(t)$.

From this “optimal” noise, the optimization of the parameters \mathbf{w} is done in a closed loop by the NELDER-MEAD algorithm to maximize the CTR (switches in position 2). Fig. 4.6 shows this optimization where we have noted the CTR and the parameters \mathbf{w} as a function of the iterations k .

The CTR reaches a maximum of 31.25 dB. This maximum is higher than the CTR obtained with noise only (30.47 dB) , than the CTR obtained when the sine wave excitation is at the optimal frequency $f_{0,opt}$, and than the CTR obtained when the sine wave excitation is at the center frequency f_c of the transducer. The transducer filters noise around the frequency f_c of 3.5 MHz. While a sine wave excitation of frequency f_c can only get a CTR of 26.4 dB, our method can improve the CTR by 4.85 dB. Note that from all the noises (about hundred) that maximize a CTR greater than 30.47 dB, we have not yet found common temporal or frequency factors. This work is ongoing.

4.3.3 Conclusion

Our technique makes it possible to free oneself from the signal family choice. It is then possible to find a suboptimal filtered random excitation which maximizes the CTR without any *a priori* knowledge available with difficulty. Note however that it is necessary to test a hundred random signals to find one that greatly optimizes the CTR , *i.e.* one hundred for ten thousand tested signals. We hope to reduce this number significantly by identifying features common to the different noises that maximized the CTR .

4.3. OPTIMAL COMMAND OF WAVEFORM FOR A NONLINEAR MEDIUM

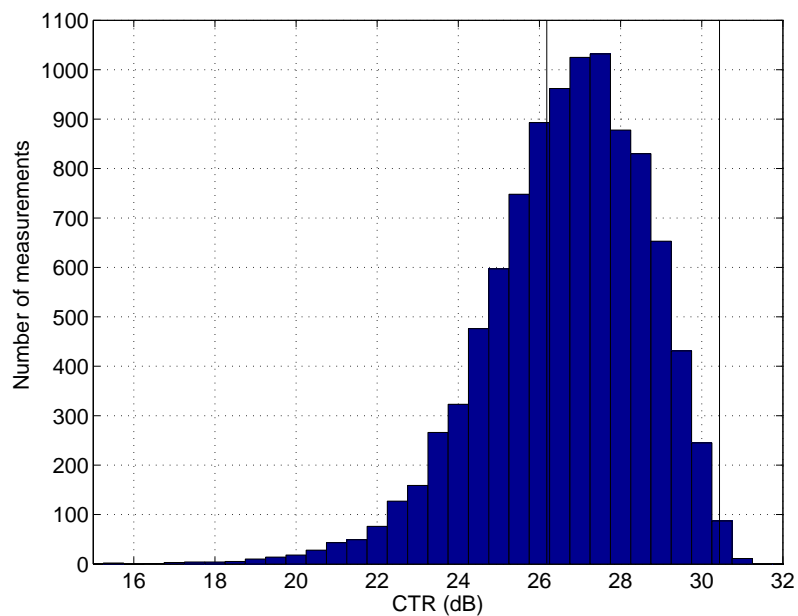


Figure 4.5 – Histogram of the *CTR* measurements when the excitation is a noise.

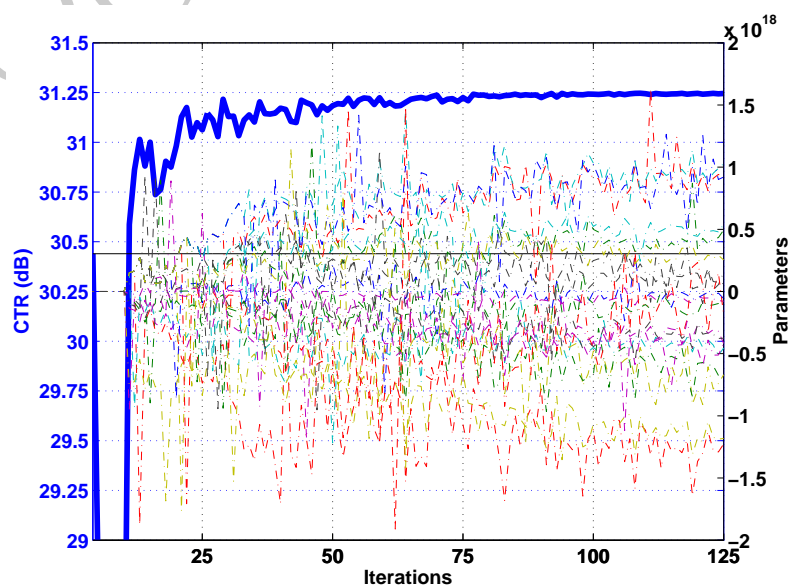


Figure 4.6 – Optimization of the *CTR* by the search for parameters w that describe the the excitation waveform.

PROOFREADING

—PART III—

OPTIMAL COMMAND OF THE
TRANSDUCER RESPONSE

PROOFREADING

Chapter 5

Optimal Command of a Capacitive Micromachined Ultrasound Transducers

FOR about twenty years, alternatives to piezoelectricity in transduction have appeared. One of the most promising technologies is the micro-machined capacitive Micromachined Ultrasound Transducers, known as cMUT [Haller and Khuri-Yakub, 1996, S n gond, 2010]. These devices belong to the family of microsystems and more particularly to the MEMS for *Micro Electro Mechanical Systems*. They are made from microelectronic processes.

The cMUT consists of several hundred (or even thousands) of partially metallized micromembranes (a few tens of micrometers in diameter) suspended above vacuum cavities (Fig. 5.1).

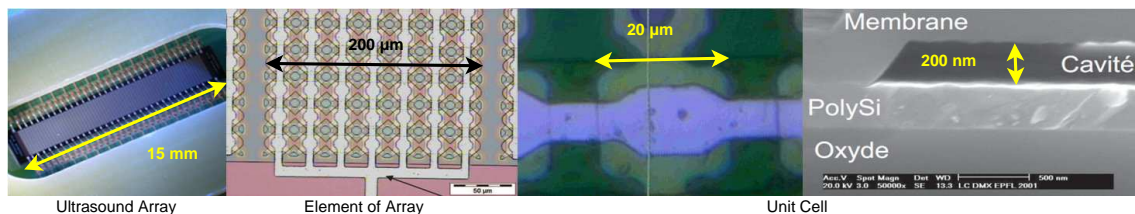


Figure 5.1 – Structure of a cMUT at different scales.

In transmission, the application of an alternating voltage produces an electrostatic force generating the membrane displacement. The whole membranes then produces an ultrasound wave propagating on the front face of the sensor. On the other hand, in reception, when an ultrasound wave arrives at the front face of the

sensor, the echo sets in motion the membranes which produce a variation in charges at the sensor terminals when a bias voltage is applied to it.

The innovative potentials of these sensors in relation to conventional piezoelectric technologies are numerous: reliability, mass production, miniaturization and electronics integration. In addition to manufacturing advantages, cMUTs have wider bandwidths than piezoelectric transducers.

One of the main cMUT difficulties is that the electrostatic force is proportional to the square of the tension and to the square of the membrane displacement. The cMUT has a highly nonlinear behaviour, which results in the appearance of harmonics in the generated ultrasound wave. Harmonic imaging is thus compromised. In this chapter, we try to reduce the nonlinearity in the displacement of a single cell in the context of harmonic imaging by optimal command (Fig. 5.2).

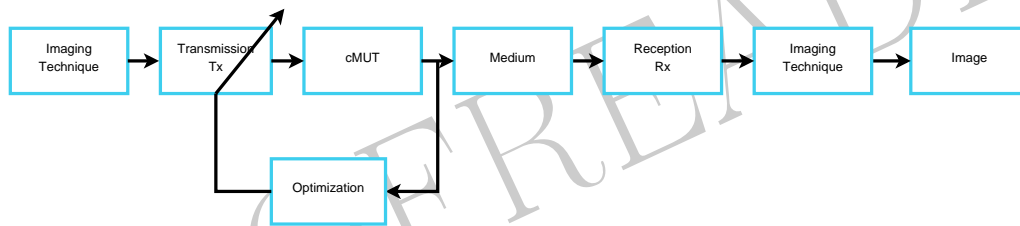


Figure 5.2 – Block diagram of the optimal command for cMUT in the context of harmonic imaging.

Some methods [Zhou et al., 2004, Novell et al., 2009] have been proposed to reduce the second harmonic at the cMUT output. Both methods consist in sending the sum of two sinusoids of different frequencies whose amplitudes and phases are correctly chosen. The first method excites the cMUT with two components at f_0 and $2f_0$, while for the second method the two components are at f_0 and $3f_0$. The second harmonic at the cMUT output is reduced for a choice of amplitudes and phase of the signal determined empirically. The empirical determination of the transmitted signal parameters is a major handicap when it is necessary to transmit coded signals (in phase or in frequency) more complicated than simple sinusoids. To eventually replace the piezoelectric transducers with cMUT transducers, it is necessary to offer the various imaging systems manufacturers the whole range of existing encodings, whether in tissue imaging or in contrast imaging. Today, this is not the case since the compensation of the cMUT nonlinearities is carried out empirically. The challenge we want to address here is to be able to propose excitations capable of compensating

for undesirable effects for existing coding techniques. To achieve this objective, we must compensate automatically and adaptively the excitation, *i.e.* the command.

In this chapter, we will propose a method that looks for the optimal command for the cMUT, so that the output reaches a target signal. We have developed two approaches: a recursive method and an iterative method. We will begin by describing the cMUT, then our different methods. Finally we present our simulation results that we will discuss.

5.1 Material: Simulation of a cMUT

One of the models developed in the laboratory by Nicolas SÉNÉGOND and Dominique CERTON [Sénégon, 2010] consists of an approximation of the cell by a damped mass-spring system having the characteristics of a plane capacitor with variable inter-electrode space (Fig. 5.3) [Lohfink and Eccardt, 2005].

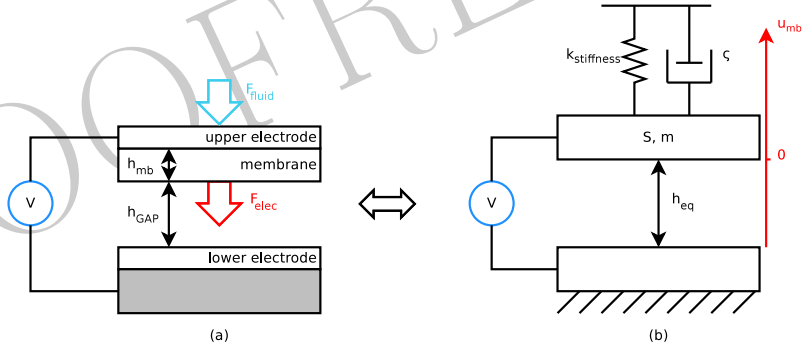


Figure 5.3 – First-order equivalent scheme of a capacitive transducer.

In order to avoid short circuits, the upper electrode is deposited on the silicon nitride membrane (SiN) whose relative electrical permittivity is ε_{mb} . The equivalent height of the capacitor is described by the following equation:

$$h_{eq} = h_{GAP} + \frac{h_{mb}}{\varepsilon_{mb}}. \quad (5.1)$$

The membrane displacement is translated from the fundamental principle of dynamics:

$$m_{mb}u_{mb}'' = F_{elec} + F_{fluid} - 2\zeta u_{mb}' - k_{stiffness}(u_{mb} - h_{eq}). \quad (5.2)$$

where the electrostatic force F_{elec} is proportional to the square of the voltage and to the square of the membrane displacement u_{mb} such as:

$$F_{elec} = -\frac{1}{2} \frac{\varepsilon_0 S V^2}{2u_{mb}^2}. \quad (5.3)$$

The fluid force is derived from the radiation on itself of a rigid baffle piston in a semi-infinite space by the RAYLEIGH integral [Stepanishen, 1978, Lingvall, 2004]. This equation is solved temporally by the RUNGE-KUTTA method with the following parameters to have a realistic membrane behaviour:

$$\left\{ \begin{array}{l} h_{GAP} = 200 \text{ nm} \\ h_{mb} = 400 \text{ nm} \\ \varepsilon_0 = 8.85 \cdot 10^{-12} \text{ F} \cdot \text{m}^{-1} \\ \varepsilon_{mb} = 7.5 \\ S = 10^{-10} \text{ m}^2 \end{array} \right. \quad \text{et} \quad \left\{ \begin{array}{l} m_{mb} = 15 \cdot 10^{-13} \text{ kg} \\ k_{stiffness} = 1900 \text{ N} \cdot \text{m}^{-1} \\ \zeta = 7 \cdot 10^{-9} \end{array} \right.$$

Measured parameters Estimated parameters

For these operating parameters, the theoretical resonance frequency of the membrane is identified at 5.6 MHz.

Although this model can reveal more the average cell behaviour, it can present the nonlinear cMUT characteristics as well as the collapse phenomenon. The collapse consists of the membrane collapse on the cavity bottom due to an unstable equilibrium between the stiffness forces of the membrane and the electrostatic force.

Given that the electrostatic force F_{elec} is proportional to the squared electrical voltage, a DC bias voltage is added to the voltage at the cMUT terminals. This continuous voltage thus makes it possible to limit the system nonlinearities. We chose a polarization voltage at 65% of the collapse voltage to offer the best compromise between the membrane displacement u_{mb} and the harmonics generated [S en egond, 2010, p. 164].

This study is in the context of harmonic imaging. Given the bandwidth in reception, an excitation whose frequency is less than the central frequency f_c of the transducer and therefore less than the cMUT resonance frequency f_{res} is usually used. In this framework, two cMUT behaviours have been identified: a forced regime where the excitation frequency is much lower than the cMUT resonance frequency

5.2. METHODS

f_{res} and a so-called intermediate regime at the half cMUT resonance frequency f_{res} . These behaviours are summarized in Fig. 5.4.

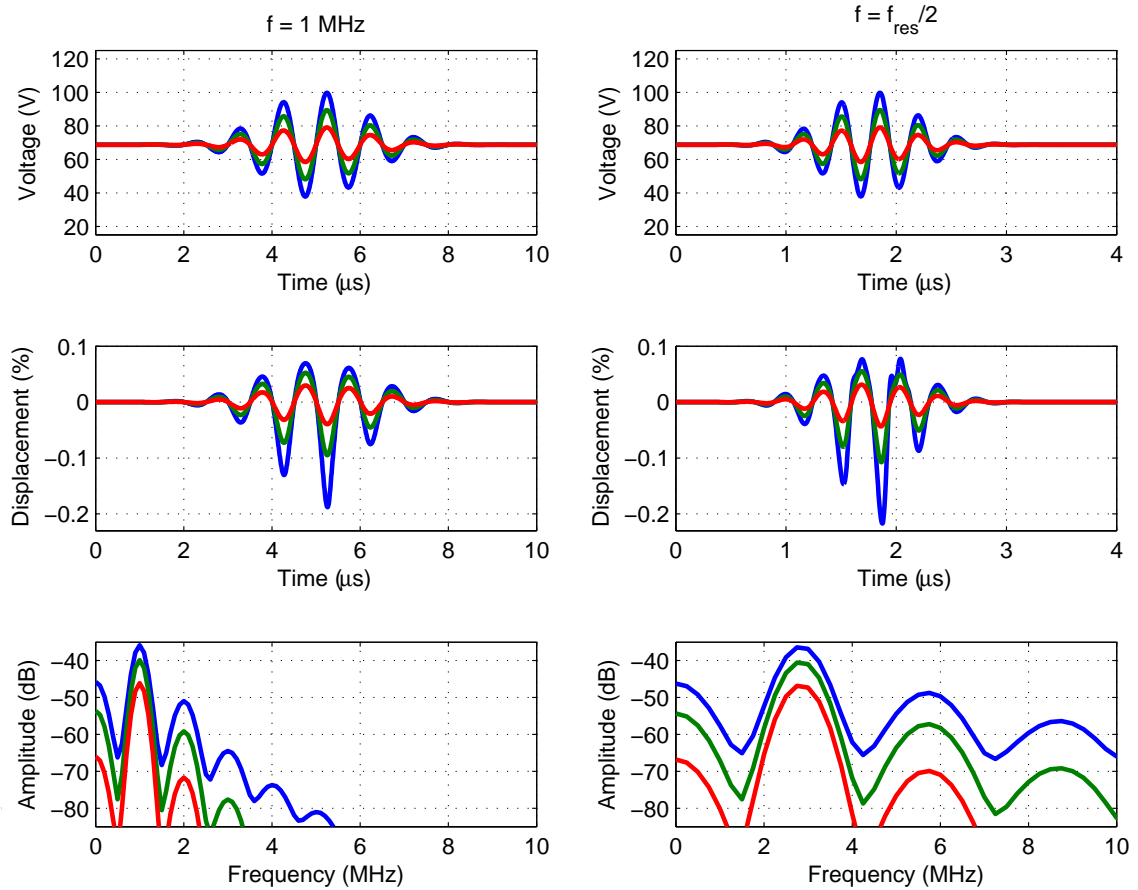


Figure 5.4 – cMUT command for different frequencies and voltages (20% in red, 40% in green and 60% in blue of the collapse voltage) on the first line. Displacement u_{mb} associated to the membrane in comparison with the cavity size on the second line. Membrane displacement spectra on the third line.

5.2 Methods

The principle of optimal command is described in Fig. 5.5 where the objective is to minimize the quadratic error e^2 between a target signal and the cMUT output y :

$$\min_{\mathbf{h}}(e^2) = \min_{\mathbf{h}} [(x - y)^2] \quad (5.4)$$

It is therefore a pre-setting carried out at the manufacturer before any clinical use.

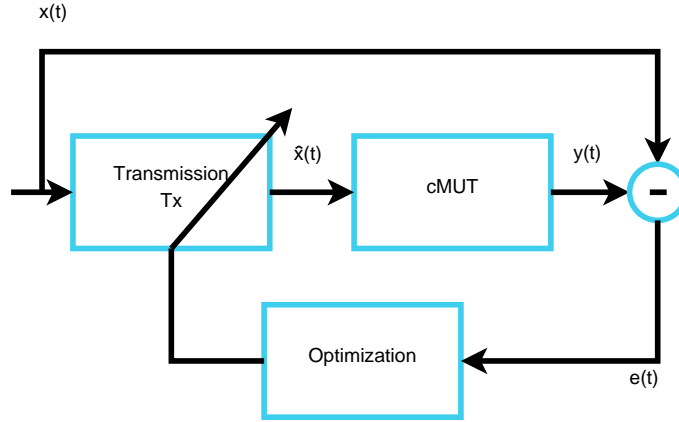


Figure 5.5 – Block diagram of cMUT optimal command to reach target signal x at output.

The optimal command takes the principle of a three-order nonlinear autoregressive and with a memory M . The cMUT input signal \hat{x} is constructed from parameters and the target signal to be reached such as:

$$\begin{aligned} \hat{x}(t) = & \sum_{i=1}^M h_1(i)x(t-i) + \sum_{i=1}^M \sum_{j=i}^M h_2(i,j)x(t-i)x(t-j) \\ & + \sum_{i=1}^M \sum_{j=i}^M \sum_{k=j}^M h_3(i,j,k)x(t-i)x(t-j)x(t-k) \end{aligned} \quad (5.5)$$

In order to reduce the number of freedom degrees of the command, we restrict ourselves to memory three, which results in a nine-parameter optimization considering that the kernels \mathbf{h} are symmetric [Lacoume et al., 1997].

5.2.1 Optimal Recursive Command

The recursive method uses the recursive least squares algorithm. The filter minimizes the error e between the target signal x and the cMUT output y such as:

$$e_t = x_t - y_t, \quad (5.6)$$

where y is the cMUT response to the excitation \hat{x} . The input signal \hat{x} is described thanks matrix by the following equation:

$$\hat{x}_t = \mathbf{x}_t^T \mathbf{h}_{t-1}, \quad (5.7)$$

5.3. OPTIMAL COMMAND OF ENCODED EXCITATION FOR CMUTS

where T is the transpose symbol and

$$\mathbf{x}_t = [x_{t-1}, x_{t-2}, \dots, x_{t-M+1}, x_{t-1}^2, x_{t-1}x_{t-2}, \dots, x_{t-M+1}^2, x_{t-1}^3, x_{t-1}^2x_{t-2}, \dots, x_{t-M+1}^3]^T,$$

$$\mathbf{h} = [h_1(1), h_1(2), \dots, h_{M-1}, h_2(1, 1), h_2(1, 2), \dots, h_2(M-1, M-1),$$

$$h_3(1, 1, 1), h_3(1, 1, 2), \dots, h_3(M-1, M-1, M-1)]^T.$$

We obtain the coefficients of the filter h [Michaut, 1992] by the following equation:

$$h_t = h_{t-1} + K_t e_t x_t, \quad (5.8)$$

with

$$\begin{cases} K_t = \frac{1}{\lambda_o} (K_{t-1} - s(v_t v_t^T)) \\ s = \frac{1}{\lambda_o + x_t^T v_t} \\ v_t = K_{t-1} x_t \end{cases} \quad (5.9)$$

where $\lambda_o = 0.999$ is the forgetting factor that offers the best performances.

5.2.2 Optimal Iterative Command

This second method calculates an mean squared error MSE for an whole signal:

$$MSE = \mathbb{E} ((x - y)^2). \quad (5.10)$$

Using the NELDER-MEAD algorithm, the setting of the nineteen parameters minimizes the mean squared error MSE at each new iteration. Thus, during an iteration, the algorithm proposes new values for the parameters. This solution is sent to the cMUT to measure the mean squared error MSE . From this measurement, the algorithm proposes new values.

5.3 Optimal Command of Encoded Excitation for cMUTs

We place ourselves in the context of harmonic imaging. Since there are many imaging techniques with encoded excitations, we deliberately restrict the imaging

techniques to three: second harmonic imaging, pulse inversion imaging and chirp reversal imaging. These different cases will be analyzed in simulation.

5.3.1 Optimal Command for second harmonic imaging

We place ourselves in the context of second harmonic imaging. Given the reception bandwidth, the excitation frequency is less than the central frequency f_c of the transducer.

In the framework of the optimal recursive command, we propose to reach a target point derived from a signal with a frequency of 1 MHz and whose amplitude represents a membrane displacement u_{mb} of $\pm 10\%$ of the cavity size. On the left, Fig. 5.6 shows the excitation signal at the top and the output of the cMUT compared to the target signal at the bottom. On the right, we have represented the spectra of these signals, and the spectrum of the cMUT output in the absence of optimization.

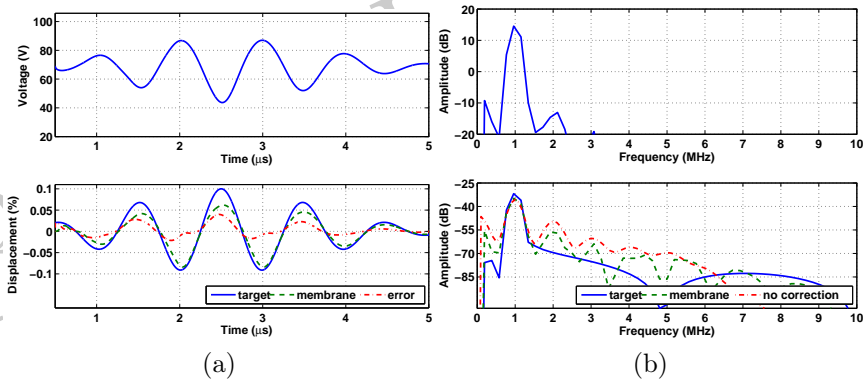


Figure 5.6 – Simulation of the recursive optimization of the cMUT output when the target signal to be reached is a sine wave signal of 1 MHz and amplitude representing a membrane displacement u_{mb} of $\pm 10\%$ of the size of the cavity. (a) cMUT Command at the top. Normalized cMUT output in relation to the cavity size, target signal and error at the bottom. (b) Spectrum of the cMUT command at the top. Spectrum of target signal and cMUT output before and after optimization at the bottom.

After optimization, the output has not quite reached the target signal, but the result is still satisfactory. There is still a non-negligible spectral error especially for the harmonic components. We propose two explanations. The first may be linked to a too low memory choice of the filter; the second is probably related to the fact that there is not enough information available to perform point-to-point optimization. To correct this effect, we propose a method which calculates the command signal in globality (optimal iterative command). An optimization will be achieved by

5.3. OPTIMAL COMMAND OF ENCODED EXCITATION FOR CMUTS

transmitting a complete signal to the cMUT and searching for a target signal, and not a target composed of a single point.

Fig. 5.7 shows the results of the iterative optimization when the target signal is a cosine modulated by a Gaussian with a frequency of 1 MHz and whose amplitude represents a membrane displacement u_{mb} of $\pm 10\%$ of the cavity size. Fig. 5.7 (left) shows the mean squared error MSE during the iterations k and the parameters that describe the excitation signal. Fig. 5.7 (center) shows the excitation signal (top) and the cMUT output and its target (bottom). Finally, Fig. 5.7 (right) shows the spectra of these signals and the cMUT output without any optimization.

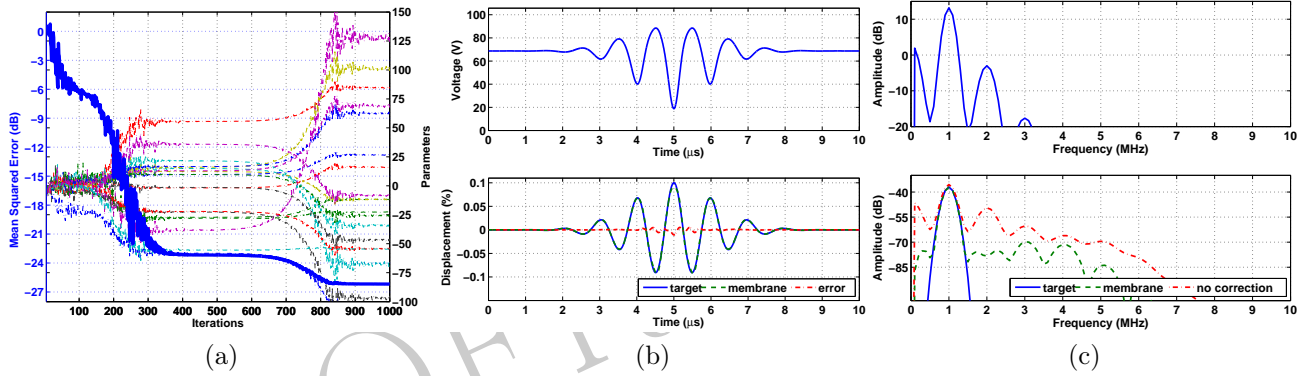


Figure 5.7 – Simulation of the iterative optimization of the cMUT output when the target signal to be reached is a sine wave signal of 1 MHz and amplitude representing a membrane displacement u_{mb} of $\pm 10\%$ of the size of the cavity. (a) Mean quadratic error between the target signal MSE and the membrane displacement u_{mb} during the iterations k with the input parameters of the system. (b) cMUT command at the top. Normalized cMUT output in relation to the cavity size, target signal and error at the bottom. (c) Spectrum of the cMUT command at the top. Spectrum of target signal and cMUT output before and after optimization at the bottom.

This optimization method makes it possible to reach the target signal more faithfully with regard to the results obtained by the optimal recursive command. The error reached -25 dB after one thousand iterations. The command is asymmetric in amplitude since the positive amplitudes are smaller than the negative amplitudes. This corresponds to the fact that the membrane is pulled towards the cavity bottom, knowing that it is more difficult to push the membrane towards the outside than towards the inside. The algorithm then proposes voltages much lower than the bias voltage. This phenomenon is expressed spectrally by a cMUT excitation including second and third harmonics. At the cMUT output, the harmonic components are greatly reduced by 25 dB for the second harmonic. The performances are then similar to the existing compensation techniques. However our method is automatic and does not include very precise parameter settings. Indeed, their values may

CHAPTER 5. OPTIMAL COMMAND OF A CAPACITIVE MICROMACHINED ULTRASOUND TRANSDUCERS

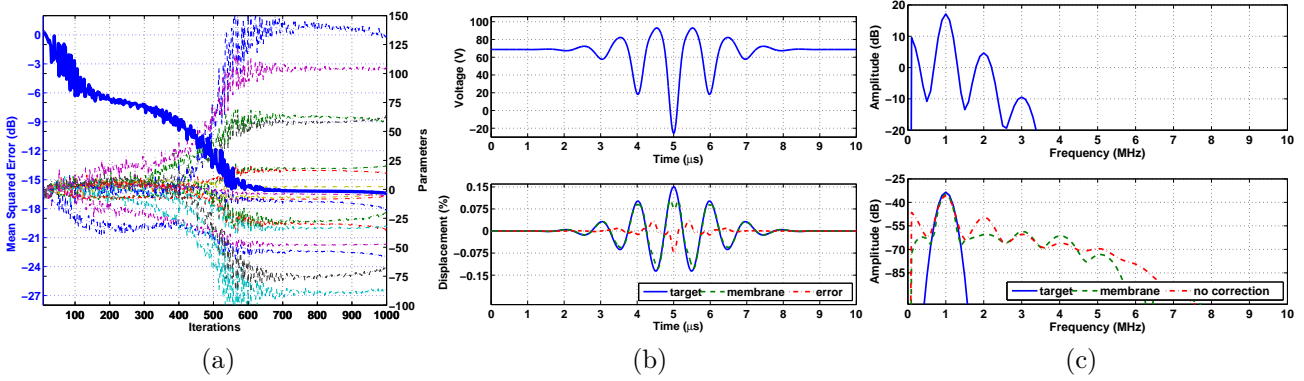


Figure 5.8 – Simulation of the iterative optimization of the cMUT output when the target signal to be reached is a sine wave signal of 1 MHz and amplitude representing a membrane displacement u_{mb} of $\pm 15\%$ of the size of the cavity. (a) Mean quadratic error between the target signal MSE and the membrane displacement u_{mb} during the iterations k with the input parameters of the system. (b) cMUT command at the top. Normalized cMUT output in relation to the cavity size, target signal and error at the bottom. (c) Spectrum of the cMUT command at the top. Spectrum of target signal and cMUT output before and after optimization at the bottom.

change slightly without compromising a large change in the mean square error MSE . Note that the proposed excitation solution has the same shape as the solution that optimizes the error between a target signal and the pressure proposed by OGUZ *et al.* [Oguz et al., 2010].

The second objective of the optimal command is to reach a target signal with the maximum amplitude. Indeed, the greater the amplitude, the greater the acoustic pressure of the generated wave, while limiting the number of cells constituting the cMUT. The new target signal is therefore at the same frequency of 1 MHz, but its amplitude represents a membrane displacement u_{mb} of $\pm 15\%$ of the cavity size. The figure 5.8 represents the results of this new optimal command.

The cMUT output is in this case faithful except for the strongest positive amplitude which is clipped. Indeed, it becomes physically impossible to obtain a displacement of the membrane to the outside with this amplitude. However spectrally, even if the performances are worse, the reduction of the second harmonic is still 10 dB.

We have also computed the optimal command for a target signal with a frequency equal to the half resonance frequency f_{res} . The performances are similar. The results are moved to appendix D (p. 159).

5.3.2 Optimal Command for pulse inversion imaging

In a context of pulse inversion imaging, it is important to be able to propose two optimal commands for the two excitations required for the pulse inversion. Since the first optimal command has been computed previously, we reproduce the search for the optimal command but with a target signal with a phase shifted by 180° .

The results are presented in the same way in Fig. 5.9.

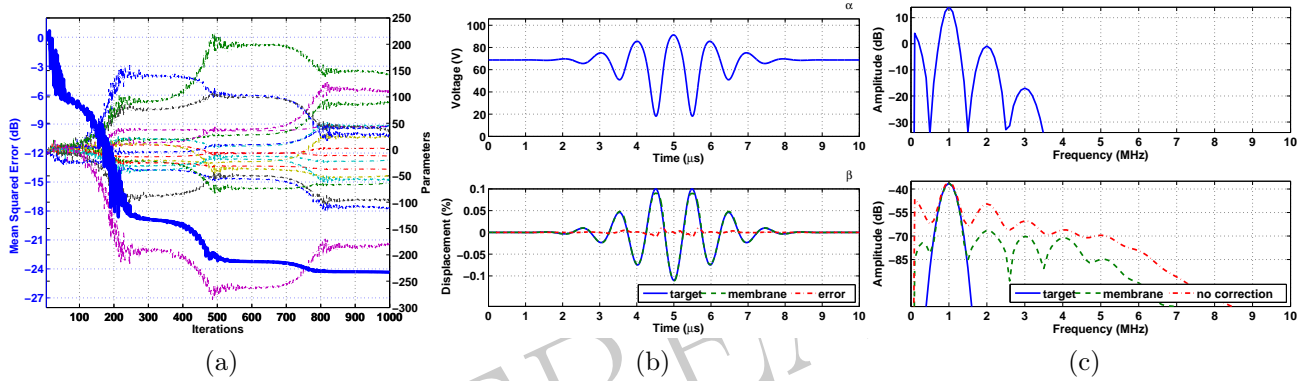


Figure 5.9 – Simulation of the iterative optimization of the cMUT output when the target signal to be reached is a sine wave signal of 1 MHz, in opposite phase to the target signal presented in Fig. 5.7b, and amplitude representing a membrane displacement u_{mb} of $\pm 10\%$ of the size of the cavity. (a) Mean quadratic error between the target signal MSE and the membrane displacement u_{mb} during the iterations k with the input parameters of the system. (b) cMUT command at the top. Normalized cMUT output in relation to the cavity size, target signal and error at the bottom. (c) Spectrum of the cMUT command at the top. Spectrum of target signal and cMUT output before and after optimization at the bottom.

The target signal is again correctly reached, but with a slightly larger error. Optimal command is performed by a nonlinear method that may require more iterations. However, the algorithm proposes a different excitation of the solution proposed in Fig. 5.7, which leaves the possibility to use the cMUT with encoded excitations. Each of the optimal commands is saved in the ultrasound system and then used in pulse inversion imaging with the cMUTs.

When the target signal has a frequency corresponding to the half resonance frequency f_{res} , the performances are similar and moved in appendix D (p. 159).

5.3.3 Optimal Command for imaging by chirp reversal

In order to show that our method can work with a target signal of our choice, we propose an imaging method where the target signal is more complicated with a

sinusoid modulated in frequency. We then place ourselves in the context of the chirp reversal imaging [Bouakaz, 2008].

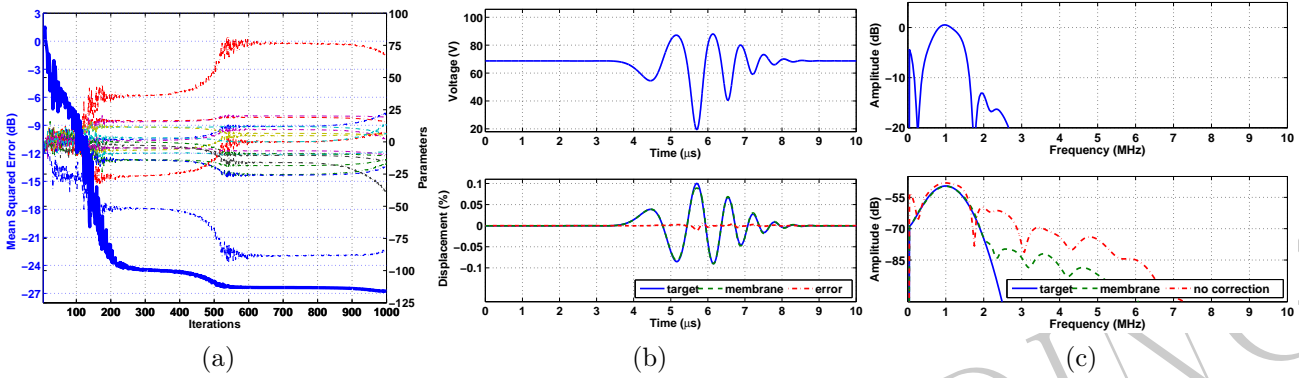


Figure 5.10 – Simulation of the iterative optimization of the cMUT output when the target signal to be reached is a sinusoidal frequency-modulated signal where $f_0 = 1$ MHz and $\beta_1 = 20$ GHz/s, and amplitude representing a membrane displacement u_{mb} of $\pm 10\%$ of the size of the cavity. (a) Mean quadratic error between the target signal MSE and the membrane displacement u_{mb} during the iterations k with the input parameters of the system. (b) cMUT command at the top. Normalized cMUT output in relation to the cavity size, target signal and error at the bottom. (c) Spectrum of the cMUT command at the top. Spectrum of target signal and cMUT output before and after optimization at the bottom.

The first target signal is centered at the frequency of 1 MHz and modulated with a linear modulation coefficient of 20 GHz/s, which corresponds to a high modulation coefficient. The second target signal has an opposite modulation coefficient.

This optimization is presented in Fig. 5.10 in the same way as the other cases, but where the target signal is frequency modulated.

The mean squared error MSE reaches -25 dB with an output from the cMUT that correctly reaches the target signal. Spectrally the optimal command allows to considerably reduce the harmonic frequencies.

To obtain both optimal commands required for the imaging method, we optimize with the target signal of the opposite modulation coefficient. The method proposes again a solution that correctly reaches the target signal.

The iterative search for optimal command can work with imaging methods using frequency modulation. If the objective is to make harmonic imaging by chirp, the optimal command consists only of the excitation proposed in Fig. 5.10b. If the aim is to make imaging by reversing frequency-modulated signals, it is sufficient to save both optimal commands that we have presented in this section.

5.4. CONCLUSION

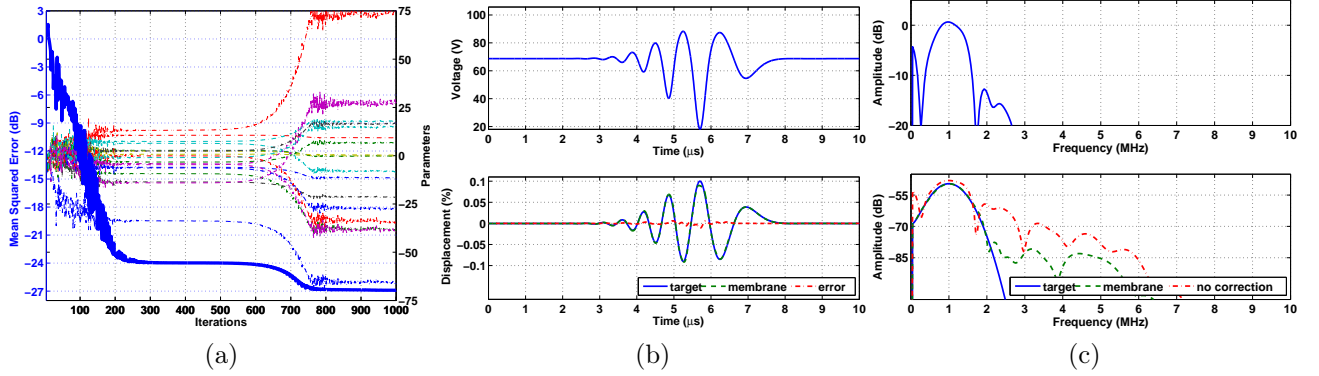


Figure 5.11 – Simulation of the iterative optimization of the cMUT output when the target signal to be reached is a sinusoidal frequency-modulated signal where $f_0 = 1$ MHz and $\beta_1 = -20$ GHz/s, and amplitude representing a membrane displacement u_{mb} of $\pm 10\%$ of the size of the cavity. (a) Mean quadratic error between the target signal MSE and the membrane displacement u_{mb} during the iterations k with the input parameters of the system. (b) cMUT command at the top. Normalized cMUT output in relation to the cavity size, target signal and error at the bottom. (c) Spectrum of the cMUT command at the top. Spectrum of target signal and cMUT output before and after optimization at the bottom.

When the target signal has a center frequency corresponding to the half resonant frequency and has the same modulation coefficient, the performances are close (appendix D, p. 159).

5.4 Conclusion

Our method makes it possible to reach a target signal at the output of a system, such as the cMUT, by correctly choosing the input signal. This target can be freely chosen without affecting performance. The advantage of our method is to offer a solution determined automatically from a restricted number of parameters. The optimal excitation compensates the cMUT nonlinearities at its output. However, the amplitude of the target signal can not exceed a threshold. The membrane behaviour seems to be the main cause of the nonlinearities. If the cMUT membrane can not physically reach the desired displacement u_{mb} , it is no longer possible to propose an excitation that corrects nonlinearities.

The next step will be to test our method with several cMUT membranes both in simulation and experimentally. However, the results are encouraging.

PROOFREADING

Conclusion

EXISTING ultrasound medical imaging systems have so far been able to progress and show better quality images through improved system sensitivity and post-treatments.

In this thesis, we focused not on these post-treatments but rather on the optimal command of the excitation of the imaging system. The ambitious goal, which we have set ourselves, was to find this command which optimizes a criterion in the system (the contrast for example) by means of a feedback. Until now, there have been few or no solutions for ultrasound imaging. The few methods proposed improved only one criterion but did not reach the optimal one. Moreover, it was possible to reach the optimum only empirically.

Our first major contribution was to simplify the complexity of the standard problem of optimal command by proposing realistic suboptimal parametric approaches. Now our methods have the advantage of finding the optimum automatically. The potential ubiquity of our optimal command methods also includes some advantageous properties. Here is a non-exhaustive list of these advantages:

1. the adjustment of the command is no longer a manual and difficult choice for the manufacturer or for the clinicians since the method proposes itself an optimal setting guaranteeing the best conditions of use;
2. no knowledge about the system or about the medium being explored is required because the method adapts itself to conditions of use, variations in the system or medium during the examination;
3. the optimization of a criterion is guaranteed at all times of the examination.

Three implementation stages of the loop back constitute the main part of the difficulty and the success of the search for the optimal command:

1. the cost function $J(\theta)$ must correctly describe the objective;
2. the variables θ which define the command must influence the cost function;
3. The algorithm must be robust enough to find the global maximum and it must be fast enough.

By responding correctly to these three points, the principle of optimal command can be applied in a large number of cases. Indeed, in absolute terms, the cost function is independent of the simulation model or of the experiment, since it takes iteratively into account only the measurements of the input and output signals of the imaging chain. We first applied this principle to harmonic imaging systems. Next, another major result of our approach is that it removes a technological barrier of considerable importance. Indeed, our methods will allow a wider use of capacitive transducers cMUTs in coded ultrasound imaging that was still inaccessible today. Finally, we imagine an application in the whole of the imaging and in particular for Doppler imaging.

Immediate implementation in commercial ultrasound scanner is not directly exploitable, since it is necessary to have a programmable analogue waveform generator. However, with the growing development of electronics, the use of our techniques in new ultrasonic imaging systems will be a major challenge for innovative companies for the next decade.

In our point of view, we also envisage the use of algorithms that will increase the convergence speed. For the same purpose, we will propose a reduction of the parameter number without reducing the degree of freedom of the waveform command. This will reduce the number of measurements per iteration.

Bibliography

- [Anderson, 2000] Anderson, M. E. (2000). A 2D Nonlinear Wave Propagation Solver Written in Open-Source MATLABCode. In *Proceeding IEEE Ultrasonic Symposium*, pages 1351–1354.
- [Åström and Wittenmark, 1994] Åström, K. J. and Wittenmark, B. (1994). *Adaptive Control*. Prentice Hall, Englewood Cliffs, NJ, United States of America.
- [Averkiou, 2000] Averkiou, M. A. (2000). Tissue Harmonic Imaging. In *Proceeding IEEE Ultrasonic Symposium*, volume 2, pages 1563–1572.
- [Barlow et al., 2011] Barlow, E., Mulholland, A. J., Gachagan, A., and Nordon, A. (2011). A Theoretical Investigation of Chirp Insonification of Ultrasound Contrast Agents. *Ultrasonics*, 51(6):725–733.
- [Becher and Burns, 2000] Becher, H. and Burns, P. N. (2000). *Handbook of Contrast Echocardiography : Left Ventricular Function and Myocardial Perfusion*. Springer, New York, NY, United States of America.
- [Borsboom et al., 2009] Borsboom, J. M. G., Bouakaz, A., and de Jong, N. (2009). Pulse Subtraction Time Delay Imaging Method for Ultrasound Contrast Agent Detection. *IEEE Transactions on Ultrasonics Ferroelectrics and Frequency Control*, 56(6):1151–1158.
- [Borsboom et al., 2005] Borsboom, J. M. G., Chin, C. T., Bouakaz, A., Versluis, M., and de Jong, N. (2005). Harmonic chirp imaging method for ultrasound contrast agent. *IEEE Transactions on Ultrasonics Ferroelectrics and Frequency Control*, 52(2):241–249.

- [Borsboom et al., 2003] Borsboom, J. M. G., Chin, C. T., and de Jong, N. (2003). Nonlinear Coded Excitation Method for Ultrasound Contrast Imaging. *Ultrasound in Medicine & Biology*, 29(2):277–284.
- [Bouakaz, 2008] Bouakaz, A. (2008). Chirp Reversal Ultrasound Contrast Imaging. (EP 20050291354).
- [Bouakaz et al., 2002] Bouakaz, A., Frigstad, S., Ten Cate, F. J., and de Jong, N. (2002). Super Harmonic Imaging: A New Imaging Technique for Improved Contrast Detection. *Ultrasound in Medicine & Biology*, 28(1):59–68.
- [Brock-fisher et al., 1996] Brock-fisher, G. A., Poland, M. D., and Rafter, P. G. (1996). Means for increasing sensitivity in non-linear ultrasound imaging systems. (US 5577505).
- [Burns, 2002] Burns, P. N. (2002). Instrumentation for Contrast Echocardiography. *Echocardiography*, 19(3):241–258.
- [Chiao and Hao, 2005] Chiao, R. and Hao, X. (2005). Coded Excitation for Diagnostic Ultrasound: a System Developer’s Perspective. *IEEE Transactions on Ultrasonics Ferroelectrics and Frequency Control*, 52(2):160–170.
- [Couture et al., 2008] Couture, O., Aubry, J. F., Montaldo, G., Tanter, M., and Fink, M. (2008). Suppression of Tissue Harmonics for Pulse-inversion Contrast Imaging Using Time Reversal. *Physics in Medicine & Biology*, 53(19):5469–5480.
- [de Jong et al., 2007] de Jong, N., Emmer, M., Chin, C. T., Bouakaz, A., Mastik, F., Lohse, D., and Versluis, M. (2007). “Compression-Only” Behavior of Phospholipid-Coated Contrast Bubbles. *Ultrasound in Medicine & Biology*, 33(4):653–656.
- [Dominguez et al., 2005] Dominguez, N., Gibiat, V., and Esquerre, Y. (2005). Time Domain Topological Gradient and Time Reversal Analogy: An Inverse Method for Ultrasonic Target Detection. *Wave Motion*, 42(1):31–52.
- [Fink, 1992] Fink, M. (1992). Time-reversal of Ultrasonic Fields .1. Basic Principles. *IEEE Transactions on Ultrasonics Ferroelectrics and Frequency Control*, 39(5):555–566.
- [Forsberg et al., 2000] Forsberg, F., Shi, W. T., and Goldberg, B. B. (2000). Subharmonic Imaging of Contrast Agents. *Ultrasonics*, 38(1-8):93–98.

REFERENCES

- [Frinking et al., 2000] Frinking, P. J. A., Bouakaz, A., Kirkhorn, J., Ten Cate, F. J., and de Jong, N. (2000). Ultrasound Contrast Imaging: Current and New Potential Methods. *Ultrasound in Medicine & Biology*, 26(6):965–975.
- [Ghrist et al., 2001] Ghrist, M., Fornberg, B., and Driscoll, T. A. (2001). Staggered Time Integrators for Wave Equations. *SIAM Journal on Numerical Analysis*, 38(3):718–741.
- [Girault, 2010] Girault, J.-M. (2010). *Analyses et traitements : de l'imagerie ultrasonore médicale aux séries temporelles biomédicales*. Habilitation à diriger des recherches, Université François Rabelais de Tours, Tours, France.
- [Golub and van Loan, 1989] Golub, G. H. and van Loan, C. F. (1989). *Matrix Computations*. Baltimore, United States of America, 2 edition.
- [Greis, 2004] Greis, C. (2004). Technology Overview: SonoVue (Bracco, Milan). *European Radiology*, 14:P11–P15.
- [Haller and Khuri-Yakub, 1996] Haller, M. I. and Khuri-Yakub, B. T. (1996). A Surface Micromachined Electrostatic Ultrasonic Air Transducer. *IEEE Transactions on Ultrasonics Ferroelectrics and Frequency Control*, 43(1):1–6.
- [Hossack et al., 2000] Hossack, J. A., Mauchamp, P., and Ratsimandresy, L. (2000). A High Bandwidth Transducer Optimized for Harmonic Imaging. In *Proceeding IEEE Ultrasonic Symposium*, volume 2, pages 1021–1024.
- [Idier, 2008] Idier, J. (2008). *Bayesian Approach to Inverse Problems*. ISTE Ltd and John Wiley & Sons Inc., London, United Kingdom.
- [Kirk, 2004] Kirk, D. E. (2004). *Optimal Control Theory: An Introduction*. Dover Publications Inc., Mineola, NY, United States of America.
- [Klauder et al., 1960] Klauder, J. R., Price, A. C., Darlington, S., and Albersheim, W. J. (1960). The Theory and Design of Chirp Radars. *The Bell System Technical Journal*, 38(4):745–808.
- [Lacoume et al., 1997] Lacoume, J.-L., Amblard, P.-O., and Comon, P. (1997). *Statistiques d'ordre supérieur pour le traitement du signal*. Masson, Paris, France.

- [Lingvall, 2004] Lingvall, F. (2004). *Time-domain Reconstruction Methods for Ultrasonic Array Imaging*. Phd thesis, Uppsala University, Uppsala, Sweden.
- [Lohfink and Eccardt, 2005] Lohfink, A. and Eccardt, P.-C. (2005). Linear and Nonlinear Equivalent Circuit Modeling of CMUTs. *IEEE Transactions on Ultrasonics Ferroelectrics and Frequency Control*, 52(12):2163–2172.
- [Marmottant et al., 2005] Marmottant, P., van der Meer, S., Emmer, M., Versluis, M., de Jong, N., Hilgenfeldt, S., and Lohse, D. (2005). A Model for Large Amplitude Oscillations of Coated Bubbles Accounting for Buckling and Rupture. *The Journal of the Acoustical Society of America*, 118(6):3499–3505.
- [Michaut, 1992] Michaut, F. (1992). *Méthodes adaptatives pour le signal : outils mathématiques et mise en oeuvre des algorithmes*. Hermes, Paris, France.
- [Misaridis, 2001] Misaridis, T. (2001). *Ultrasound Imaging Coded Signals*. Phd thesis, Technical University of Denmark, Lyngby, Denmark.
- [Misaridis and Jensen, 2005] Misaridis, T. and Jensen, J. A. (2005). Use of Modulated Excitation Signals in Medical Ultrasound. Part I: Basic Concepts and Expected Benefits. *IEEE Transactions on Ultrasonics Ferroelectrics and Frequency Control*, 52(2):177–191.
- [Mleczko et al., 2007] Mleczko, M., Wilkening, W. G., and Schmitz, G. (2007). Optimal Pulse Sequences for the Suppression of Memoryless Tissue Harmonics. In *Proceeding IEEE Ultrasonic Symposium*, pages 542–545.
- [Ménigot et al., 2009] Ménigot, S., Novell, A., Bouakaz, A., and Girault, J.-M. (2009). Improvement of the Power Response in Contrast Imaging with Transmit Frequency Optimization. In *Proceeding IEEE Ultrasonic Symposium*, pages 1–4.
- [Ménigot et al., 2010] Ménigot, S., Voicu, I., Novell, A., Elkateb Hachemi Amar, M., and Girault, J.-M. (2010). Adaptive Matched Filters for Contrast Imaging. In *Proceeding IEEE Ultrasonic Symposium*, pages 1–4.
- [Nelder and Mead, 1965] Nelder, J. A. and Mead, R. (1965). A Simplex Method for Function Minimization. *The Computer Journal*, 7(4):308–313.

REFERENCES

- [Novell et al., 2009] Novell, A., Legros, M., Felix, N., and Bouakaz, A. (2009). Exploitation of Capacitive Micromachined Transducers for Nonlinear Ultrasound Imaging. *IEEE Transactions on Ultrasonics Ferroelectrics and Frequency Control*, 56(12):2733–2743.
- [Oguz et al., 2010] Oguz, H. K., Olcum, S., Senlik, M. N., Tas, V., Atalar, A., and Koymen, H. (2010). Nonlinear Modeling of an Immersed Transmitting Capacitive Micromachined Ultrasonic Transducer for Harmonic Balance Analysis. *IEEE Transactions on Ultrasonics Ferroelectrics and Frequency Control*, 57(2):438–447.
- [Pauzin, 2009] Pauzin, M.-C. (2009). *Modélisation du comportement dynamique d'un agent de contraste ultrasonore*. Phd thesis, Université de Provence Aix-Marseille I, Marseille, France.
- [Phillips and Gardner, 2004] Phillips, P. and Gardner, E. (2004). Contrast-Agent Detection and Quantification. *European Radiology*, 14:4–10.
- [Phukpattaranont and Ebbini, 2003] Phukpattaranont, P. and Ebbini, E. S. (2003). Post-Beamforming Second-Order Volterra Filter for Pulse-Echo Ultrasonic Imaging. *IEEE Transactions on Ultrasonics Ferroelectrics and Frequency Control*, 50(8):987–1001.
- [Plesset, 1949] Plesset, M. S. (1949). The Dynamics of Cavitation Bubbles. *Journal of Applied Mechanics*, 16:277–282.
- [Prada and Fink, 1994] Prada, C. and Fink, M. (1994). Eigenmodes of the Time Reversal Operator: A Solution to Selective Focusing in Multiple-target Media. *Wave Motion*, 20(2):151–163.
- [Rao, 1994] Rao, N. A. H. K. (1994). Investigation of a Pulse Compression Technique for Medical Ultrasound: A Simulation Study. *Medical and Biological Engineering and Computing*, 32(2):181–188.
- [Reddy and Szeri, 2002] Reddy, A. J. and Szeri, A. J. (2002). Optimal Pulse-Inversion Imaging for Microsphere Contrast Agents. *Ultrasound in Medicine & Biology*, 28(4):483–494.

- [Sahuguet et al., 2010] Sahuguet, P., Gibiat, V., and Jacob, X. (2010). Quantitative Numerical Approach for Ultrasound Imaging with Time Domain Topological Energy. In *Proceeding of 20th International Congress on Acoustics*.
- [Simpson et al., 1999] Simpson, D. H., Chin, C. T., and Burns, P. N. (1999). Pulse Inversion Doppler: A New Method for Detecting Nonlinear Echoes from Microbubble Contrast Agents. *IEEE Transactions on Ultrasonics Ferroelectrics and Frequency Control*, 46(2):372–382.
- [Soetanto and Chan, 2000] Soetanto, K. and Chan, M. (2000). Study on the Lifetime and Attenuation Properties of Microbubbles Coated with Carboxylic Acid Salts. *Ultrasonics*, 38(10):969–977.
- [Song et al., 2011] Song, J., Chang, J. H., Song, T.-K., and Yoo, Y. (2011). Coded Tissue Harmonic Imaging with Nonlinear Chirp Signals. *Ultrasonics*, 51(4):516–521.
- [Stepanishen, 1978] Stepanishen, P. R. (1978). Radiated Power and Radiation Loading of Cylindrical Surfaces With Nonuniform Velocity Distributions. *The Journal of the Acoustical Society of America*, 63(2):328–338.
- [Synnevag et al., 2007] Synnevag, J. F., Austeng, A., and Holm, S. (2007). Adaptive Beamforming Applied to Medical Ultrasound Imaging. *IEEE Transactions on Ultrasonics Ferroelectrics and Frequency Control*, 54(8):1606–1613.
- [Szabo, 2004] Szabo, T. (2004). *Diagnostic Ultrasound Imaging: Inside Out*. Academic Press, London, United Kingdom.
- [Sénégon, 2010] Sénégon, N. (2010). *Approche temporelle de la simulation et de la caractérisation des transducteurs ultrasonores capacitifs micro-usinés*. Phd thesis, Université François Rabelais de Tours, Tours, France.
- [Tauber, 2005] Tauber, C. (2005). *Filtrage anisotrope robuste et segmentation par B-splin snake : application aux images échographiques*. Phd thesis, Institut national polytechnique de Toulouse, Toulouse, France.
- [Tranquart et al., 2007a] Tranquart, F., Correas, J.-M., and Bouakaz, A. (2007a). *Échographie de contraste, Méthodologie et applications cliniques*, chapter Principes

BIBLIOGRAPHY

- physiques des méthodes d'imagerie de contraste, pages 45–57. Springer, Paris, France.
- [Tranquart et al., 2007b] Tranquart, F., Correas, J.-M., and Bouakaz, A. (2007b). *Échographie de contraste, Méthodologie et applications cliniques*, chapter Dynamique de la microbulle, pages 25–43. Springer, Paris, France.
- [van der Meer et al., 2004] van der Meer, S. M., Versluis, M., Lohse, D., Chin, C. T., Bouakaz, A., and de Jong, N. (2004). The Resonance Frequency of SonoVue(TM) as Observed by High-Speed Optical Imaging. In *Proceeding IEEE Ultrasonic Symposium*, volume 1, pages 343–345.
- [Widrow and Stearns, 1985] Widrow, B. and Stearns, S. (1985). *Adaptive Signal Processing*. Prentice Hall, Englewood Cliffs, United States of America.
- [Wild and Neal, 1951] Wild, J. J. and Neal, D. (1951). Use of High-frequency Ultrasonic Waves for Detecting Changes of Texture in Living Tissues. *The Lancet*, 257(6656):655–657.
- [Wilhjelm, 1993] Wilhjelm, J. (1993). Bandwidth Expressions of Gaussian Weighted Chirp. *Electronics Letters*, 29(25):2161–2162.
- [Wojcik et al., 1997] Wojcik, G., Fomberg, B., Waag, R., Carcione, L., Mould, J., Nikodym, L., and Driscoll, T. (1997). Pseudospectral Methods for Large-scale Bioacoustic Models. In *Proceeding IEEE Ultrasonic Symposium*, volume 2, pages 1501–1506.
- [Zhou et al., 2004] Zhou, S., Reynolds, P., and Hossack, J. (2004). Precompensated Excitation Waveforms to Suppress Harmonic Generation in MEMS Electrostatic Transducers. *IEEE Transactions on Ultrasonics Ferroelectrics and Frequency Control*, 51(11):1564–1574.

PROOFREADING

Appendix

PROOFREADING

PROOFREADING

Appendix A

Optimization algorithm



OPTIMIZATION algorithms are numerous. But all of them aim to minimize a cost function ^a using parameters that the algorithm needs to determine. Some algorithms offer better robustness and others a better convergence speed. For example, in the case of very complex optimizations, metaheuristics, such as simulated annealing, are a class of optimization algorithms that attempt to obtain an approximate value of the global optimum. However, since the latter are relatively complex, we have made the choice of simpler implementation algorithms.

In this thesis, we used two different algorithms: the gradient-based method and the NELDER-MEAD method. The first algorithm is reputed to be simple, while the second algorithm offers better robustness.

A.1 Algorithm based on the Gradient

The feedback of our closed-loop systems corresponds to our optimization algorithm. The algorithm optimizes a cost function $J(\mathbf{w})$ in an iterative way. The algorithm is based on the principle of gradient descent defined by the following recurrence relation [Widrow and Stearns, 1985] :

$$\mathbf{w}_{k+1} = \mathbf{w}_k + \mu_k(\nabla J), \quad (\text{A.1})$$

where $\mathbf{w}_k = [w_{1,k} \cdots w_{N,k}]^T$ is the vector of the N optimization parameters in the iteration k ^b. The coefficient vector $\mu_k = [\mu_{1,k} \cdots \mu_{N,k}]^T$ leads the direction and

^aMaximizing is to minimize the opposite of the function

^b T is the symbol of the transpose.

speed of convergence. Finally, the gradient at the iteration k and for the parameter w_i is expressed according to the following equation:

$$\nabla_{i,k}(J) = \frac{\partial J}{\partial w_i} = \frac{J(w_{j,k}, w_{i,k}) - J(w_{j,k-1}, w_{i,k})}{w_{i,k} - w_{i,k-1}}. \quad (\text{A.2})$$

However, since the gradient is a ratio of two quantities of different dimensions, we modify the recurrence relation such that:

$$\mathbf{w}_{k+1} = \mathbf{w}_k + \mu_k \cdot \Delta \mathbf{w}, \quad (\text{A.3})$$

where $\Delta \mathbf{w} = [\Delta w_1 \cdots \Delta w_N]^T$. When the dimension of w_i is a frequency, Δw_i is 50 kHz; while w_i expresses the α ratio (in chapter 3), then Δw_i is 5/100.

The direction of convergence is applied to the coefficient μ_k . This coefficient is initialized with $w_i = 2$ and is defined by equation A.4:

$$\mu_{i,k} = \begin{cases} \mu_{i,k-1} & \text{if } \text{sign}[\nabla_{i,k}(J)] = \text{sign}[\nabla_{i,k-1}(J)] \\ -\frac{\mu_{i,k-1}}{2} & \text{if } \text{sign}[\nabla_{i,k}(J)] \neq \text{sign}[\nabla_{i,k-1}(J)] \end{cases}, \quad (\text{A.4})$$

where $\text{sign}(t)$ is the sign function that is equal to 1 if $t > 0$, 0 if $t = 0$ and -1 if $t < 0$. Note that an initialization phase of 3^N steps is required to start the optimization.

A.2 NELDER-MEAD Algorithm

The NELDER-MEAD method is a nonlinear optimization algorithm [Nelder and Mead, 1965], known to be more robust than the gradient method. It is sometimes called a simplex method or “simplex downhill” and is based on the simplex concept. The simplex is a generalization of the triangle to any dimension. Thus the algorithm seeks the maximum of the cost function J by progressively surrounding it in the simplex.

First, an initialization phase is necessary to define the coordinates $\mathbf{w}' = [w'_1, \dots, w'_{N+1}]$ of the $N + 1$ vertices of the first simplex, where N is the degree of freedom of the cost function J . The cost function is evaluated in all vertices of the simplex.

Then the algorithm starts the iterative phase which looks for the minimum of the cost function J :

A.2. NELDER-MEAD ALGORITHM

1. the measurements of the cost function for the $N + 1$ vertices of the simplex are sorted in ascending order and reindexed as:

$$J(w_1) \leq J(w_2) \leq \dots \leq J(w_{N+1});$$

2. the gravity center of the simplex w_G from \mathbf{w} is calculated to deduce the cost function from these coordinates;
3. the cost function is evaluated at the point of reflection from w_{N+1} :

$$w_R = w_G + \mu_R(w_G - w_{N+1}).$$

These coordinates correspond to the reflection point of the maximum of the cost function with respect to the gravity center w_G . If the reflection point w_R is better than the penultimate point w_N and greater than the first point w_1 ($J(w_1) \leq J(w_R) \leq J(w_N)$) then a new simplex is formed by replacing the worst point by w_{N+1} by the reflection point, and returning to step 1;

4. if the reflection point w_R is better than the first point w_1 , then the simplex does not contain the minimum of the cost function J . An extension point is then determined such that:

$$w_E = w_G + \mu_E(w_G - w_{N+1}).$$

If the extension point w_E is better than the reflection point w_R ($J(w_E) < J(w_R)$) then a new simplex is formed by replacing the worst point w_{N+1} by the extension point w_E . Otherwise a new simplex is constructed by replacing w_{N+1} with w_R . Return to step 1;

5. if the reflection point w_R is greater than the penultimate point w_N ($J(w_R) \geq J(w_N)$), then a contraction point w_C is determined such that:

$$w_C = w_{N+1} + \mu_C(w_G - w_{N+1}).$$

If the contraction point is better than the worst point ($J(w_C) < J(w_{N+1})$), then a new simplex is determined by replacing the worst point w_{N+1} with the contraction point w_C and return to step 1;

6. if the contraction point w_C is greater than the worst point w_{N+1} ($J(w_C) > J(w_{N+1})$), then the simplex is reduced by replacing all vertices such as:

$$w_i = w_1 + \mu(w_i - w_1),$$

and return to step 1.

The reflection coefficient μ_R , the extension coefficient μ_E , the contraction coefficient μ_C and the reduction coefficient μ_ζ are usually chosen such that:

$$\begin{cases} \mu_R = 1, \\ \mu_E = 2, \\ \mu_C = \frac{1}{2}, \\ \mu_\zeta = \frac{1}{2}, \end{cases}$$

It should be noted that it is sometimes necessary to normalize the vector w so that all the parameters have the same order of magnitude for a good optimization.

Appendix B

Optimal Command in Pulse Inversion Imaging

THIS appendix shows the results of optimal command in pulse inversion imaging using the family of truncated half-sine waves presented in section 3.2.2 (p. 87).

B.1 Setting of the Frequencies of Truncated Half-Sine Waves

Here, we show that the simultaneous setting of the frequencies of two half-sine waves makes it possible to increase the *CTR* in comparison with the only optimization of the frequency f_0 . First, we check the existence of this maximum. Moreover, we verify that it is not at the position $f_1 = f_2$. Fig. B.1 presents the empirical search of frequencies f_1 and f_2 for a pressure level A_0 of 400 kPa. We also report automatic searches using the gradient algorithm by a black line and the NELDER-MEAD algorithm by a white line.

The automatic optimization of the *CTR* by the frequencies f_1 and f_2 is shown in Fig. B.2. Fig. B.2a presents the optimization by the gradient algorithm while Fig. B.2b presents the optimization by the Nelder-Mead algorithm with a white line.

APPENDIX B. OPTIMAL COMMAND IN PULSE INVERSION IMAGING

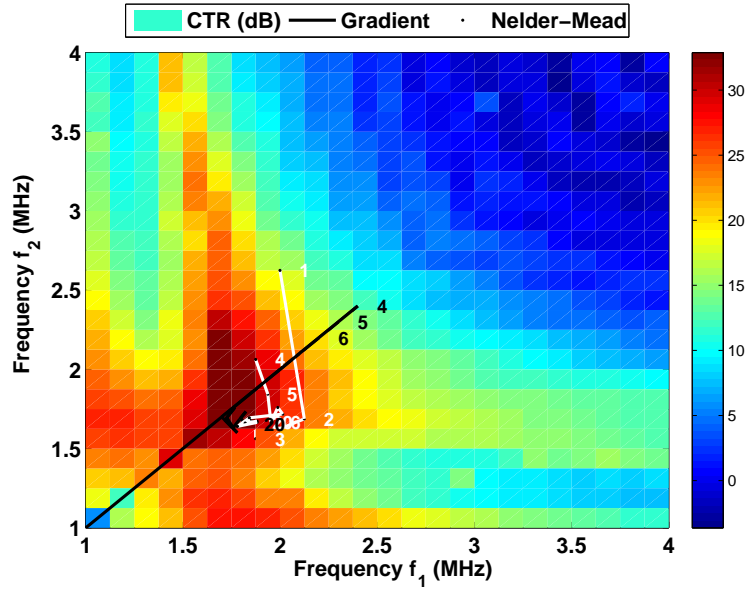


Figure B.1 – Simulation of the empirical search of the CTR maximum as a function of the frequencies f_1 and f_2 of the truncated half-sine waves in pulse inversion imaging by for a pressure level $A_0 = 400$ kPa. The automatic searches are reported in black for the gradient algorithm and in white for the NELDER-MEAD algorithm.

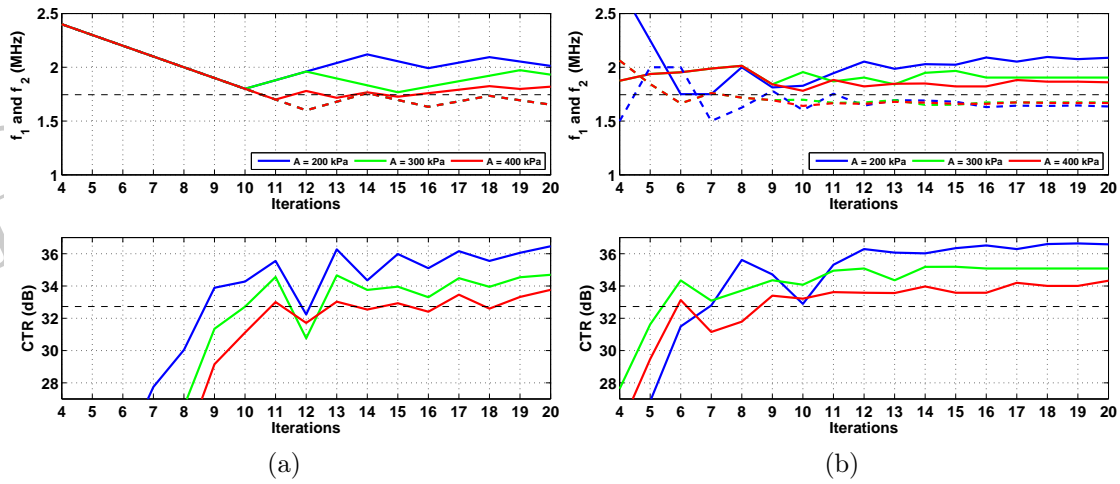


Figure B.2 – Simulations of the automatic optimizations using the frequencies f_1 and f_2 of the truncated half-sine waves in pulse inversion imaging for different pressure levels A_0 by the algorithm based on the gradient (a) and the NELDER-MEAD (b). The frequencies f_1 are written in solid lines, while the frequencies f_2 are dotted.

B.2. SETTING OF THE AMPLITUDE RATIO BETWEEN THE TRUNCATED HALF-SINE WAVES

Finally, we present the synthetic image with the suboptimal excitation that we calculated previously.=

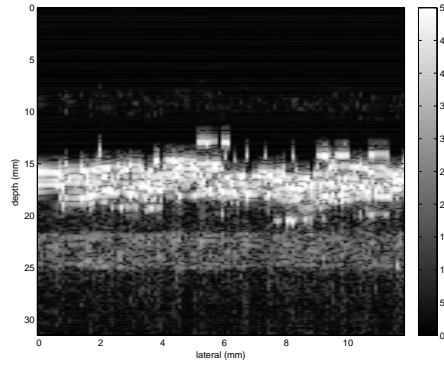


Figure B.3 – Synthetic image in pulse inversion imaging for a pressure level of $A_0 = 400$ kPa and with the optimal values of $f_{1,opt}$ and $f_{2,opt}$.

B.2 Setting of the Amplitude Ratio Between the Truncated Half-Sine Waves

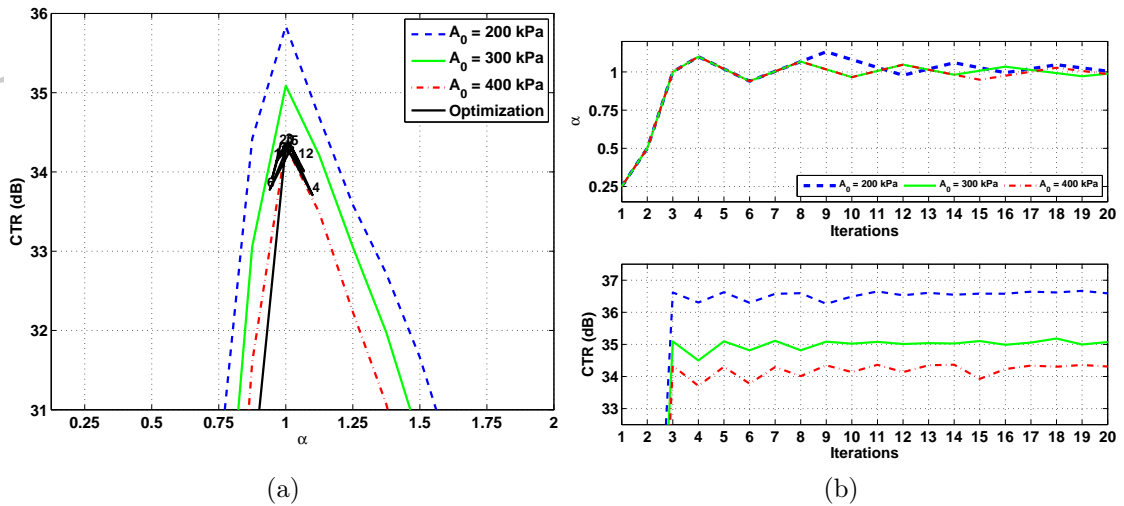


Figure B.4 – Simulations of the optimizations using the amplitude ratio α ratio in pulse inversion imaging for different pressure levels A_0 . (a) Empirical searches of the CTR maxima as a function of α . The automatic optimization path for the pressure level $A_0 = 400$ kPa is marked in black. (b) Automatic search of CTR using α by an algorithm using the gradient.

This third optimization in pulse inversion imaging sets the ratio α by considering the values of the frequencies $f_{1,opt}$ and $f_{2,opt}$ obtained in the previous optimization.

Fig. B.4a represents the CTR as a function of the α ratio and for different pressure levels A_0 . At the top of the Fig. B.4b, the CTR is represented during the k iterations, while at the bottom of the figure the associated α_k parameter is represented. The optimal α ratio is very slightly different from 1.

The image obtained for this ratio α is shown in Fig. B.5.

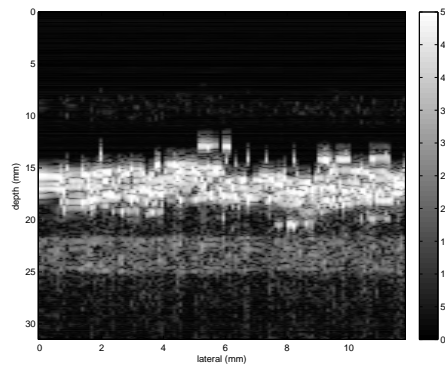


Figure B.5 – Synthetic image in pulse inversion imaging for a pressure level of $A_0 = 400$ kPa and with the optimal values of $f_{1,opt}$ and $f_{2,opt}$, and after optimization of α .

B.3 Setting of the Frequencies and the Amplitude Ratio of the Truncated Half-Sine Waves

This last proposition of parameters for the pulse inversion imaging proposes to simultaneously optimize the frequencies f_1 , f_2 and the ratio α of the amplitudes of the truncated half-sine waves. Fig. B.6 represents the CTR as a function of the k iterations at the bottom, the frequencies of the truncated half-sine waves followed by the α which set the amplitudes. First, this optimization offers a higher CTR than the previous optimization. Then the speed of convergence did not change. Finally, note that f_1 is smaller than f_2 .

We compute the synthetic image represented in Fig. B.7 for an excitation with these optimal parameters.

B.3. SETTING OF THE FREQUENCIES AND THE AMPLITUDE RATIO OF THE TRUNCATED HALF-SINE WAVES

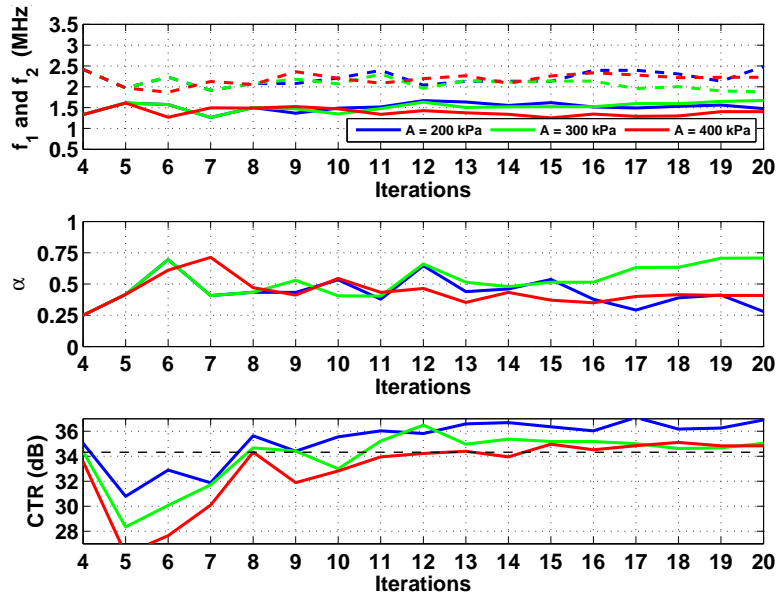


Figure B.6 – Simulations of automatic optimizations using the frequencies f_1 and f_2 , and the amplitude ration α in pulse inversion imaging for different pressure levels A_0 . The frequencies f_1 are written in solid lines, while the frequencies f_2 are dotted.

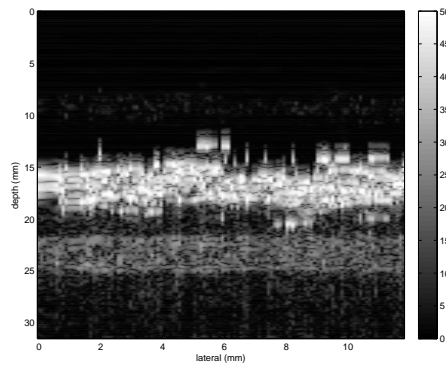


Figure B.7 – Synthetic image in pulse inversion imaging for a pressure level of $A_0 = 400$ kPa after optimization of f_1 , f_2 and α .

PROOFREADING

Appendix C

Optimal Command in Imaging by Phase and Amplitude Modulation

THIS appendix presents the results of optimal command in imaging by phase and amplitude modulation using the family of truncated half-sine waves presented in section 3.2.3 (p. 94).

C.1 Setting of the Excitation Frequency

We start with optimization with only one parameter. The Fig. C.1 presents the *CTR* optimization as a function of the excitation frequency f_0 . Fig. C.1a presents the empirical maximum search of the *CTR* at the top, while the automatic optimization is presented at the bottom.

First, as for the other imaging methods, we find the presence of a single maximum in the *CTR* function. However, the optimal frequency is different from that of other imaging methods. The pressure level A_0 influences the *CTR* maximum and its optimal frequency. When the pressure level is lower, the non-linearities in the tissue are lower, which does not deteriorate the *CTR*. The automatic optimization of the frequency finds the frequency which makes it possible to obtain the maximum *CTR*. As an illustration, we have superimposed our optimization for the pressure level A_0 (black line) to the empirical research curve in Fig. C.1a.

As with other imaging methods, we observe this result on synthetic images. The first two are references (the first at the central frequency f_c , the second at two thirds of the central frequency f_c), while the last one presents the results after our

APPENDIX C. OPTIMAL COMMAND IN IMAGING BY PHASE AND AMPLITUDE MODULATION

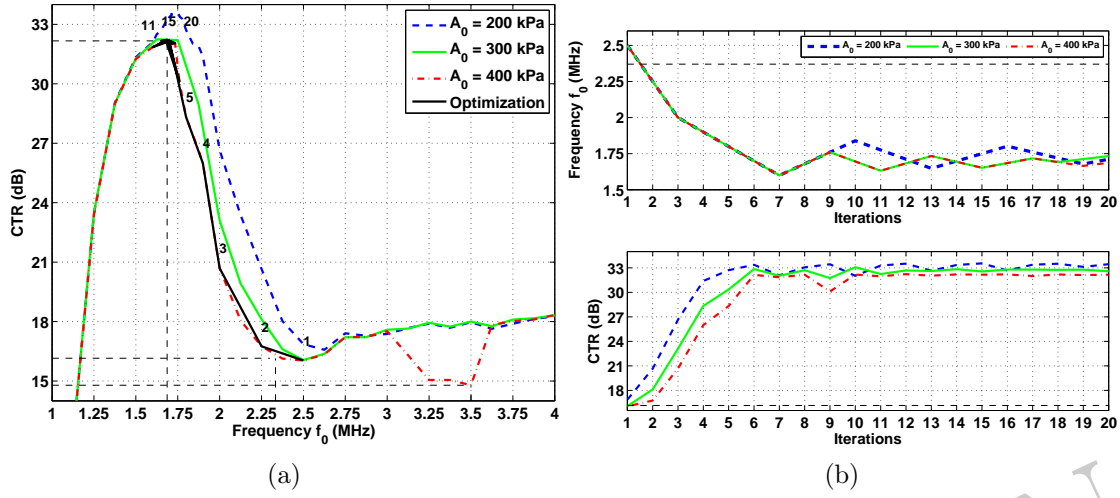


Figure C.1 – Simulations of optimizations using the excitation frequency f_0 in imaging by phase and amplitude modulation for different pressure levels A_0 . (a) Empirical investigations of the CTR maxima as a function of the excitation frequency $f_{0,k}$. The automatic optimization path for the pressure level $A_0 = 400$ kPa is depicted in black. (b) Automatic search of the CTR using the excitation frequency $f_{0,k}$ by an algorithm using the gradient.

optimization.

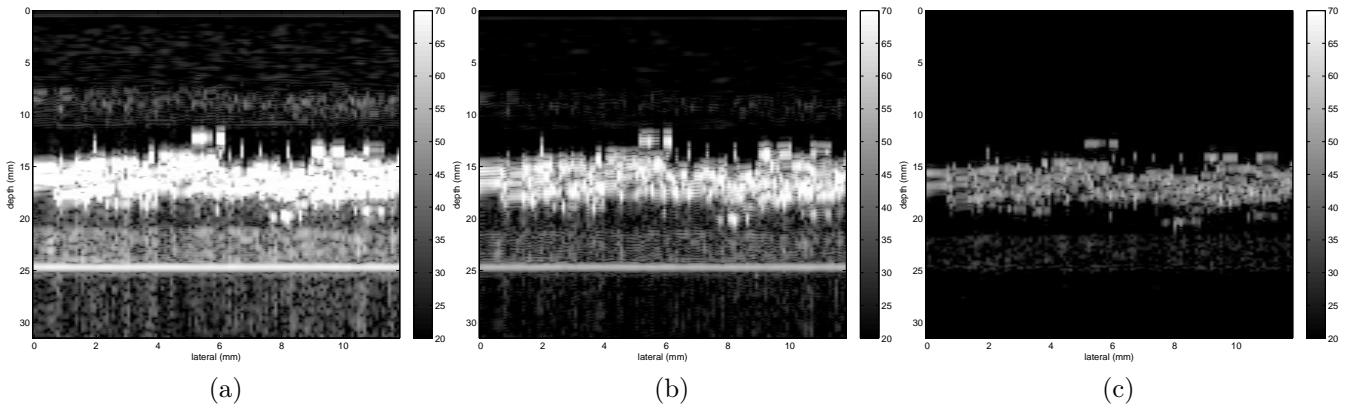


Figure C.2 – Synthetic images in imaging by phase and amplitude modulation for a pressure level of $A_0 = 400$ kPa where the excitation frequency f_0 is (a) the center frequency f_c of the transducer ($f_c = 3.5$ MHz), (b) the two-thirds of the center frequency f_c of the transducer ($2/3f_c = 2.33$ MHz), (c) the optimal frequency ($f_{0,opt} = 2.28$ MHz).

Finally, we tested this principle experimentally. After a few iterations, the algorithm converges to the CTR maximum.

C.2. SETTING OF THE FREQUENCIES OF TRUNCATED HALF-SINE WAVES

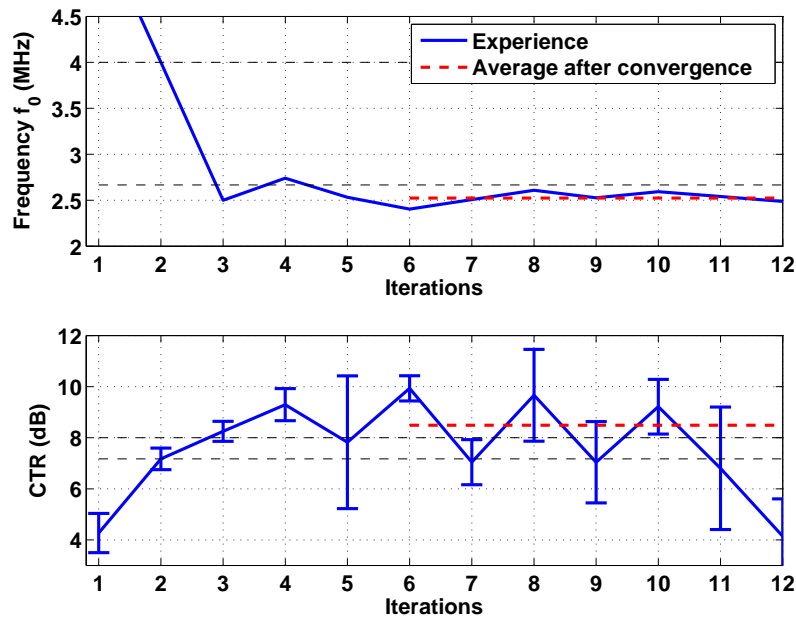


Figure C.3 – Experiment of automatic optimization using the frequency of excitation f_0 in imaging by phase and amplitude modulation by a gradient algorithm.

C.2 Setting of the Frequencies of Truncated Half-Sine Waves

This second optimization consists in increasing by one degree of freedom by the search for an optimal setting of f_1 and f_2 .

Fig. C.4 represents the CTR as a function of the frequencies f_1 and f_2 . The CTR maximum is obtained when the frequencies f_1 and f_2 are close.

The second step is to find this maximum by one of our optimization algorithms. Fig. C.5a presents the automatic optimization using our gradient algorithm, while Fig. C.5b shows the optimization by the Nelder-Mead algorithm. In these two figures, the CTR is represented as a function of the iterations k at the bottom, the associated frequencies at the top.

APPENDIX C. OPTIMAL COMMAND IN IMAGING BY PHASE AND AMPLITUDE MODULATION

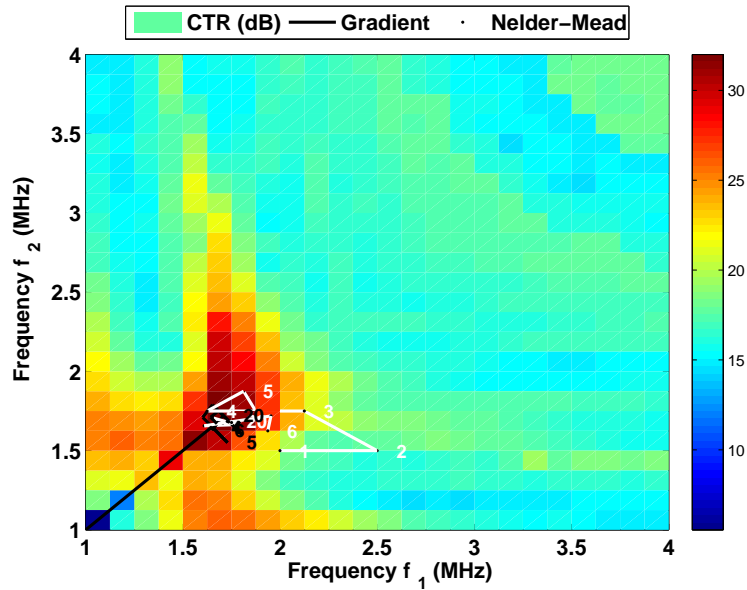


Figure C.4 – Simulation of the empirical search of the CTR maximum as a function of the frequencies f_1 and f_2 of the truncated half-sine waves in imaging by phase and amplitude modulation for a pressure level $A_0 = 400$ kPa. The automatic searches are reported in black for the gradient algorithm and in white for the NELDER-MEAD algorithm.

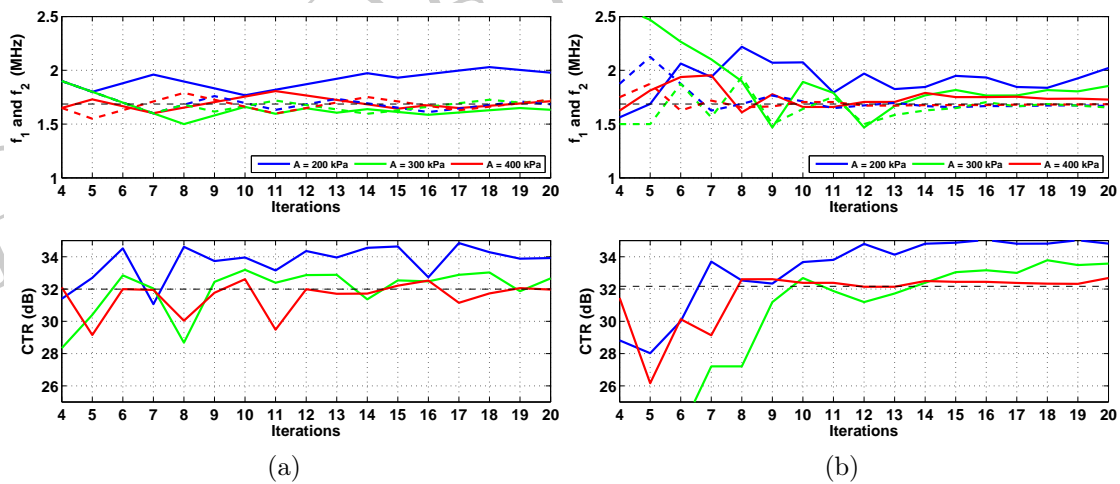


Figure C.5 – Simulations of the automatic optimizations using the frequencies f_1 and f_2 of the truncated half-sine waves in imaging by phase and amplitude modulation for different pressure levels A_0 by the algorithm based on the gradient (a) and the NELDER-MEAD (b). The frequencies f_1 are written in solid lines, while the frequencies f_2 are dotted.

C.3. SETTING OF THE AMPLITUDE RATIO BETWEEN THE TRUNCATED HALF-SINE WAVES

This result is observed on a synthetic image in Fig. C.6.

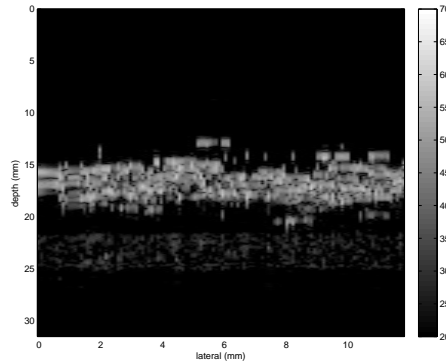


Figure C.6 – Synthetic image in imaging by phase and amplitude modulation for a pressure level of $A_0 = 400$ kPa and with the optimal values of $f_{1,opt}$ and $f_{2,opt}$.

C.3 Setting of the Amplitude Ratio Between the Truncated Half-Sine Waves

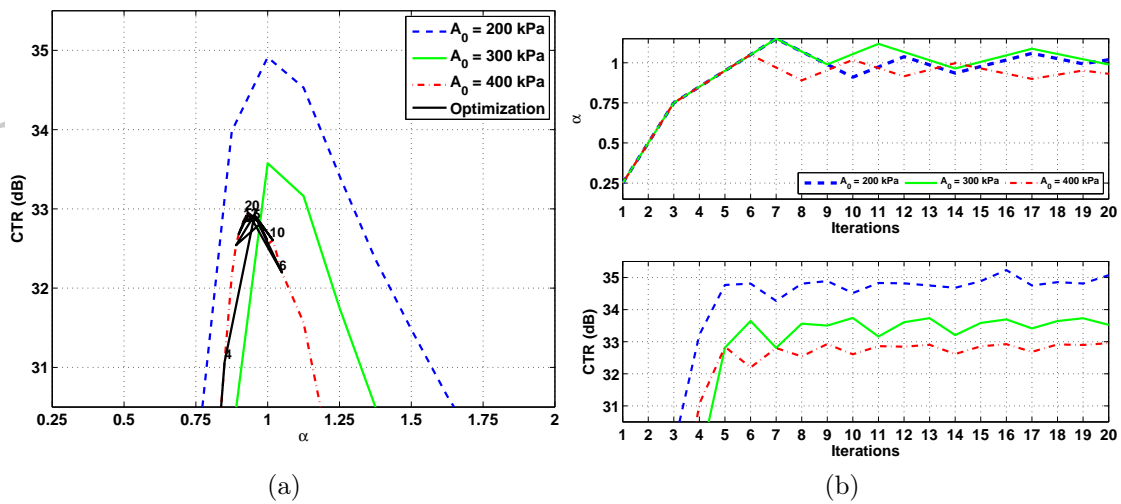


Figure C.7 – Simulations of the optimizations using the amplitude ratio α ratio in imaging by phase and amplitude modulation for different pressure levels A_0 . (a) Empirical searches of the CTR maxima as a function of α . The automatic optimization path for the pressure level $A_0 = 400$ kPa is marked in black. (b) Automatic search of CTR using α by an algorithm using the gradient.

This third optimization takes up the previous result, but optimizes the ratio α which sets the amplitudes of the truncated half-sine waves. Fig. C.7a represents the CTR as a function of the ratio α for different pressure levels A_0 . This parameter

makes it possible to reach a new CTR maximum when α is slightly different from 1. Fig. C.7b shows the automatic optimization that is associated.

As an illustration, let us observe the synthetic image (Fig. C.8) which offers the optimal CTR in this case.

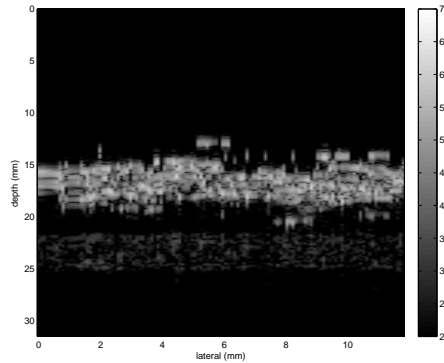


Figure C.8 – Synthetic image in imaging by phase and amplitude modulation for a pressure level of $A_0 = 400$ kPa and with the optimal values of $f_{1,opt}$ and $f_{2,opt}$, and after optimization of α .

C.4 Setting of the Frequencies and the Amplitude Ratio of the Truncated Half-Sine Waves

Finally, this last optimization, represented in Fig. C.9, proposes a simultaneous adjustment of the frequencies f_1 , f_2 and the ratio α of the amplitudes of the truncated half-sine waves.

We compute the synthetic image (Fig. C.10) where the excitation is determined with the optimal parameters.

C.4. SETTING OF THE FREQUENCIES AND THE AMPLITUDE RATIO OF THE TRUNCATED HALF-SINE WAVES

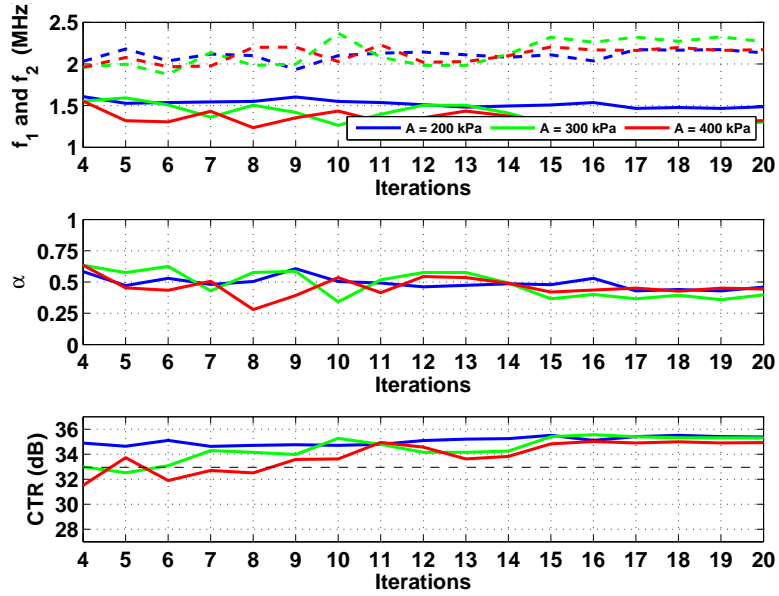


Figure C.9 – Simulations of automatic optimizations using the frequencies f_1 and f_2 , and the amplitude ratio α in imaging by phase and amplitude modulation for different pressure levels A_0 . The frequencies f_1 are written in solid lines, while the frequencies f_2 are dotted.

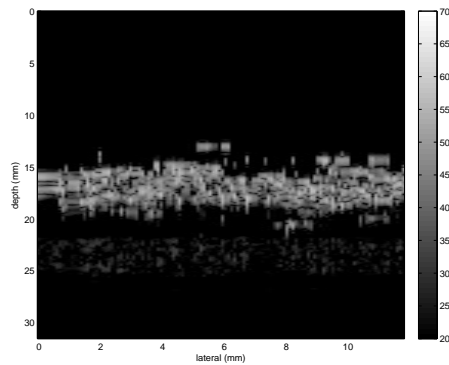


Figure C.10 – Synthetic image in imaging by phase and amplitude modulation for a pressure level of $A_0 = 400$ kPa after optimization of f_1 , f_2 and α .

PROOFREADING

Appendix D

Optimal Command of Encoded Excitation for cMUTs

THIS appendix presents the results of the optimal command of the encoded excitations for the cMUTs presented in section 5.3 (p. 121).

D.1 Optimal Command for Second Harmonic Imaging

The command that we propose consists in using the half resonance frequency, as shown in the Fig. 5.4. Optimal command is sought by a target signal with this new frequency.

Fig. D.1 represents the optimal command at the half resonance frequency in the same form as before.

The target signal is correctly reached with a mean square error MSE of -21 dB. Spectrally the second harmonic is reduced by 20 dB. It is important to note that our method reduces the second harmonic, but also the third harmonic; what existing methods can not do.

We also present an optimization where the cMUT output do not follows the target signal visibly. In this case, the amplitude of the target signal was $\pm 17,5\%$. The mean square error MSE still reaches -17 dB. In contrast with the case of the forced regime, the cMUT output is not cut the top off, but the membrane can not oscillate as slowly as the target signal. Spectrally, the second harmonic is still reduced by 10 dB, but with an increase of the third harmonic.

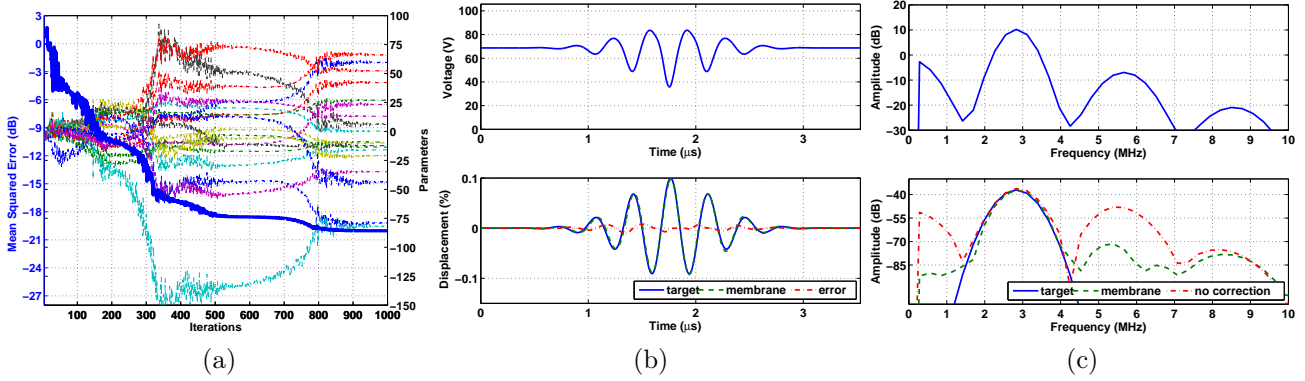


Figure D.1 – Simulation of the iterative optimization of the cMUT output when the target signal to be reached is a sine wave signal of a frequency $f_{res}/2$ and amplitude representing a membrane displacement u_{mb} of $\pm 10\%$ of the size of the cavity. (a) Mean quadratic error between the target signal MSE and the membrane displacement u_{mb} during the iterations k with the input parameters of the system. (b) cMUT command at the top. Normalized cMUT output in relation to the cavity size, target signal and error at the bottom. (c) Spectrum of the cMUT command at the top. Spectrum of target signal and cMUT output before and after optimization at the bottom.

D.2 Optimal Command for Pulse Inversion Imaging

As for the forced regime, we optimize with an target where the phase is opposite in comparison with this one presented in Fig. D.3. The optimal command correctly reaches again the target signal.

D.3 Optimal Command for Chirp Reversal Imaging

In the context of imaging by chirp reversal, we also tested the case where the frequency modulated signal (20 GHz/s) is centered at the half resonant frequency.

Figs. D.4 and D.5 represent optimizations with targets where the modulation slopes are inverted.

Targets are correctly reached. We can notice that the error is slightly more important for the lower frequencies due to transient phenomena between the forced regime and the resonant regime.

D.3. OPTIMAL COMMAND FOR CHIRP REVERSAL IMAGING

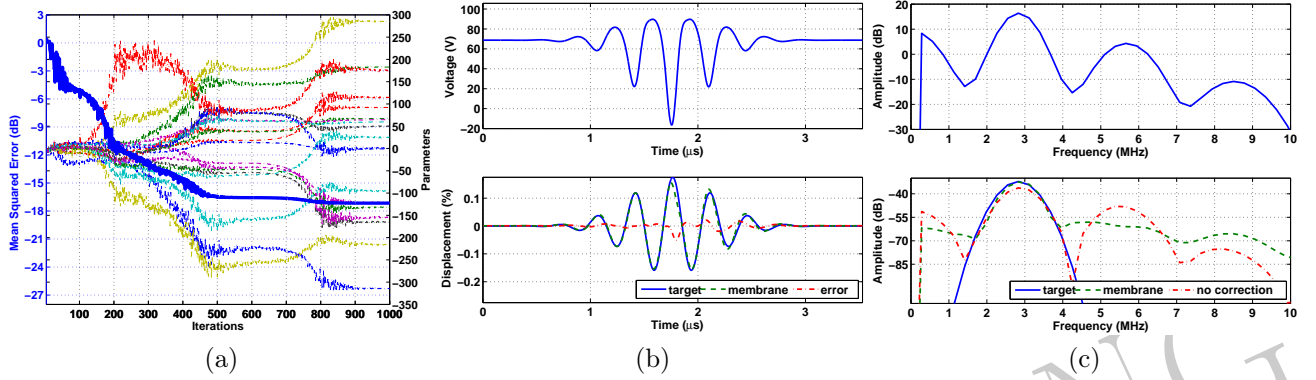


Figure D.2 – Simulation of the iterative optimization of the cMUT output when the target signal to be reached is a sine wave signal of a frequency $f_{res}/2$ and amplitude representing a membrane displacement u_{mb} of $\pm 17.5\%$ of the size of the cavity. (a) Mean quadratic error between the target signal MSE and the membrane displacement u_{mb} during the iterations k with the input parameters of the system. (b) cMUT command at the top. Normalized cMUT output in relation to the cavity size, target signal and error at the bottom. (c) Spectrum of the cMUT command at the top. Spectrum of target signal and cMUT output before and after optimization at the bottom.

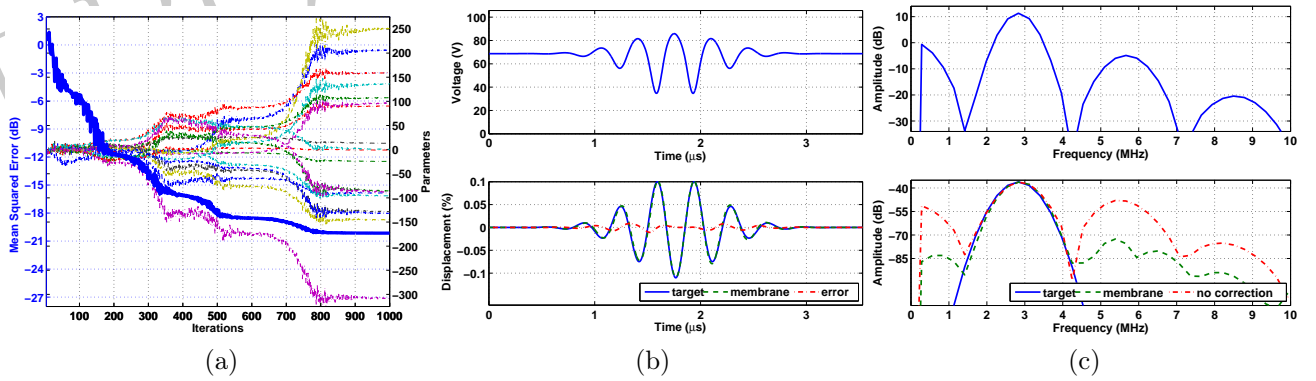


Figure D.3 – Simulation of the iterative optimization of the cMUT output when the target signal to be reached is a sine wave signal of a frequency $f_{res}/2$, in opposite phase to the target signal presented in Fig. D.1b, and amplitude representing a membrane displacement u_{mb} of $\pm 10\%$ of the size of the cavity. (a) Mean quadratic error between the target signal MSE and the membrane displacement u_{mb} during the iterations k with the input parameters of the system. (b) cMUT command at the top. Normalized cMUT output in relation to the cavity size, target signal and error at the bottom. (c) Spectrum of the cMUT command at the top. Spectrum of target signal and cMUT output before and after optimization at the bottom.

APPENDIX D. OPTIMAL COMMAND OF ENCODED EXCITATION FOR CMUTS

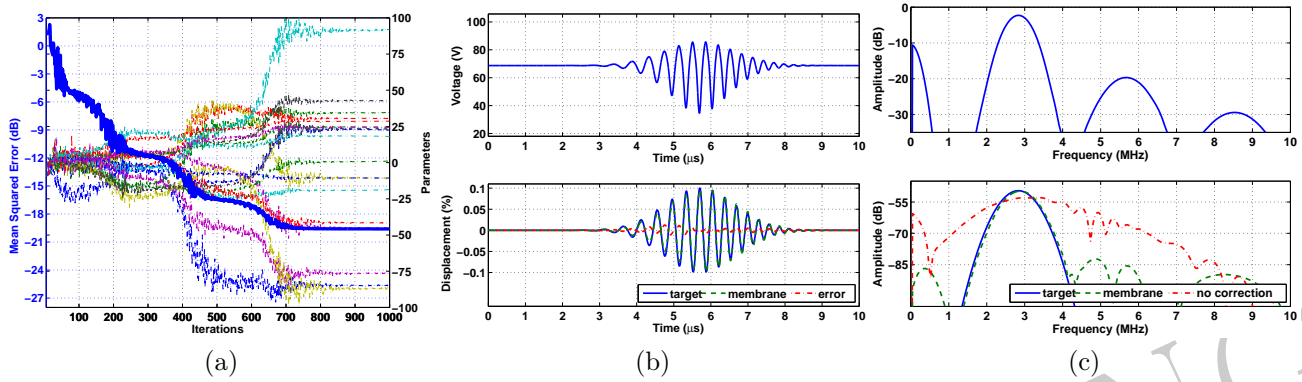


Figure D.4 – Simulation of the iterative optimization of the cMUT output when the target signal to be reached is a sinusoidal frequency-modulated signal where $f_0 = f_{res}/2$ and $\beta_1 = 20$ GHz/s, and amplitude representing a membrane displacement u_{mb} of $\pm 10\%$ of the size of the cavity. (a) Mean quadratic error between the target signal MSE and the membrane displacement u_{mb} during the iterations k with the input parameters of the system. (b) cMUT command at the top. Normalized cMUT output in relation to the cavity size, target signal and error at the bottom. (c) Spectrum of the cMUT command at the top. Spectrum of target signal and cMUT output before and after optimization at the bottom.

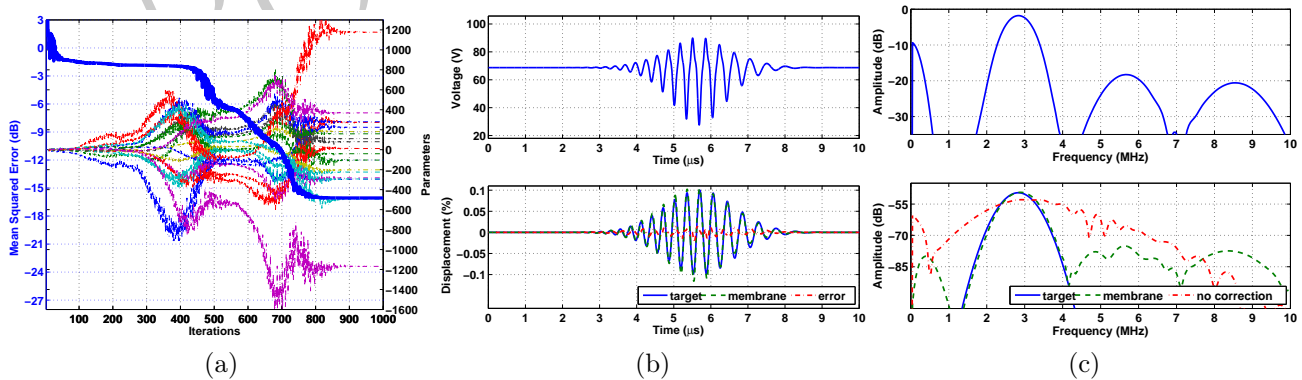


Figure D.5 – Simulation of the iterative optimization of the cMUT output when the target signal to be reached is a sinusoidal frequency-modulated signal where $f_0 = f_{res}/2$ and $\beta_1 = -20$ GHz/s, and amplitude representing a membrane displacement u_{mb} of $\pm 10\%$ of the size of the cavity. (a) Mean quadratic error between the target signal MSE and the membrane displacement u_{mb} during the iterations k with the input parameters of the system. (b) cMUT command at the top. Normalized cMUT output in relation to the cavity size, target signal and error at the bottom. (c) Spectrum of the cMUT command at the top. Spectrum of target signal and cMUT output before and after optimization at the bottom.

Appendix E

List of publications

Peer-Reviewed Articles

Articles published

Ménigot, S., Girault, J.-M. et Voicu, I. (2012). Optimisation des paramètres fréquentiels du signal d'émission appliquée à l'imagerie de contraste ultrasonore du second harmonique. *IRBM*, 33:211–216.

Girault, J.-M., **Ménigot, S.** et Voicu, I. (2012). Détection automatique de micro-emboles cérébraux grâce à un nouveau détecteur de variance conditionnelle. *IRBM*, 33:217–222.

Voicu, I., Girault, J.-M. et **Ménigot, S.** (2012). Estimation du rythme cardiaque fœtal par l'estimateur YIN. *IRBM*, *sous presse*.

Girault, J.-M., Kouamé, D., **Ménigot, S.** et Souchon, G. and Tranquart, F. (2011). Analysis of Index Modulation in Microembolic Doppler Signals Part I: Radiation Force as a New Hypothesis–Simulations. *Ultrasound in medicine & biology*, 37(1):87–101.

Girault, J.-M., Kouamé, D., **Ménigot, S.**, Guidi, F., Souchon, G. et Remenieras, J. P. (2011). Analysis of Index Modulation of Doppler

Microembolic Signals PartII: In Vitro Discrimination. *Ultrasound in Medicine & Biology*, 37(1):102–111.

Articles in Review (during the thesis defence)

Ménigot, S., Girault, J.-M., Voicu, I. et Novell, A. (2012). Optimization of Contrast to Tissue Ratio by Frequency Adaptation in Pulse Inversion Imaging. *IEEE Transactions on Ultrasonics Ferroelectrics and Frequency Control*, 59(11):2431–2439.

Conferences with Act

2010

Ménigot, S., Voicu, I., Novell, A., Elkateb Hachemi Amar, M. et Girault, J.-M. (2010). Adaptive Matched Filters for Contrast Imaging. *In Proceeding IEEE Ultrasonic Symposium*, pages 1–4. San Diego, CA, USA.

Ménigot, S., Novell, A., Voicu, I. et Girault, J.-M. (2010). Optimisation de l'énergie rétrodiffusée en imagerie de contraste par la fréquence de transmission. *10ème Congrès Français d'Acoustique*. Lyon, France.

Girault, J.-M., **Ménigot, S.**, Dreibine, L. et Meziati, N. (2010). Détection US automatique de micro-embolies par des techniques de prédictions linéaires synchrones. *10ème Congrès Français d'Acoustique*. Lyon, France.

2009

Ménigot, S., Dreibine, L., Meziati, N. et Girault, J.-M. (2009). Automatic Detection of Microemboli by Means of a Synchronous Linear Prediction Technique. *In Proceeding IEEE Ultrasonic Symposium*, pages 2371–2374. Rome, Italy.

Ménigot, S., Novell, A., Bouakaz, A. et Girault, J.-M. (2009). Improvement of the Power Response in Contrast Imaging with Transmit Frequency

Optimization. *In Proceeding IEEE Ultrasonic Symposium*, pages 1–4. Rome, Italy.

Ménigot, S., Novell, A., Voicu, I., Bouakaz, A. et Girault, J.-M. (2009). Transmit Frequency Optimization for Ultrasound Contrast Agent Response. *In International Conference on Advancements of Medicine and Health Care through Technology*, volume 26, pages 181–184. Cluj-Napoca, Romania.

Ménigot, S., Novell, A., Voicu, I., Bouakaz, A. et Girault, J.-M. (2010). Adaptive Contrast Imaging: Transmit Frequency Optimization. *Physcis Procedia*, from *2009 International Congress on Ultrasonics*, volume 3, pages 667–676. Santiago, Chile.

Others communications

2011

Girault, J.-M., **Ménigot, S.**, Voicu, I., Sbeity, F. et Charara, J. (2011). A New Cerebral Micro-emboli Detector. *In International Conference on Advances in Biomedical Engineering*. Tripoli, Liban.

2010

Girault, J.-M., **Ménigot, S.** et Dreibine, L. (2010). Automatic Detection of Micro-emboli by Means of a Generalized Autoregressive Conditional Heteroskedasticity Model. *In 2nd Pan American/Iberian Meeting on Acoustics*. Cancún, Mexique.

Ménigot, S., Girault, J.-M., Voicu, I. et Novell, A. (2010). Optimization of the Contrast Tissue Ratio in Ultrasound Contrast Imaging by an Adaptive Transmit Frequency. *In First Mediterranean Congress on Acoustics*. Salé, Morocco.

Girault, J.-M., **Ménigot, S.**, Dreibine, L., Ouahabi, A. et Guibert, B. (2010). Automatic Detection of Micro-emboli by Means of a Garch Model. *In First Mediterranean Congress on Acoustics*. Salé, Morocco.

2009

Ménigot, S., Novell, A., Voicu, I., Bouakaz, A. et Girault, J.-M. (2009). Imagerie de contraste adaptative : optimisation de la fréquence d'émission. *Dans IMVIE 5 - Imagerie pour les Sciences du Vivant et la Médecine*. Mulhouse, France.

PROOFREADING

Index

- Adaptive, 89
- Chirp, 70, 100, 126, 160
- cMUT, 115–127, 159–160
 - Collapse, 118
 - Electrostatic force, 118
 - Membrane, 117
- Compensation, 116
- Contrast-to-Tissue Ratio, 74
- Feedback, 44, 74
- Filter
 - Autoregressive, 50
 - Compression, 70, 100
 - Nonlinear autoregressive, 66, 106, 120
- Imaging
 - Chirp inversion, 100–104
 - Chirp reversal, 71, 125–127, 160
 - Contrast, 55–56, 63–71, 73–74
 - Encoded, 64
 - Harmonic, 65, 121–124, 159
 - Chirp, 71, 101, 126
 - Nonlinear autoregressive filtering, 64–67, 78–87
 - Non-encoded, 64
 - Phase and Amplitude Modulation, 151–156
 - Phase and amplitude modulation, 69–70, 94–95
 - Pulse Inversion, 148
 - Pulse inversion, 67–69, 87–94, 125, 145–160
- Lagrange multipliers, 48
- Loop
 - Closed, 38, 44
 - Open, 38
- Marmottant model, *see* Microbubble
- Mean squared error, 67, 121
- Method
 - Adams-Bashforth, 58
 - Runge-Kutta, 62
 - Pseudo-spectral, 58
 - Runge-Kutta, 118
- Microbubble, 59, 63
 - Marmottant model, 59
 - Buckling, 60
 - Elastic state, 60
 - Rupture, 60
 - Surface tension, 61
- Microbubblee
 - Marmottant model, 62
- Modulation
 - Polynomial law, 100
- Non-optimized system, 37
- Optimal control under constraint, 48

-
- Optimization algorithm, 141–144
NELDER-MEAD, 82, 86, 110, 121, 142–
144
Gradient, 80, 82, 84, 88, 92, 141–
142, 145
- Perfectly-Matched boundary Layer, 58
- Phantom, 63
- Rayleigh-Plesset equation, 59
- Recursive least squares, 50, 120
Forgetting factor, 121
- Relative bandwidth, 76
- Resolution
Axial, 90
- Simplex downhill, *see* NELDER-MEAD in
optimization algorithm
- Simulation
cMUT, 117–118
Contrast Imaging, 57–62
- Sine waves modulated in frequency, *see*
Chirp
- SonoVue™, *see* Microbubble
- Time reversal, 44–45, 107, 108
- Topological energy, 46–48
- Truncated half-sinus wave, 75–99, 145–
148, 151–156
- Ultrasound contrast agents, *see* Microbubble
- Ultrasound imaging system, 37
- Ultrasound probe, 57, 63
- Volterra Series, 45
- Wave propagation, 58

PROOFREADING

Résumé: Les systèmes d'imagerie médicale ultrasonore ont considérablement amélioré le diagnostic clinique par une meilleure qualité des images grâce à des systèmes plus sensibles et des post-traitements. La communauté scientifique de l'imagerie ultrasonore a consenti à un très grand effort de recherche sur les post-traitements et sur le codage de l'excitation sans s'intéresser, outre mesure, aux méthodes de commande optimale. Ce travail s'est donc légitimement tourné vers les méthodes optimales basées sur l'utilisation d'une rétroaction de la sortie sur l'entrée. Pour rendre applicable ces méthodes, ce problème complexe de commande optimale a été transformé en un problème d'optimisation paramétrique sous-optimal et plus simple. Nous avons appliqué ce principe au domaine de l'imagerie ultrasonore : l'échographie, l'imagerie harmonique native et l'imagerie harmonique de contraste avec ou sans codage de la commande.

La simplicité de l'approche nous a permis, par une modification de la fonction de coût, de l'adapter à l'imagerie harmonique. Cette adaptation montre que la méthode peut être appliquée à l'imagerie ultrasonore en générale.

Aujourd'hui, les enjeux de l'imagerie ultrasonore portent non seulement sur les traitements des excitations ou des images mais aussi sur les capteurs. Ce point nous a conduit naturellement à rechercher la commande optimale des transducteurs capacitifs (cMUT) afin de les adapter à une utilisation plus large en imagerie ultrasonore codée. Nos méthodes de compensation et de codage par commande optimale procurent des résultats très prometteurs qui vont au delà de nos espérances.

Le champ d'applications de nos méthodes de codage optimal est large et nous n'en voyons pas forcément encore toutes les limites. L'atout majeur de nos approches est leur simplicité d'utilisation et d'implémentation. En effet, elles ne nécessitent pas d'informations *a priori* difficilement accessibles sur les outils utilisés ou milieux explorés. Notre système s'adapte automatiquement aux variations qui peuvent être liées au vieillissement du capteur ou à la modification du milieu exploré.

Mots clés: Boucle fermée, commande optimale, optimisation, imagerie ultrasonore, système adaptatif.

Abstract: Medical ultrasound imaging systems have greatly improved the clinical diagnosis by improving the image quality thanks to more sensitive systems and post-processings. The scientific community has made a great effort of research on post-processing and on encoding the excitation. The methods of the optimal control have been neglected. Our work has focused on the optimal methods based on the feedback from output to input. We have transformed the complex problem of optimal control into an easier suboptimal parametric problem. We apply the principle of optimal control to the ultrasound imaging, the ultrasound harmonic imaging and to the contrast harmonic imaging with or without encoding.

The simplicity of the method has allowed us to adapt it to harmonic imaging by a change in the cost function. This adaptation shows that our method can usually be applied to the ultrasound imaging.

Nowadays, the stakes of the ultrasound imaging focus not only on the excitation processings or image processings but also on the sensors. This point naturally leads us to seek the optimal control of the capacitive transducers (cMUT) in order to adapt them to the encoded ultrasound imaging. Our compensation and encoding methods by optimal control provide very promising results that go beyond our expectations.

The application scope of our methods of optimal control is large and we do not see all the limits yet. The main advantage of our approaches is the easiness of their use and of their implementation. Indeed, our approaches do not require any *a priori* knowledge on system and medium explored. Our system automatically adapts itself to the changes which may be related to sensor ageing or to the medium change.

Keywords: Adaptive system, closed-loop, optimal control, optimization, ultrasound imaging.